RESEARCH INVESTIGATIONS OF BULKHEAD CYLINDRICAL JUNCTIONS EXPOSED TO COMBINED LOAD, CRYOGENIC TEMPERATURES AND PRESSURE

PART I EXPERIMENTAL STUDIES

by

C. A. Sciammarella

Technical Report
Contract No. NAS8-5199
Prepared for
George C. Marshall Space Flight Center
NASA
Huntsville, Alabama
National Aeronautics and Space Administration
Washington 25, D. C.

Department of Engineering Science and Mechanics
Engineering and Industrial Experiment Station
University of Florida
Gainesville, Florida

November, 1965

RESEARCH INVESTIGATIONS OF BULKHEAD CYLINDRICAL JUNCTIONS EXPOSED TO COMBINED LOAD, CRYOGENIC TEMPERATURES AND PRESSURE

Part I

Experimental Studies

by

C. A. Sciammarella

Technical Report
Contract No. NAS8-5199
Prepared for
George C. Marshall Space Flight Center
NASA
Huntsville, Alabama
National Aeronautics and Space Administration
Washington 25, D.C.

Department of Engineering Science and Mechanics
Engineering and Industrial Experiment Station
University of Florida
Gainesville, Florida

November, 1965

ABSTRACT 17098

The objective of this study is the experimental analysis of one design version of an aft bulkhead-connection ("Y - ring section") of a Saturn V S-IV lox container.

Two different sections are contained in the report. The first section deals with a two-dimensional analog model built to study the bending stresses of the "Y-ring." Two experimental stress techniques were applied in this study. The "wire model" was utilized to measure displacements. Photoelasticity was used to measure bending stress concentration effects.

The second section of the report deals with the study of a 1/6 reduced scale model of the tank. Strain-gauges and displacement transformers were applied to the model to measure strains and displacements.

Results of the reduced scale model show very good agreement between the theoretically computed stresses and the stresses determined in the model.

Author

Section I

1. Introduction

The theoretical background underlying this study has been given in Part II of this report. In the analysis of the stress distribution of the aft-bulkhead-connection T-ring the so-called influence coefficient approach was used (see Section 3, Part II).

The coefficients were partially obtained from experimental data of a Moiré test performed with a two-dimensional 1:1 scale model. Although the values of the coefficients could have been obtained by a numerical approach, the experimental method was selected. This approach served a twofold purpose. Besides being used to determine the influence coefficients, the two-dimensional analog model was used also as a photoelastic model to find stress concentration factors.

In this chapter we will describe the process followed in the design and test of the 1:1 two-dimensional analog model.

2. Similitude Laws

As described in Section 3 of Part II of this report, the structure under analysis was divided into five pieces or parts, Figure 1. The Moiré model includes Pieces No. 1, No. 2, and No. 3.

To design the model the similitude of the differential equation that governs the bending of a cylindrical shell and the equation corresponding to the bending of a beam on elastic foundations was utilized [1].

The equation corresponding to the bending of a thin cylindrical shell of variable thickness in the x,w coordinate system, Figure 2, is

$$\frac{d}{dx^2}\left[D\frac{d^2w}{dx^2}\right] + \frac{Eh}{a^2}w = 0 \qquad (1)$$

where $D = \frac{Eh^3}{12(1-\nu^2)}$, E is the modulus of elasticity, ν Poisson's ratio, h the shell thickness, and a the shell radius.

We can express the shell thickness in the following manner:

$$h = h_o f(x) \qquad (2)$$

where h_o is a reference thickness and f(x) a function of x giving the dimensionless value of the thickness.

Equation (1) can be written

$$\frac{d^2}{dx^2}\left[\frac{Eh_o^3}{12(1-\nu^2)} f(x) \frac{d^2w}{dx^2}\right] + \frac{Eh_o f(x)}{a^2} w = 0 \qquad (3)$$

which can be transformed into

$$\frac{d^2}{dx^2}\left[f(x) \frac{d^2w}{dx^2}\right] + \frac{12\, f(x)(1-\nu^2)}{h_o^2 a^2} w = 0 \qquad (4)$$

The corresponding equation for a beam with variable moment of inertia and variable foundation modulus is

$$\frac{d^2}{dx^2}\left[f(x) \frac{d^2w}{dx^2}\right] + \frac{12\, k(x)}{Eb\, h_o^3} w = 0 \qquad (5)$$

where k(x) is the variable foundation modulus and b the beam width.

From Equations (4) and (5) the following similitude condition is obtained:

$$k(x) = \frac{Eb\, h_o\, f(x)\, (1-\nu^2)}{a^2} \qquad (6)$$

If we know f(x) we can compute k(x) utilizing Equation (6).

The above conditions of similitude are valid if the scale of length and the materials of the model and phototype are equal.

In the problem under consideration the equality of the length scales can be preserved without difficulty.

The effect of the change of material can easily be taken into account. Let us assume that we have two elastically supported beams, one with the same material as the prototype and the other with a different material that we call model material. The deflections of both beams are given by

$$w_p = \int \frac{M_p}{E_p I_p} x \, dx \tag{7}$$

and

$$w_m = \int \frac{M_m}{E_m I_m} x \, dx \tag{8}$$

where the subscripts p and m indicate the prototype and the model, respectively, I the moment of inertia of the beam, and M the bending moment.

From (7) and (8)

$$\frac{w_p}{w_m} = \frac{M_p E_m I_m}{M_m E_p I_p} \tag{9}$$

Now if $M_p = M_m$ and $I_m = I_p$, we obtain

$$w_p = w_m \frac{E_m}{E_p} \tag{10}$$

Using the above law the deflections measured in the model can be translated to the beam having the same material as the prototype. These deflections will also be the deflections in the shell.

3. Model Design

To provide an elastic foundation for the two-dimensional model, cantilever beams of yellow brass wire were used. Figure 3 shows the system used to simulate the elastic foundation. The wires were spaced 1/4 inch apart. In the fixed end they were close-fitted into holes drilled in aluminum bars. To provide a free end condition at the point of connection with the beam, steel rings with a longitudinal slot were cemented to the side of the model, Figure 4.

Figure 5 shows a general sketch of the Y-ring with an indication of the regions into which the elastic foundation was divided. Three different regions were considered according to the changes of thickness. Regions 1 and 2 have constant thickness, therefore the cantilever beams used to simulate the elastic foundation have constant length. Since in Region 2 the thickness is variable, the length of the beams was adjusted to this change. Figure 6 shows the elastic foundation with the corresponding three regions.

To define the end conditions of the model, the following considerations were applied.

The length of Piece No. 1, corresponding to the cylinder wall of constant thickness, was computed so that the edge perturbations originating at its end would not influence the Y-ring.

At the other end, the skirt was connected to a corrugated inter-tank by means of clamps bolted to both the skirt and to the corrugated inter-tank. The clamps were replaced by an equivalent beam with a variable moment of inertia corresponding to the change of moment of inertia of the clamp. The bolted union between the skirt and the clamp was simulated by two connecting screws, Figure 7.

Since the moment of inertia of the transversal section of the inter-tank is several times larger than the moment of inertia of the skirt, it was assumed that the connection between the clamp and the inter-tank corresponds to a fixed end. Figure 8 shows a top view of the model.

4. Tests Performed in the Model

In Part II of this report it is shown (page 14 and following) that the actual tank has been substituted by a shell configuration consisting of two principal systems, each of which is additionally subdivided into several shell components of classical shape.

From the analytical point of view, there is no need to introduce two principal systems, since the whole computation could have been handled in one single system. However, preference was given to a representation of the tank by two principal systems, since System I could be treated twice, analytically and experimentally. As we can see from Figure 9, since System I consists of circular cylindrical shells only, it was thus possible to study experimentally a two-dimensional model of System II. Consequently, comparison between the analytical and the experimental approaches could be made. The comparison is very important since the mathematical model used for the theoretical computation is somewhat simplified, whereas the shape of the two-dimensional model does not take into consideration the effects that the fillet radius of the different transitions present in the model. The fillets produce secondary effects which are not taken into consideration by the common shell theory. However, these effects are accounted for by the two-dimensional analog model.

As shown in Figure 9, System I is composed of the following elements:

Piece No. 1. Semi-infinite circular cylinder with constant wall thickness.

Piece No. 2. Finite circular cylinder with variable wall thickness (part of the Y-ring).

Piece No. 3. Finite circular cylinder with constant wall thickness with connecting clamp (skirt).

Four different tests were performed. The model was sectioned according to the scheme shown in Figure 9. Displacements and rotations of the ends of the component pieces were determined.

The model was tested as a whole to determine the rotation and the displacements of section M,M, Figure 9.

5. System of Load Application

One of the problems that the test on plastic model presents is the creep phenomena of the material. Due to creep of the material the effective modulus of elasticity changes with the time, and, therefore, if a constant external load is applied, deformations keep on increasing with the time. This makes it very difficult to interpret deflection measurements.

Through the use of the so-called technique of the spring-balance this difficulty can be overcome.

In this technique displacements are imposed on the model through a loading element made out of the same material as the model. The spring-balance may be designed with an arbitrary shape. In the present case spring-balances with the shape of circular rings were utilized. One of such balances is shown in Figure 10. It consists of a plexiglass ring, two aluminum pieces with a gap. One end of the balance is applied to the point of loading by pieces of a steel ball. The other end is connected to a block screwed on the same table

that supports the model. At the block end an Allen-type screw provides the means for applying a displacement. The theory of the spring-balance can be explained as follows.

Let us assume in Figure 11 that we apply to the system model spring-balance a displacement Δ. (In this case the model is shown to be a cantilever beam, but the derivation is general.)

We can write

$$\Delta = \Delta_s + \Delta_m \tag{11}$$

where Δ_s is the displacement of the balance and Δ_m is the displacement of the model.

The values of Δ_s and Δ_m can be expressed by the following equations, assuming that the material is linearly viscoelastic

$$\Delta_m = K_m \frac{P_{(t)}}{E_{(t)}} \tag{12}$$

and

$$\Delta_s = K_s \frac{P_{(t)}}{E_{(t)}} \tag{13}$$

where K_m and K_s are constants of proportionality that depend on the geometries of the spring-balance and the model, $P_{(t)}$ and $E_{(t)}$ are the load and the modulus of elasticity, both functions of the time.

Replacing in (11), we obtain

$$\Delta = \frac{K_m P_{(t)} + K_s P_{(t)}}{E_{(t)}} \tag{14}$$

From Equation (14)

$$\frac{P_{(t)}}{E_{(t)}} = \frac{\Delta}{K_s + K_m} \tag{15}$$

This means that the relationship between the load and the modulus of elasticity is constant and independent of the time.

In order to compute the constant K_s corresponding to the balance, the spring-balance is applied to a cantilever beam and loaded with a dead weight, Figure 12.

The deflection of the beam is given by

$$\delta = \frac{1}{3} \frac{P\ell^3}{EI} \tag{16}$$

where δ is the deflection of the cantilever beam, P the load, ℓ the beam span, E the elasticity modulus, and I the moment of inertia of the beam section.

From Equation (13)

$$E_{(t)} = \frac{K_s}{\Delta_s} P_{(t)} \tag{17}$$

Replacing in (16)

$$K_s = \frac{1}{3} \frac{\ell^3 \Delta_s}{\delta I} \tag{18}$$

Equation (18) gives the value of K_s.

In our measurements we need to know the effective values of the applied loads. The procedure for obtaining the load is the following. From (12) and (13)

$$\frac{\Delta_m}{\Delta_s} = \frac{K_m}{K_s} \therefore K_m = \frac{\Delta_m}{\Delta_s} K_s \tag{19}$$

From Equation (15) the ratio $P_{(t)}/E_{(t)}$ is constant, consequently, if we give to E the value corresponding to a reference time t_o,

$$P_{(t_o)} = \frac{E_{(t_o)} \Delta}{K_s + K_m} \tag{20}$$

The modulus for the reference time t_o is determined by measuring the Δ_s corresponding to a given P.

A pair of spring-balances was utilized to apply a given moment by means of the device shown in Figure 13.

To calibrate the balances, the beam deflections were measured by means of a dial indicator with the smallest division equal to 5×10^{-4} inches. The deformations of the spring-balance were measured with a filar microscope with 5×10^{-4} inch sensitivity. Calibration constants were computed as an average of ten readings. Four balances were calibrated with two of them making pairs of approximately the same constants. The approximate relation between the load capacity of the pairs is one to ten.

6. Testing Procedure. Check on the Constants of the Elastic Foundation. Experimental Results

The procedure applied to measure the required values from the model consisted of the following steps.

An initial load was applied by means of the spring-balance. A filar microscope was used to find the displacement corresponding to the balance. Fringe position was determined by means of a ruler divided into 1/100 of an inch. Figure 14 illustrates the procedure used to measure fringe position. A final load was applied, and the deflections of the beam were determined as a difference between the initial and final patterns. For each pattern, loads in opposite directions were applied. With this technique, nonlinear effects, coming from the change of the geometrical shape of the model with the load, were eliminated. Obtained values were consistent and showed a good reproductivity.

Figure 15 shows one of the Moiré patterns.

To show the feasibility of the two-dimensional analog model and to check the constants providing the similitude between the model and prototype, Piece No. 1 was used. In the model sectioned in parts, Piece No. 1 is a finite beam or elastic foundation whose solution is known theoretically. In Figure 16 the theoretical and experimental results are plotted together showing good agreement.

Once it was established that the behavior of the model was satisfactory, measurements leading to the determination of the constants corresponding to System No. 1 were carried out. Concentrated forces and couples were applied to the ends of Pieces No. 2 and No. 3, Figure 9.

Results are plotted in Figures 17 to 22.

By twice differentiating the displacement curves, the moment distribution corresponding to the unit load and couples was obtained. In Figures 23 to 28 the corresponding results are plotted. In order to verify the results obtained from the model, Piece No. 2 was analyzed as a cylindrical shell with linearly varying thickness. (See A2, Part II, of this report.) In Figures 23 to 26 the corresponding results are plotted together with the experimental values.

If we call w_1, Q_1, w_2, Q_2, the displacements and the rotations of the sections to the left and to the right, respectively, due to the four forces Q_1, M_1, Q_2, M_2, we can write the following relationship between the eight quantities:

$$\begin{aligned} w_1 &= \beta_{11} Q_1 + \beta_{12} M_1 + \beta_{13} Q_2 + \beta_{14} M_2 \\ Q_1 &= \beta_{21} Q_1 + \beta_{22} M_1 + \beta_{23} Q_2 + \beta_{24} M_2 \\ w_2 &= \beta_{31} Q_1 + \beta_{32} M_1 + \beta_{33} Q_2 \quad \beta_{34} M_2 \\ Q_2 &+ \beta_{41} Q_1 + \beta_{42} M_1 + \beta_{43} Q_2 \quad \beta_{44} M_2 \end{aligned} \tag{21}$$

The experimental values of the influence matrix are given by:

$$\Omega^* = \begin{bmatrix} 0.711/-3 & 0.777/-4 & 0.303/-3 & -0.600/-4 \\ 0.777/-4 & 0.132/-4 & 0.450/-4 & -0.567/-5 \\ -0.303/-3 & -0.450/-4 & -0.567/-3 & 0.501/-4 \\ 0.600/-4 & 0.567/-5 & 0.501/-4 & -0.732/-5 \end{bmatrix}$$

The corresponding theoretical values are:

$$\Omega = \begin{bmatrix} 0.85068/-3 & 0.78294/-4 & 0.31251/-3 & -0.62193/-4 \\ 0.78237/-4 & 0.13194/-4 & 0.43515/-4 & -0.56916/-5 \\ -0.31218/-3 & -0.43539/-4 & -0.49161/-3 & 0.48756/-4 \\ 0.62166/-4 & 0.56964/-5 & 0.48759/-4 & -0.73017/-5 \end{bmatrix}$$

Although the actual experimental coefficients of the symmetrical components of the matrix differed slightly from each other, the theoretical equality was applied by taking averages.

Agreement between the experimental values and the theoretical values is good and indicates that as far as the deformations are concerned, Piece No. 2 can be considered as a linearly variable thickness cylinder.

The influence coefficients, due to edge unit shear force Θ, and the unit moment M, corresponding to Piece No. 3, were experimentally obtained.

$$W^{\phi} = 0.384 \times 10^{-3}$$

$$\theta^{M} = 0.408 \times 10^{-3}$$

and

$$W^{M} = \theta^{Q} = 0.870 \times 10^{-4}$$

The last relationship is a consequence of the Betti's work theorem. Although the actual experimental values of W^{M} and θ^{Q} differed slightly from each other,

the theoretical equality was applied. To this end the experimental values $W^M = 0.855 \times 10^{-3}$ and $\theta^Q = 0.885 \times 10^{-4}$ were averaged.

To check the values corresponding to System I as a whole, a load normal to the axes of the beam was applied. The measured values were

$$W'_A = -0.113 \times 10^{-3}$$

$$\theta'_A = 0.0504 \times 10^{-4}$$

and computed values were

$$W'_A = -0.115 \times 10^{-3}$$

$$\theta'_A = 0.04948 \times 10^{-4}$$

7. Stress Concentration Factors

In the preceding sections we have analyzed the results of the determination of displacements and moment distributions from a two-dimensional analog model, applying the Moiré fringes technique.

A model with the same geometry as the one used for the Moiré determination was used as a photoelastic model for the determination of stress concentration factors at the points of transition of the Y-ring.

In the point of transition of section of different thickness, at the discontinuities introduced by shape changes, the basic assumption of the shell theory breaks down. This phenomenon is similar to the one observed in beam theory. In the regions of transition or in the proximity of concentrated load and on a length of the order of the section depth, the stress distribution departs from the one assumed in the Bernouilli-Euler theory. Photoelasticity has been used to study the stress distribution in beam discontinuities.

In our problem we can take advantage of the similitude of the bending equation of the cylinder and a beam on elastic foundation.

According to this similitude, bending stresses should be the same in both cases. The difference in the stress distribution will be that, while in the cylinder the elastic foundation is provided by hoop-rings where spring force is transmitted by shear, in the beam the spring force is applied at the outer edge. These stresses are zero at the free edges, and therefore the stresses will be the same in the cylinder and in the shell.

Although it is interesting to know the stress distribution in detail, from the practical point of view it is only necessary to know the maximum stresses and their location. The concept of stress concentration factors can be used advantageously in our problem. We can compare the experimentally determined stresses at a given location with the stresses computed according to the ordinary theory of bending, and we can determine the stress concentration factor.

In order to study the stress distribution in the joint of the knuckle, skirt and cylinder, a photoelastic model was constructed. The photoelastic model was built with the same shape as the plexiglass model used to measure the displacements. The only change was that the model material, Homalite CR 39, was employed with an elasticity modulus of 20.5×10^5 psi. Fringe constant for the material measured in bending $79 \frac{\text{lb}}{\text{in. order}}$.

Since the elasticity modulus of the homalite is nearly one-half the modulus of plexiglass, to maintain similitude it would have been necessary to build a new elastic foundation device with smaller constant of proportionality. In the case that the same device is used, this means that in the corresponding bending differential equation

$$\frac{d^4w}{dx^4} + 4\beta_o^4 w = 0 \qquad (22)$$

the constant β_o is changed. This change corresponds to a change in the geometrical dimensions of the prototype. Inasmuch as we are interested in a local effect, the stress concentration factor, rather than the stress distribution itself, it is not very likely that this effect is influenced by the value of β_o to a very large extent.

In order to investigate the maximum stress point in the groove between the knuckle and the skirt, several types of loadings were applied.

To explain the meaning of the process followed in the determination, let us first consider Figure 29. In this figure the bending diagram corresponding to the ordinary theory of bending and the bending diagram at the section corresponding to the maximum stress at the point have been plotted. The lineal stress distribution is replaced by a curved plot, and the position of the neutral axis is lowered. As a result of these two facts, the stress at one edge is larger than the stress corresponding to the lineal distribution, while the stress at the other edge is smaller. The stress distribution depends on the geometry of the section and on the type of loading. We are interested in the bending effect, and we have two possibilities, bending with and without shear force.

Several photoelastic patterns have been recorded starting with pure bending and increasing the influence of the shear force. Figures 30 to 31 contain the photoelastic patterns. The following table contains the results corresponding to these patterns.

Fig. No.	M	P	σ_b	n	σ_{ph}	$\frac{P}{M}$	C
	lb.in	lb.	lb.sq.in.		lb.sq.in.		
2	29.70	0	1260	4.5	1420	0	1.13
3	44	9.9	2360	8.6	2720	0.225	1.15
4	33.3	12.5	1800	6.5	2060	0.379	1.145
5	22	13.4	1190	4.55	1420	0.61	1.19

Depth of the section where the maximum stress takes place d = 0.665 in.

M Applied moment

P Applied force

σ_b Stress computed according bending theory

n Maximum fringe order

σ_{ph} Stress computed from photoelastic pattern

C Stress concentration factor

The location of the point of maximum stress is always the same, near the point of tangency between the circular groove and the outer face of the knuckle, Figure 34

The results show an increase of the stress concentration factor with the shear force.

Since the stresses in the region where the maximum stress concentration factor is observed are low, the effect of the stress concentration is not significant.

Section II

1. Introduction

The combined experimental and theoretical approach that is described in Parts II and III of this report required a number of simplifying assumptions introduced to make the computation feasible. The degree to which these assumptions lead to values that can be trusted, is a problem that can be settled only through an experimental determination of the stress distribution. An important question arises: Can we design a model capable of yielding the required information? Or is it necessary to perform the tests in the prototype? The problem originates in the peculiar nature of space-flight structures. Thicknesses are very small as compared with the radii involved, and consequently, a reduction in scale leads to dimensions that are difficult to handle.

2. Geometrical Similitude Laws Governing the Design of the Model

The most general similitude condition for elastic structures statically loaded requires complete geometrical similitude between the model and the prototype. The condition of strict geometrical similitude can be relaxed in many cases. One case where the strict similitude can be relaxed is the bending problem of plates. However, in the case of the theory of shells, the strict geometrical similitude cannot be relaxed, since the solution of the problem depends on the ratio of a characteristic length to the thickness. This can be shown by writing the differential equations governing the problem and putting them in dimensionless form. Let us consider Love's first approximation in the case of a general shell space.

We call ξ_1, ξ_2, and ζ a system of orthogonal coordinates in the shell space (Figure 35) and u_1, u_2, and w the corresponding displacements. The dis-

placement field consistent with the basic assumption of this theory is

$$u_1 = u_1^o + \zeta \beta_1$$
$$u_2 = u_2^o + \zeta \beta_2 \tag{23}$$
$$w = w(\xi_1, \xi_2)$$

where

$$\beta_1 = \frac{1}{\alpha_1} \frac{\partial w}{\partial \xi_1} + \frac{u_1}{R_1}$$
$$\beta_2 = -\frac{1}{\alpha_2} \frac{\partial w}{\partial \xi_2} \frac{u_2}{R_2} \tag{24}$$

where α_1, α_2 are the coefficients appearing in the expression giving the square of an arc element of the shell surface and R_1, R_2 the principal radius of curvature at the considered point.

The strain-displacement relationships are given by

$$\epsilon_{11} = \epsilon_{11}^o + \zeta \chi_1$$
$$\epsilon_{22} = \epsilon_{22}^o + \zeta \chi_2 \tag{25}$$
$$\gamma_{12} = \gamma_1^o + \gamma_2^o + \zeta (\delta_1 + \delta_2)$$

where

$$\epsilon_{11}^o = \frac{1}{\alpha_1} \left(\frac{\partial u_1}{\partial \xi_1} + \frac{u_2}{\alpha_2} \frac{\partial \alpha_1}{\partial \xi_2} \right) + \frac{w}{R_1}$$

$$\epsilon_{22}^o = \frac{1}{\alpha_2} \left(\frac{\partial u_2}{\partial \xi_1} + \frac{u_1}{\alpha_1} \frac{\partial \alpha_2}{\partial \xi_2} \right) + \frac{w}{R_2}$$

$$\gamma_1^o = \frac{1}{\alpha_1} \left(\frac{\partial u_2}{\partial \xi_1} - \frac{u_1}{\alpha_1} \frac{\partial \alpha_1}{\partial \xi_2} \right)$$

$$\gamma_2^o = \frac{1}{\alpha_2} \left(\frac{\partial u_1}{\partial \xi_2} - \frac{u_1}{\alpha_2} \frac{\partial \alpha_2}{\partial \xi_1} \right)$$

$$\chi_1 = \frac{1}{\alpha_1}\frac{\partial \beta_1}{\partial \xi_1} + \frac{\beta_2}{\alpha_2}\frac{\partial \alpha_1}{\partial \xi_2}$$

$$\chi_2 = \frac{1}{\alpha_2}\frac{\partial \beta_2}{\partial \xi_2} + \frac{\beta_1}{\alpha_1}\frac{\partial \alpha_2}{\partial \xi_1}$$

$$\delta_1 = \frac{1}{\alpha_1}\left(\frac{\partial \beta_2}{\partial \xi_1} - \frac{\beta_1}{\alpha_2}\frac{\partial \alpha_1}{\partial \xi_2}\right)$$

$$\delta_2 = \frac{1}{\alpha_2}\left(\frac{\partial \beta_1}{\partial \xi_2} - \frac{\beta_2}{\alpha_1}\frac{\partial \alpha_2}{\partial \xi_1}\right) \qquad (26)$$

According to Hooke's law,

$$\sigma_{11} = \frac{E}{1-\nu^2}(\epsilon_{11} + \nu\epsilon_{22})$$

$$\sigma_{22} = \frac{E}{1-\nu^2}(\epsilon_{22} + \nu\epsilon_{11}) \qquad (27)$$

$$\sigma_{33} = \frac{E}{2(1+\nu)}\gamma_{12}$$

The stress resultants can be obtained by integrating the above expressions across the plate thickness h, and the following results are obtained:

$$N_{11} = \frac{Eh}{1-\nu^2}(\epsilon_{11}^o + \nu\epsilon_{22}^o)$$

$$N_{22} = \frac{Eh}{1-\nu^2}(\epsilon_{22}^o + \nu\epsilon_{11}^o)$$

$$N_{12} = N_{21} = \frac{E}{2(1+\nu)}h(\gamma_1^o + \gamma_2^o)$$

$$M_{11} = D(\chi_1 + \nu\chi_2)$$

$$M_{22} = D(\chi_2 + \nu\chi_1)$$

$$M_{12} = M_{21} = \frac{Eh^3}{2(1+\nu)}\chi_{12} \qquad (28)$$

where $D = \frac{Eh^3}{12(1-\nu^2)}$ and $\chi_{12} = \delta_1 + \delta_2$.

The equilibrium equations are

$$\frac{\partial}{\partial\xi_1}(\alpha_2 N_{11}) + \frac{\partial(\alpha_1 N_{21})}{\partial\xi_2} + N_{12}\frac{\partial\alpha_1}{\partial\xi_2} - N_{22}\frac{\partial\alpha_2}{\partial\xi_1} + \alpha_1\alpha_2 X = 0$$

$$\frac{\partial}{\partial\xi_1}(\alpha_2 N_{12}) + \frac{\partial}{\partial\xi_2}(\alpha_1 N_{22}) + N_{21}\frac{\partial\alpha_2}{\partial\xi_1} - N_{11}\frac{\partial\alpha_1}{\partial\xi_2} + \alpha_2\alpha_1 Y = 0$$

$$\frac{\partial}{\partial\xi_1}(\alpha_2\gamma_1) + \frac{\partial}{\partial\xi_2}(\alpha_1\gamma_2) - \alpha_1\alpha_2\left(\frac{N_1}{R_1} + \frac{N_2}{R_2}\right) + \alpha_1\alpha_2 Z = 0$$

$$\frac{\partial}{\partial\xi_1}(\alpha_2 M_{11}) + \frac{\partial}{\partial\xi_2}(\alpha_1 M_{21}) + M_{12}\frac{\partial\alpha_1}{\partial\xi_2} - M_{22}\frac{\partial\alpha_2}{\partial\xi_1} - \alpha_1\alpha_2 V_1 = 0$$

$$\frac{\partial}{\partial\xi_1}(\alpha_2 M_{12}) + \frac{\partial}{\partial\xi_2}(\alpha_1 M_{22}) + M_{21}\frac{\partial\alpha_2}{\partial\xi_1} - M_{11}\frac{\partial\alpha_1}{\partial\xi_2} - \alpha_1\alpha_2 V_2 = 0 \qquad (29)$$

where X, Y, Z are the loads applied in the direction of the coordinate axis and

$$\gamma_1 = \int_{-h/2}^{h/2} \tau_1 \zeta \, d\zeta$$

$$\gamma_2 = \int_{-h/2}^{h/2} \tau_2 \zeta \, d\zeta \qquad (30)$$

Replacing the stress resultant in the equilibrium equations, we obtain

$$\frac{\partial}{\partial\xi_1}\left[\alpha_2 \frac{Eh}{1-\nu^2}(\epsilon_{11}^o + \nu\epsilon_{22}^o)\right] + \frac{\partial}{\partial\xi_2}\left[\alpha_1 \frac{Eh}{2(1+\nu)}(\gamma_1^o+\gamma_2^o)\right] + \frac{Eh}{2(1+\nu)}(\gamma_1^o+\gamma_2^o)\frac{\partial\alpha_1}{\partial\xi_2}$$

$$- \frac{Eh}{1-\nu^2}\frac{\partial\alpha_2}{\partial\xi_1} + \alpha_1\alpha_2 X = 0$$

$$\frac{\partial}{\partial\xi_1}\left[\alpha_2 \frac{Eh}{2(1+\nu)}(\gamma_1^o+\gamma_2^o)\right] + \frac{\partial}{\partial\xi_2}\left[\alpha_1 \frac{Eh}{1-\nu^2}(\epsilon_{22}^o + \nu\epsilon_{11}^o)\right] + \frac{Eh}{2(1+\nu)}(\gamma_1^o+\gamma_2^o)$$

$$- \frac{Eh}{1-\nu^2}(\epsilon_{11}^o + \nu\epsilon_{22}^o)\frac{\partial\alpha_1}{\partial\xi_2} + \alpha_1\alpha_2 Y = 0$$

$$\frac{\partial}{\partial \xi_1}(\alpha_2 v_1) + \frac{\partial}{\partial \xi_2}(\alpha_1 \alpha_2) - \alpha_1 \alpha_2 \left[\frac{Eh}{1-\nu^2}\left(\frac{\epsilon_{11}^o + \nu \epsilon_{22}^o}{R_1} + \frac{\epsilon_{22}^o + \nu \epsilon_{11}^o}{R_2}\right)\right] + \alpha_1 \alpha_2 Z = 0$$

$$\frac{\partial}{\partial \xi_1}[\alpha_2 D(\chi_1 + \nu \chi_2)] + \frac{\partial}{\partial \xi_2}\left(\alpha \frac{Eh^3}{2(1+\nu)} \chi_{12}\right) + \frac{Eh^3}{2(1+\nu)} \chi_{12} \frac{\partial \alpha_1}{\partial \xi_2}$$

$$- D(\chi_2 + \nu \chi_1) \frac{\partial \alpha_2}{\partial \xi_1} - \alpha_1 \alpha_2 V_1 = 0$$

$$\frac{\partial}{\partial \xi_1} \alpha_2 \frac{Eh^3}{2(1+\nu)} \chi_{12} + \frac{\partial}{\partial \xi_2}[\alpha_1 D(\chi_2 + \nu \chi_1)] + \frac{Eh^3}{2(1+\nu)} \chi_{12} \frac{\partial \alpha_2}{\partial \xi_1}$$

$$- D(\chi_1 + \nu \chi_2) \frac{\partial \alpha_1}{\partial \xi_1} - \alpha_1 \alpha_2 \gamma_2 = 0 \qquad (31)$$

For the above system of equations, we have the following boundary conditions:

1) Either we have N_{nn} specified or U_n specified

2) Either we have N_{ns} specified or U_s specified

3) Either we have $V_n = Q_n \pm \frac{\partial M_{ns}}{\partial \xi_s}$ specified or w specified

4) Either we have M_{nn} specified or $\frac{\partial w}{\partial \xi_n}$ specified

where n and s refer to the normal and the tangential directions, respectively.

The boundary conditions are of simple form and may be left out of special consideration in the analysis of similitude conditions. We can write the equilibrium equations in dimensionless form

$$\frac{\partial}{\partial \xi_1^*}\left[\frac{\alpha_2}{1-\nu^2}(\epsilon_{11}^o + \nu \epsilon_{22}^o)\right] + \frac{\partial}{\partial \xi_2^*}\left[\frac{\alpha_1}{2(1+\nu)}(\gamma_1^o + \gamma_2^o)\right] + \frac{1}{2(1+\nu)}(\gamma_1^o + \gamma_2^o) \frac{\partial \alpha_1}{\partial \xi_2^*}$$

$$- \frac{1}{1-\nu^2} \frac{\partial \alpha_2}{\partial \xi_1^*} + \alpha_1 \alpha_2 \frac{XL}{Eh} = 0$$

$$\frac{\partial}{\partial \xi_1^*}\left[\frac{\alpha_2}{2(1+\nu)}\,(\gamma_1^o+\gamma_2^o)\right]+\frac{\partial}{\partial \xi_2^*}\left[\frac{\alpha_1}{1-\nu^2}\,(\epsilon_{22}^o+\epsilon_{11}^o\nu)\right]+\frac{1}{2(1+\nu)}\,(\gamma_1^o+\gamma_2^o)\,\frac{\partial \alpha_2}{\partial \xi_1^*}$$

$$-\frac{1}{1-\nu^2}\,(\epsilon_{11}^o+\nu\epsilon_{22}^o)\,\frac{\partial \alpha_1}{\partial \xi_2^*}+\alpha_1\alpha_2\,\frac{YL}{Eh}=0$$

$$\frac{\partial}{\partial \xi_1^*}\left[\alpha_2\,\frac{\gamma_1}{Eh}\right]+\frac{\partial}{\partial \xi_2^*}\left[\alpha_1\,\frac{\gamma_2}{Eh}\right]-\alpha_1\alpha_2\left[\frac{1}{1-\nu^2}\left(\frac{\epsilon_{11}^o+\nu\epsilon_{22}^o}{R_1^*}+\frac{\epsilon_{22}^o+\nu\epsilon_{11}^o}{R_2^*}\right)\right]+\alpha_1\alpha_2\,\frac{ZL}{Eh}=0$$

$$\frac{\partial}{\partial \xi_1^*}\left[\alpha_2\,\frac{1}{12(1-\nu^2)}\,(\chi_1^*+\nu\chi_2^*)\right]+\frac{\partial}{\partial \xi_2^*}\left[\alpha_1\,\frac{1}{2(1+\nu)}\,\chi_{12}^*\right]+\frac{1}{2(1+\nu)}\,\chi_{12}^*\,\frac{\partial \alpha_1}{\partial \xi_2^*}$$

$$-\frac{1}{12(1-\nu^2)}\,[\chi_2^*+\nu\chi_1^*]\,\frac{\partial \alpha_2}{\partial \xi_2^*}-\alpha_1\alpha_2\,\frac{\nu_1 L^2}{Eh^3}=0$$

$$\frac{\partial}{\partial \xi_1^*}\left[\alpha_2\,\frac{1}{2(1+\nu)}\,\chi_{12}^*\right]+\frac{\partial}{\partial \xi_2^*}\left[\frac{\alpha_1}{12(1-\nu^2)}\,(\chi_2^*+\nu\chi_1^*)\right]+\frac{1}{2(1+\nu)}\,\chi_{12}^*\,\frac{\partial \alpha_2}{\partial \xi_1^*}$$

$$-\frac{1}{12(1-\nu^2)}\,(\chi_1^*+\nu\chi_2^*)\,\frac{\partial \alpha_1}{\partial \xi_1^*}-\alpha_1\alpha_2\,\frac{V_2 L^2}{Eh^3}=0 \qquad (32)$$

where

$$\xi_1^*=\frac{\xi_1}{L}, \qquad \xi_2^*=\frac{\xi_2}{L} \qquad (33)$$

$$\chi_1^*=\chi_1 L, \qquad \chi_2^*=\chi_2 L, \qquad \chi_{12}^*=\chi_{12} L \qquad (34)$$

and L a characteristic length.

We have the following dimensionless products

$$\frac{XL}{Eh}\,,\quad \frac{YL}{Eh}\,,\quad \frac{ZL}{Eh}\,,\quad \frac{V_1 L^2}{Eh^3}\,,\quad \frac{V_2 L^2}{Eh^3}\,.$$

In order to insure similitude we must keep the numerical values of the above dimensionless products. This can only be achieved if the model is strictly similar to the prototype.

A 1/6 scale factor was selected as a compromise between a manageable model size, which could be handled without a too large and expensive setup, and a size large enough to reproduce the basic features of the prototype.

The details of the model are shown in Figures 36 to 41.

To facilitate the manufacture of the model, some changes were made, which do not have influence in the stress distribution. The longitudinal stiffeners in the cylindrical part of the model were redesigned so that the ratio of the bending rigidity to the transversal rigidity was preserved. The inter-tank was replaced by a uniform thickness cylinder of the equivalent bending rigidity. This cylinder was long enough to reproduce the effect of the inter-tank on the prototype.

Special joining clamps were designed to fulfill the role of the clamps that were used in the prototype to connect the skirt and the inter-tank.

3. Scale Factors of the Loads to Be Applied to the Model

According to the loading scheme shown in Figure 42, we have both internal and liquid pressure. According to DWG 06-A-2-503 at station 912

Acceleration Head	29.5 psi
Max Total Pressure	54.8 psi
	Δ = 25.3 psi

At station 772

Acceleration Head	37.4 psi
Max Total Pressure	62.7 psi
	Δ = 25.3 psi

We can compute the density corresponding to the liquid from the above data

$$\gamma = \frac{\Delta p}{\Delta x} = \frac{62.7 - 54.8}{140} = 0.0564 \frac{\text{lbs}}{\text{in.}^3}$$

where Δp is the difference of pressures between the two above-mentioned stations and Δx their mutual distance.

The pressure can be then expressed

$$p(x) = p_o + \nu(x - x_o) \tag{35}$$

In what follows, upper case letters refer to prototype dimensions, lower case letters to the model dimensions. Unstarred quantities refer to the prototye, starred to the model loading.

The conditions of similitude impose the relation

$$p(x) = p^*(x) \tag{36}$$

This means that

$$p_o = p^*_o \tag{37}$$

and

$$\gamma = \nu^* \tag{38}$$

Now if we consider the axial load which is uniformly distributed in the periphery of the cylinder

$$\frac{T_1^*}{T_1} = \lambda_{\underline{1}} \tag{39}$$

where $\lambda_{\underline{1}}$ is the scale of lengths.

Since we did not have at our disposal coloidal mudd to satisfy condition (38), a pressure equal to the average pressure in the stations 912 and 772 was applied. In the case of rebound this gives

$$p = 58.7 \text{ psi} \tag{40}$$

The ratio of the internal load to the axial load in the prototype is then

$$\alpha = \frac{2214}{58.7} \cong 3.8 \tag{41}$$

For the model the above ratio must be reduced by the factor λ:

$$\alpha^{*} = \frac{3.8}{1.6} \simeq 2.39$$

Since the load was applied in steps, the above ratio was kept constant to fulfill the similitude condition.

4. Preliminary Tests

The cylindrical part of the tank is not perfectly round. The presence of this out-of-roundness modifies the assumption of radial symmetry that has been utilized in the theoretical analysis. The lack of symmetry is responsible for the introduction of large bending moments, as it has been observed by Durelli, Dally and Morse [2].

The presence of the out-of-roundness was a perturbating factor in this case, since we were looking for a confirmation for the theoretical analysis Consequently, preliminary tests were conducted to find a representative section

Measurements of the variation of the diameter were taken at a 21 1/2° interval around the circumference with no load applied. The basic setup for the test is shown in Figure 43. Three vertical positions were investigated. On the basis of these data listed in Table II, two meridians were chosen in sections of the tank periphery which most nearly conformed to a circular arc over a reasonable angle and were remote from any weld seam.

The following table gives the out-of-roundness data:

TABLE

[illegible] ROUNDNESS TEST DATA

	Reading			Mean Deviation		
				I	II	III
				+0.0135	+0.0125	+0.0062
2				-0.0215	+0.0245	+0.0169
				+0.0070	-0.0215	+0.0127
				-0.0045	-0.0005	-0.0019
			2795	+0.0042	-0.0015	-0.0043
				[illegible]	-0.0105	+0.0037
				-0.0255	+0.0235	-0.0030
				-0.0340	-0.0195	+0.0049
				+0.0105	+0.0145	-0.0031
				-0.0160	-0.0195	-0.0069
				-0.0415	-0.0595	-0.0092
12				-0.0045	-0.0225	+0.0019
				-0.0215	+0.0095	-0.0132
				-0.0065	-0.0095	-0.0135
				+0.0155	-0.0015	+0.0054

Mean Reading		
		2535

All Measurements in Inches

Figure 14 shows an exaggerated view of the geometric imperfections of the tank in the vicinity of the Y-ring. The curves are incomplete due to the presence of the pressurizing valves which obstruct the measuring device.

5. Structural Testing of the Model Tank

The objectives of the test were

(a) To determine outside and inside strains in the selected sections

(b) Outside displacements using differential transformers.

(c) Outside deformations in the vicinity of welds.

(d) Observation of the behavior of the previously detected imperfections.

With the obtained information it would be possible

(a) To obtain information in the representative sections to compare with the theoretical analysis.

(b) To determine deflections and to correlate (a) and (b), to find out the possible influence of second order effects

(c) In the vicinity of weld-seams to find the influence introduced by the presence of the seam in the state of stresses.

(d) To determine the influence of out-of-roundness on maximum stresses, and to correlate the maximum deviations from the theoretical shape.

Of the above program only parts (a) and (b) were carried out. Lack of funds interrupted the tests in the two initial stages.

The following steps were followed to fulfill the above-mentioned objectives.

1. The specific points to be investigated were precisely located.
2. The type of strain gage most suitable for this test was selected.
3. Techniques for applying and protecting the strain gages were studied.
4. A method for providing internal pressure and axial load was devised.

6. Selection of the Strain Gage

Electrical strain gages were chosen for use in this stress analysis problem, since a display of the entire strain field was unnecessary, the principal stress direction was known, and a high degree of sensitivity was required.

[illegible] very advantageous. The variables [illegible] gage type for this test were the filament [illegible] grid and lead wire configurations, the [illegible] gage [illegible] selected-melt SR-4 epoxy-backed [illegible] Two base lengths were obtained since [illegible] gage in the meridional direction because of the higher stress gradient. The characteristics of the gages were:

Gage resistance	120.3 ± 0.5 ohm
Filament material	Constantan foil
Expansion coefficient	23 micro inches/inch-°F
Base length	0.125 and 0.0625 inches
Gage factor	2.11 and 2.07

Determination of Strain Gage Location

It was desired to investigate points at 1/4 inch intervals along a vertical meridian across the ring section. However, by consideration of the size of the strain gage installation, it was concluded that this was not feasible. The smallest interval between gages permitting space for application terminals was found to be 0.2 inch. As a solution, two meridian sections were studied with the strain gages applied approximately every 1/2 inch with a relative vertical displacement between the two sets of installations of about 1/4 inch, so as to give a more complete analysis of the stress distribution. Figure 4 shows the dimensions of the ring section and the spacing of the strain gages, while the following table lists the ordinate of each strain gage installation as measured from the cover plate flange.

TABLE II

MERIDIONAL COORDINATES OF THE STRAIN GAGES
AS SHOWN IN FIGURE 45

	Distance - X - inches	
No.	Section "A"	Section "B"
1	11.43	11.12
2	11.73	11.78
3	12.55	12.37
4	13.08	12.98
5	14.15	13.38
6	14.61	14.48
7	15.11	15.01
8	15.68	15.51
9	16.36	16.01
10	16.83	16.53
11	17.43	17.03
12	18.48	17.48
13	19.06	18.65
14	19.50	19.11
15	20.08	19.58
16	20.54	20.28
17	20.97	20.93
18	21.56	21.38

8. Application and Protection of the Strain Gages

By consideration of compatibility with the strain gage, stability required, temperature range, and curing procedure, Baldwin-Lima-Hamilton's EPY-150 was selected as the bonding cement. This was a room temperature curing epoxy requiring little bonding pressure and having excellent dielectric properties. It was recommended for static measurements to 150°F.

All paint and grease were removed from the surface in the vicinity of the strain gage installations. No. 180 grit emery paper was used to smooth the surface where necessary, and just prior to gage application the entire region was meticulously cleaned with acetone. A liberal amount of epoxy was spread over the points to be studied, and care was taken to avoid forming air pockets in the cement. The gages were then positioned and all excess cement was pressed out. A small teflon sheet was placed over the area and pressure was applied by taping a foam rubber pad to the setup. The cement was allowed to cure at room temperature for several hours before removal of the pressure pads.

The resistance of each strain gage was checked at this point as a possible indication of damage. Also, ground resistance was measured for each, with 50 megohms being the minimum acceptable value.

A cluster of four strain gages was needed to completely determine the state of stress at each point. The smaller gage was mounted in the meridional direction with the larger perpendicular to it, each accompanied by a temperature compensating "dummy" gage as was shown in Figure 45. The "dummy" gages were located very close to their respective "active" gages. They were sandwiched between two strips of mylar tape with a small amount of grease to insure freedom of movement.

The interior strain gage installations were completed before any attempt was made to place the gages on the outer surface. A "stud-finder" was employed to position the gages back-to-back. This device has a magnetic pointer which reacts to the presence of ferrous material. The procedure used for locating the exterior gages was as follows: A small point magnet was placed over an interior "active" strain gage. The "stud-finder" was then swept over the general

area on the outside of the tank, and the position was marked when the pointer located the magnet.

Petrosene micro-crystalline wax was used as the protective coating for the gages since they were not susceptible to mechanical damage, only to moisture. The area surrounding the gage installations was heated above 100°F by means of heat lamps to drive out any absorbed moisture and to aid in obtaining a good bond between the wax and the aluminum surface. The wax was melted and spread over the entire area so that it covered the gages and extended up the lead wires. The coating was approximately 1/8 inch thick. Protection of the exterior strain gages was effected in the same manner as those inside.

9. Measurement of Displacements

In order to determine displacements, the deflections of the tank were measured by linear variable differential transformers.

Schaevitz linear differential transformers were utilized. The approximate sensitivity of the transformers is 10^{-3} in. per mV. The excitation to the lineal transformers was provided by the Schaevitz D MP 3 3 Demodulator.

10. Method of Loading

For the purpose of producing the state of loading existing in the prototype, a loading frame was designed. In Figure 46 we can see a picture of the loading frame.

The loading frame consists of two rigid frames made out of I beams connected in the corners by four columns and reinforced with additional plates welded to the I beams.

The axial load was provided by eight hydraulic jacks, each of ten ton capacity, positioned above the tank and screwed into the test stand. They were spaced equally around the cover plate, and the line of action of the force was directed through the middle surface of the cylindrical shell. The jacks were calibrated on a screw-driven compression testing machine prior to installation and were connected in such a manner so that all transmitted the same force simultaneously

The load was distributed by means of two rows of eight inch curved I-beam segments resting on steel balls, each segment acting as a simply-supported beam. Figure 17 is a photograph showing the use of the curved beams. The force of each hydraulic jack was divided into four equal components by means of the above diversified arrangement. Consequently, 32 equal loads were applied to the periphery of the tank. This means that a uniformly distributed load was obtained in the region of interest.

Besides the axial load an internal pressure was applied. Two electrical pumps were utilized. One of the pumps was connected to the jacks through a system of valves to insure a uniform distribution of the oil pressure to the eight jacks.

The tank was filled with transformer oil as the pressurizing fluid because of its good dielectric properties. The second pump provided the required internal pressure.

The cover plate of the tank was fitted with ten 3/4 inch water tight connectors. In addition, two holes were drilled and tapped in the cover to accommodate the necessary valves for pressurization. One was provided as an air escape valve during the filling operation. The other, as a regulator, to control the pressure when tank capacity had been reached.

Figures 48, and 49 show details of the strain gage installation. Figure 50 shows the differential transformer installation.

11. Measurement and Recording Instruments

A 36-channel recording system (Figure 51) was utilized to record the strain gage readings. The system features (1) a fringe balancing unit that can be operated by a servo gun or manual control, (2) a relay unit capable of switching one bank of thirty-six input signals for another, and (3) a 24-channel recorder complete with automatic sequencer and trace identifier.

The output of the differential transformed was recorded with a Brush recorder.

12. Preliminary Test

Prior to filling the tank with the transformer oil, certain points were selected to study the effect of the oil weight on the deformation of the tank in the Y-ring region. The strain gages measuring the tank deflection at these points were connected to the bridge for initial balancing, and the oil was then pumped into the tank. When tank capacity had been reached, the strain gage outputs were recorded. However, the weight of the oil was found to produce a negligible effect on the strain gages' readings.

13. Strain Due to Loading

The group of selected strain gages was removed from the recording unit, and the first bank of twenty-four cables was connected to the bridge. Initial balancing of these gages was achieved with the transformer oil already in the tank. The internal pressure and the axial load were increased to the specified values concurrently. We recall that the two pressures have a given relationship which is established by design specifications. In all

loading processes, this ratio was kept as constant as was feasible. The strain gages were read in groups of twenty-four. For each group of twenty-four gages, readings were made at three levels of load. Maximum load applied was 30 psi internal pressure. Since the theoretical computation yielded very high stresses at certain points of the Y-ring, no attempt was made to apply the full load to avoid a possible damage to the model.

14. The Data

To obtain the true strain from the strain gage readings, it was necessary to introduce a calibration factor. The calibration constant is a function of the strain gage resistance, the gage factor, and the value of the calibrating resistor in the bridge balance unit. It was determined by finding the change in resistance in the active arm of the bridge produced by switching the calibrating resistor in parallel with the strain gage and putting this value into the equation,

$$F = \frac{\Delta R/R}{\epsilon} \tag{42}$$

which is the definition of gage factor. This gives the value of the strain which was caused by the change in resistance, ΔR, due to the calibrating resistor. Dividing this value of the strain by the number of units of deflection produced on the recorder, the calibration factor is obtained. The true strain may now be found from the strain gage readings by multiplying by this calibration constant.

The stresses were calculated by the following relations:

Meridional stress: $$\sigma_x = \frac{E}{1-\nu^2}(\epsilon_x + \nu\epsilon_\theta) \tag{43}$$

Circumferential stress: $$\sigma_\theta = \frac{E}{1-\nu^2}(\epsilon_\theta + \nu\epsilon_x) \tag{44}$$

The resultant values of the stresses corresponding to the applied loads are listed in Tables III and IV. The stresses in the elliptical head are given in Table IV. The displacements are given in Table V It can be seen from these tables that the stresses are linear functions of the applied load. The correlation between the previously derived theoretical stresses and those obtained by experiment is shown in Figure 52 for the interior points. Figure 53 contains similar curves for the exterior. Figure 54 contains the stress distribution in the elliptical head.

Figure 55 shows the plot load versus strain gage readings, for three given gages. The linearity is very good. Figure 56 shows the deflections of the Y-ring under maximum load. Figure 57 shows the deflections of the elliptical head which have been plotted.

15. Conclusions

The good correlation between the theoretical and experimental values indicates that all the assumptions made on the theoretical analysis proved to be correct within the range of precision of the experimental results. In the region of the knuckle, the experimental results show larger strains in the interior face than those obtained by computation. At the same time the stresses in the outer face are smaller. This means larger bending stresses than those obtained by the theoretical analysis. However, in the knuckle, the experimental results cannot be weighed too heavily. The reason for this is that the region is too small, and consequently, it was only possible to investigate two points on the outer and inner faces.

Another very significant point has been proved also, the possibility of an accurate analysis by means of reduced scale models. At first glance, a one-to-one relationship seems ideal, because it is possible to reproduce

TABLE III

INTERIOR STRESS DATA

	Pressure: 10 psi Axial Load: 239 $\frac{\text{pounds}}{\text{inch}}$				Pressure: 20 psi Axial Load: 478 $\frac{\text{pounds}}{\text{inch}}$				Pressure: 30 psi Axial Load: 717 $\frac{\text{pounds}}{\text{inch}}$			
X	ϵ_x	ϵ_θ	σ_x	σ_θ	ϵ_x	ϵ_θ	σ_x	σ_θ	ϵ_x	ϵ_θ	σ_x	σ_θ
11.12	-485	746	-3040	6990	-1002	1481	- 6408	13759	-1550	2275	-10100	20600
11.78	-502	689	-3425	6268	-1034	1356	- 7340	12186	-1602	2110	-11300	19000
12.37	-548	601	-4287	5090	-1121	1187	- 8912	9914	-1690	1878	-13150	16000
12.55	-554	609	-4322	5161	-1131	1191	- 9017	9926	-1725	1915	-13400	16300
12.98	-509	543	-4031	4543	-1036	1065	- 8353	8796	-1548	1695	-12100	14300
13.08	-422	427	-3425	3495	- 863	843	- 7107	6803	-1342	1352	-10900	11050
13.38	-376	368	-3099	2971	- 771	758	- 6338	6140	-1140	1174	- 9200	9700
14.15	- 58	200	23.3	2132	- 121	420	- 431	4474	- 201	618	- 187	6500
14.51	55	312	1736	3844	102	618	3355	7561	154	960	5115	11700
15.01	38	328	1584	3961	74	671	2423	7992	101.2	970	4560	11650
15.51	299	184	4124	3192	588	351	8073	6175	765	510	10700	8630
16.01	198	78	2586	1607	389	141	5021	3029	545	208	7070	4320
16.36	149	51	1910	1118	245	97	3204	2004	400	129	5100	2900
16.53	167	15.2	2004	760	324	39.1	3868	1584	420	51.6	5070	2075
17.03	122	-21.4	4823	1188	827	-52.3	9448	2283	1217	- 71	13950	3450
17.48	-214	- 68	- 489	- 862	-50.1	- 141	- 1072	- 1817	- 101	- 183	- 1820	- 2480
18.48	663	- 753	5091	-6454	1289	-1521	9704	-13316	1900	-2240	14300	-19500
18.65	712	- 726	5755	-5965	1392	-1475	10974	-12290	2060	-2220	16250	-18700
19.58	740	- 651	6349	-4998	1489	-1321	12733	-10135	2125	-1917	18100	-14900
20.28	671	- 613	5674	-4800	1357	-1240	11475	- 9704	1998	-1811	16950	-15300
21.38	658	- 501	5918	-3530	1330	-1023	11917	- 7258	2032	-1450	18600	- 9800

TABLE IV

EXTERIOR STRESS DATA

	Pressure: 10 psi Axial Load: 239 $\frac{\text{pounds}}{\text{inch}}$				Pressure: 20 psi Axial Load: 478 $\frac{\text{pounds}}{\text{inch}}$				Pressure: 30 psi Axial Load: 717 $\frac{\text{pounds}}{\text{inch}}$			
X	ϵ_x	ϵ_θ	σ_x	σ_θ	ϵ_x	ϵ_θ	σ_x	σ_θ	ϵ_x	ϵ_θ	σ_x	σ_θ
11.12	-248	671	- 548	6943	- 475	1310	- 955	13607	- 703	1966	- 1316	20445
11.78	-207	593	- 315	6186	- 386	1157	- 454	12128	- 562	1726	- 524	18116
12.37	-139	528	230	5662	- 258	1046	652	11289	- 399	1548	745	16636
12.55	-175	462	- 361	4776	- 327	900	- 664	9343	- 491	1349	- 1002	13863
12.98	-171	381	- 655	3833	- 318	743	- 1106	7538	- 455	1138	- 1340	11650
13.38	-243	375	-1503	3518	- 67	752	- 2807	7130	- 673	1099	- 3996	10450
14.15	-279	282	-2260	2307	- 588	556	- 4927	4427	- 799	799	- 6512	6512
14.48	-219	257	-1654	2225	- 148	481	- 3542	4043	- 638	728	- 4893	6244
14.61	-275	251	-2330	1957	- 581	492	- 5044	3705	- 873	708	- 7701	5196
15.01	-289	184	-2726	1130	- 602	347	- 5801	1934	- 865	495	- 8341	2737
15.51	-382	155	-3903	466	- 775	296	- 7992	734	-1199	470	-12326	1282
16.01	-237	27	-2668	- 513	- 496	60	- 5499	- 1037	- 762	93	- 8551	- 1572
16.53	-128	- 57	-1689	-1105	- 248	- 115	- 3297	- 2202	- 348	- 181	- 4683	- 3320
16.83	-185	-121	-2575	-2062	- 355	- 246	- 4998	- 4112	- 521	- 402	- 7479	- 6501
17.48	291	-127	2947	- 466	607	- 263	6454	- 943	961	- 425	9704	- 1712
18.48	481	-421	4136	-3227	1032	- 883	8936	- 6675	1527	-1363	13024	-10543
18.65	427	-301	3926	-2015	891	- 713	7910	- 5196	1295	-1048	11417	- 7689
19.11	641	-587	5359	-4602	1313	-1207	11079	- 9495	2006	-1837	16950	-15553
19.58	681	-572	5930	-4287	1392	-1196	12046	- 9063	2130	-1778	18605	-13269
20.28	678	-510	6116	-3577	1341	-1147	11615	- 8679	2057	-1610	18337	-11551
20.54	704	-548	6291	-3926	1415	-1190	12326	- 8912	2190	-1730	19467	-12500
21.56	752	-482	7072	-2982	1483	-1042	13631	- 6955	2287	-1467	21517	- 9099

TABLE V

ELLIPTICAL HEAD STRESS DATA

Interior

	Pressure: 10 psi Axial Load: 239 pounds/inch				Pressure: 20 psi Axial Load: 478 pounds/inch				Pressure: 30 psi Axial Load: 717 pounds/inch			
X												
27.8	711	-130	7829	907	1441	-263	15867	1969	2037	-366	22449	2854
33.9	639	141	7934	3879	1301	271	16100	7700	1943	405	24057	11556
40.0	698	495	9879	8213	1413	983	19921	16380	1951	1440	27762	23590
46.1	714	596	10415	9437	1397	1176	20387	18593	2087	1711	30290	27226
52.2	735	671	10904	10368	1451	1301	21448	20341	2168	1976	32165	30593
58.3	739	731	11160	11126	1453	1443	21972	22207	2183	2185	33074	33086
						Exterior						
27.8	739	-158	8132	722	1481	-321	16135	1433	2138	-441	23369	2341
33.9	693	137	8551	4019	1372	268	16986	7922	2016	358	24745	11219
40.0	687	408	9425	7153	1361	819	18727	15460	2000	1242	27645	21460
46.1	689	511	9693	8365	1389	1037	19805	16939	2020	1588	29078	25560
52.2	741	629	10834	9914	1476	1273	21576	19991	2100	1921	31175	29719
58.3	732	723	11056	10986	1440	1431	21774	21704	2090	2193	32014	32853

TABLE VI

DEFLECTION 10^{-3} INCHES

X	10 psi 239 lb/in	20 psi 478 lb/in	30 psi 717 lb/in
9.5	23.3	37.8	51.1
10.5	23.3	40.0	56.7
11.5	15.6	32.2	47.8
12.5	16.7	35.6	50.0
13.5	7.8	14.4	17.8
14.5	5.6	13.3	14.4
15.5	7.8	13.3	15.6
16.5	-1.1	-2.2	-3.3
33.9	2.2	6.7	10.0
40.0	5.6	13.3	17.8
46.1	6.7	14.4	23.3
52.2	8.9	18.9	30.0
64.4	8.9	20.0	31.1
70.5	7.8	15.6	23.3
76.6	5.6	14.4	18.9
82.7	3.3	6.7	11.1

Outward deflection assumed positive.

in the model all the characteristics of the prototype, such as shape, types of connections between the different parts, initial stresses due to welding or forming.

Against these very convenient features, the reduction in scale introduces an appreciable economy in time and cost of the study. Besides these two factors, observations can be more precisely made in a reduced scale model, and the forces can be reproduced with higher accuracy. Another factor is the possibility of repeating the test and changing shapes on account of the experience gained through previous models. This possibility is highly restricted if the one-to-one scale is selected. Consequently, the more reduced the scale, the cheaper and quicker the analysis, and more models can be analyzed. Of course, if we reduce the scale it becomes more difficult to reproduce the details of the prototype.

In the problem described in this report the selected scale and the changes introduced in the model to simulate the prototype proved to be successful. The model yielded results that, within a satisfactory degree of accuracy, confirmed the mathematical model selected to represent the actual structure.

We consider this result extremely valuable in the light of the present tendency to design larger boosters than the ones used at present. A well-organized program on reduced scale models could lead to substantial savings in the cost of research and development of these structures.

Bibliography

[1] Hetényi, M., "Beams On Elastic Foundations," Ann Arbor: The University of Michigan Press, 1946.

[2] Durelli, A. J., Daily, G. W., and Morse, S., "Experimental Study of Large-diameter Thin-wall Pressure Vessels," Proceedings of SESA, Vol. XVIII, No. 1, 1961, p. 33.

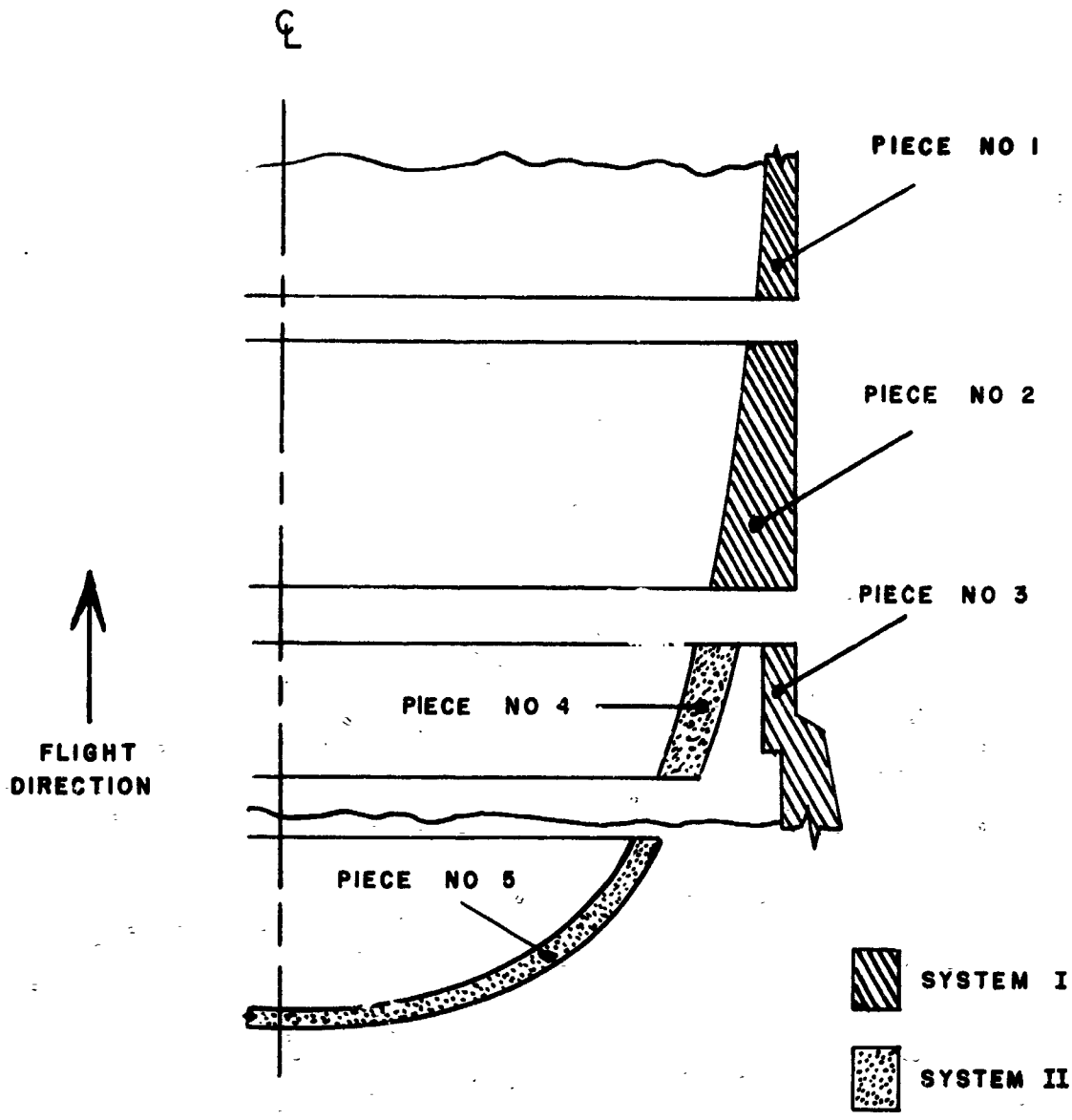

FIG. I. The Individual Shell Components of the Substitute Tank Underlying the Analysis

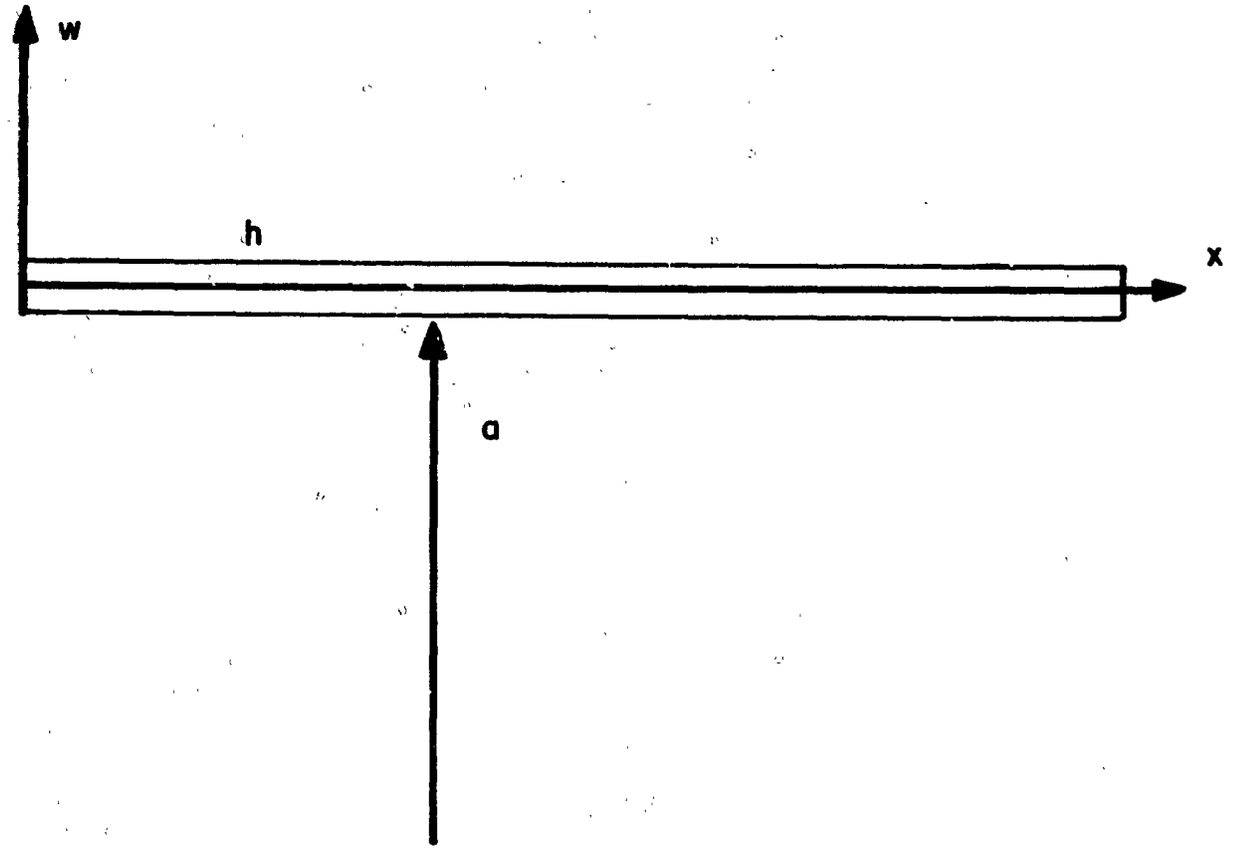

Figure 2. System of Coordinates Utilized For The Shell Components

FIGURE 3. SIMULATION OF THE ELASTIC FOUNDATION BY MEANS OF YELLOW BRASS CANTILEVER BEAMS.

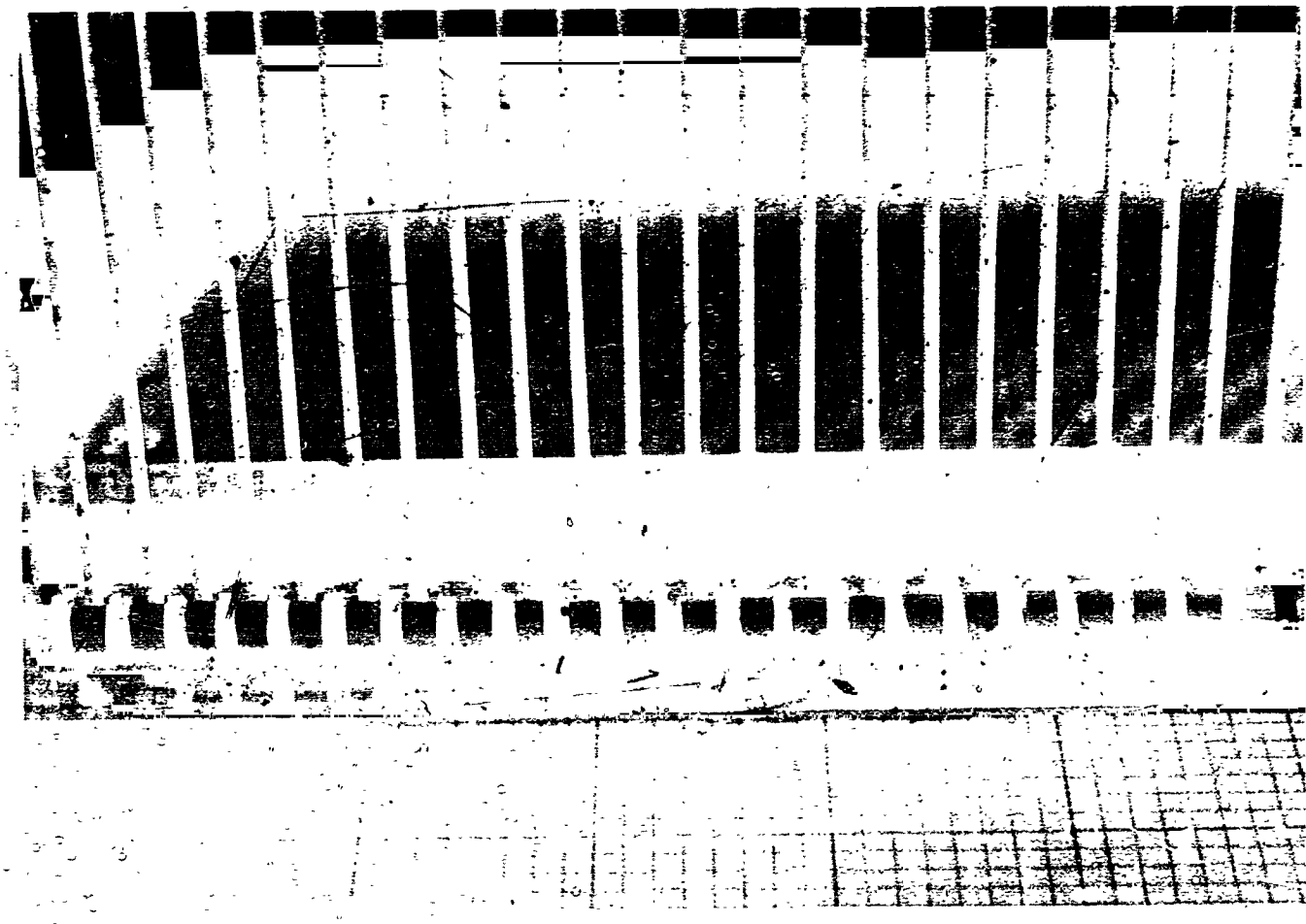

FIGURE 4. SYSTEM USED TO CONNECT THE BRASS WIRES TO THE BEAM.

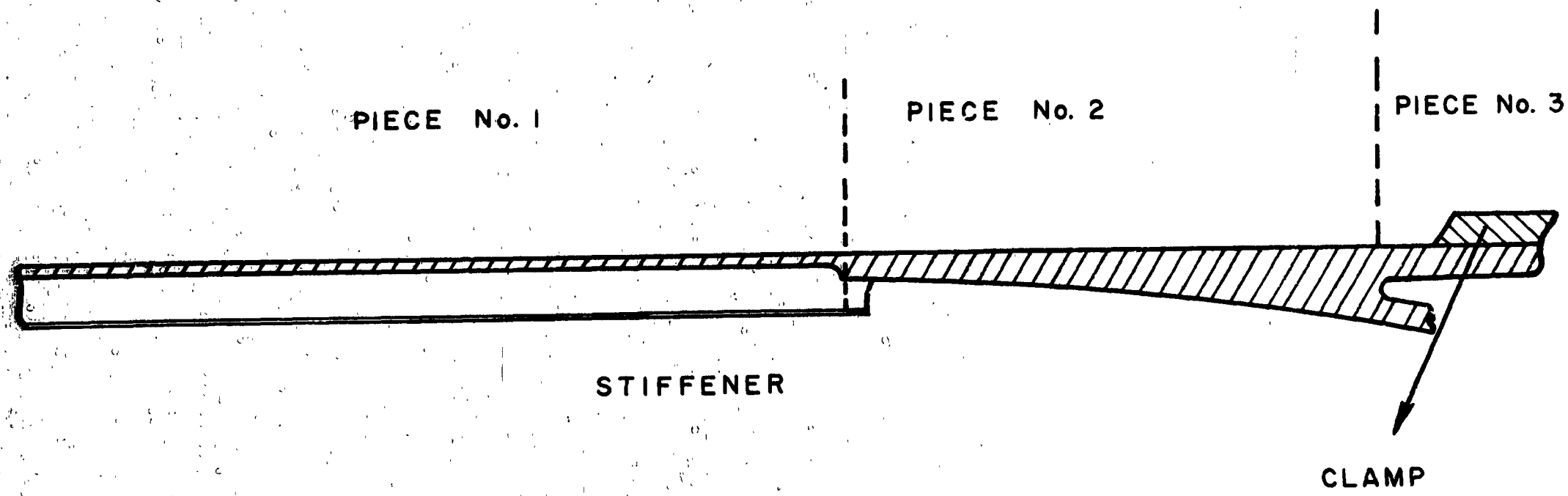

Figure 5. Regions Corresponding to the "Y-Ring Model

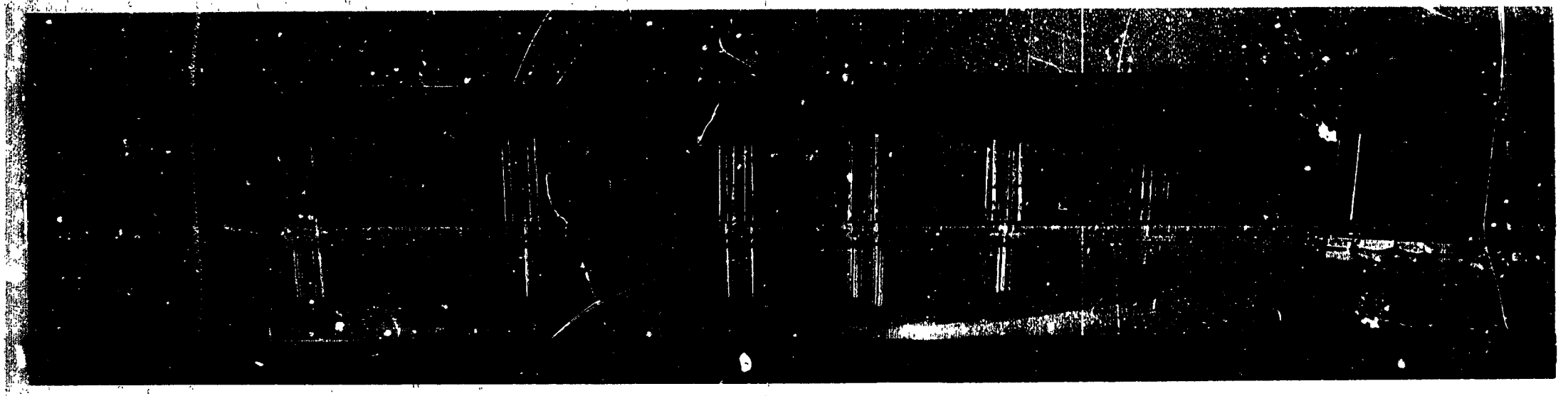

FIGURE 6. VIEW OF THE ELASTIC FOUNDATION SHOWING THE DIFFERENT REGIONS.

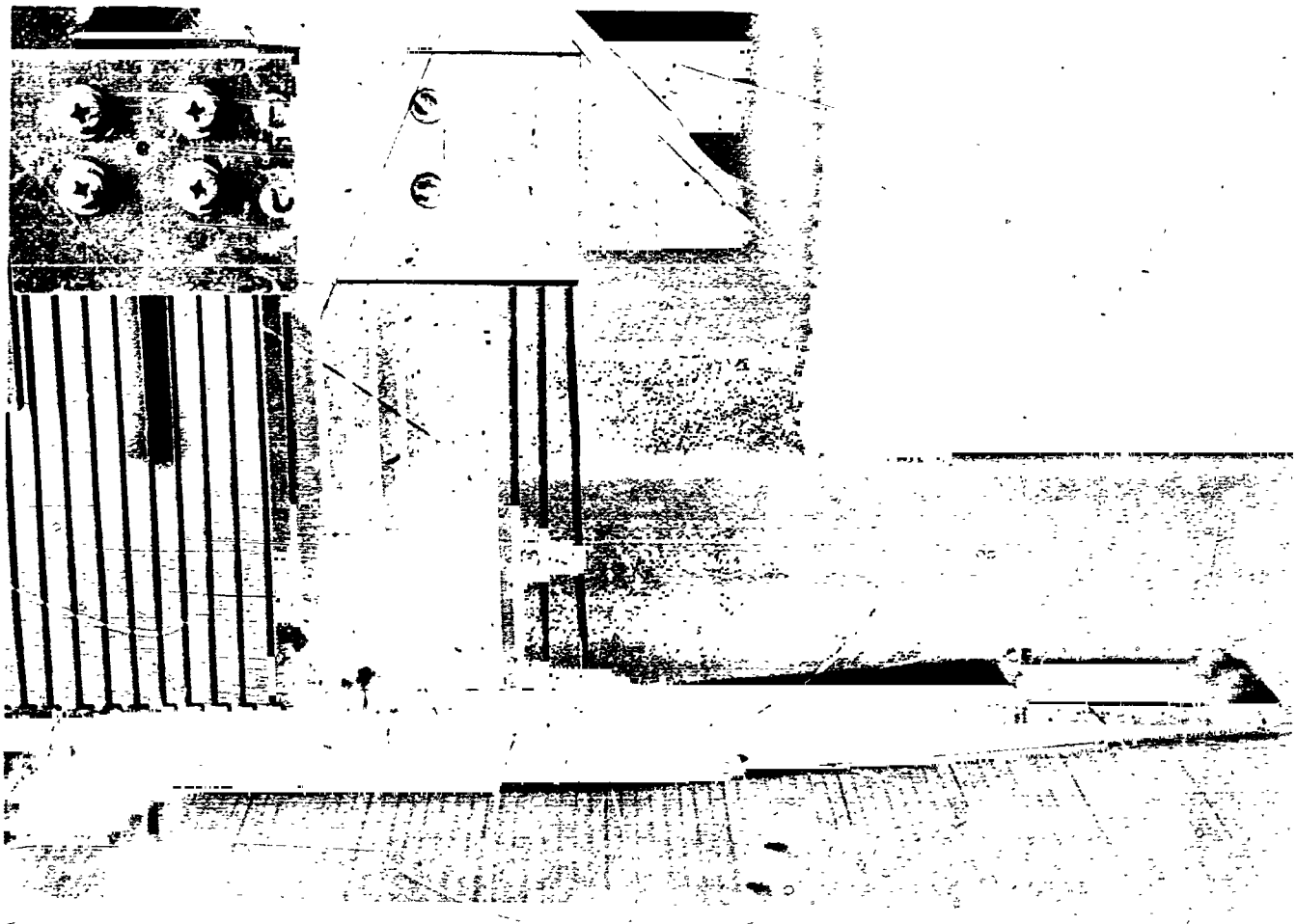

FIGURE 7. CLAMPED END OF THE MODEL.

FIGURE 8. TOP VIEW OF THE MODEL.

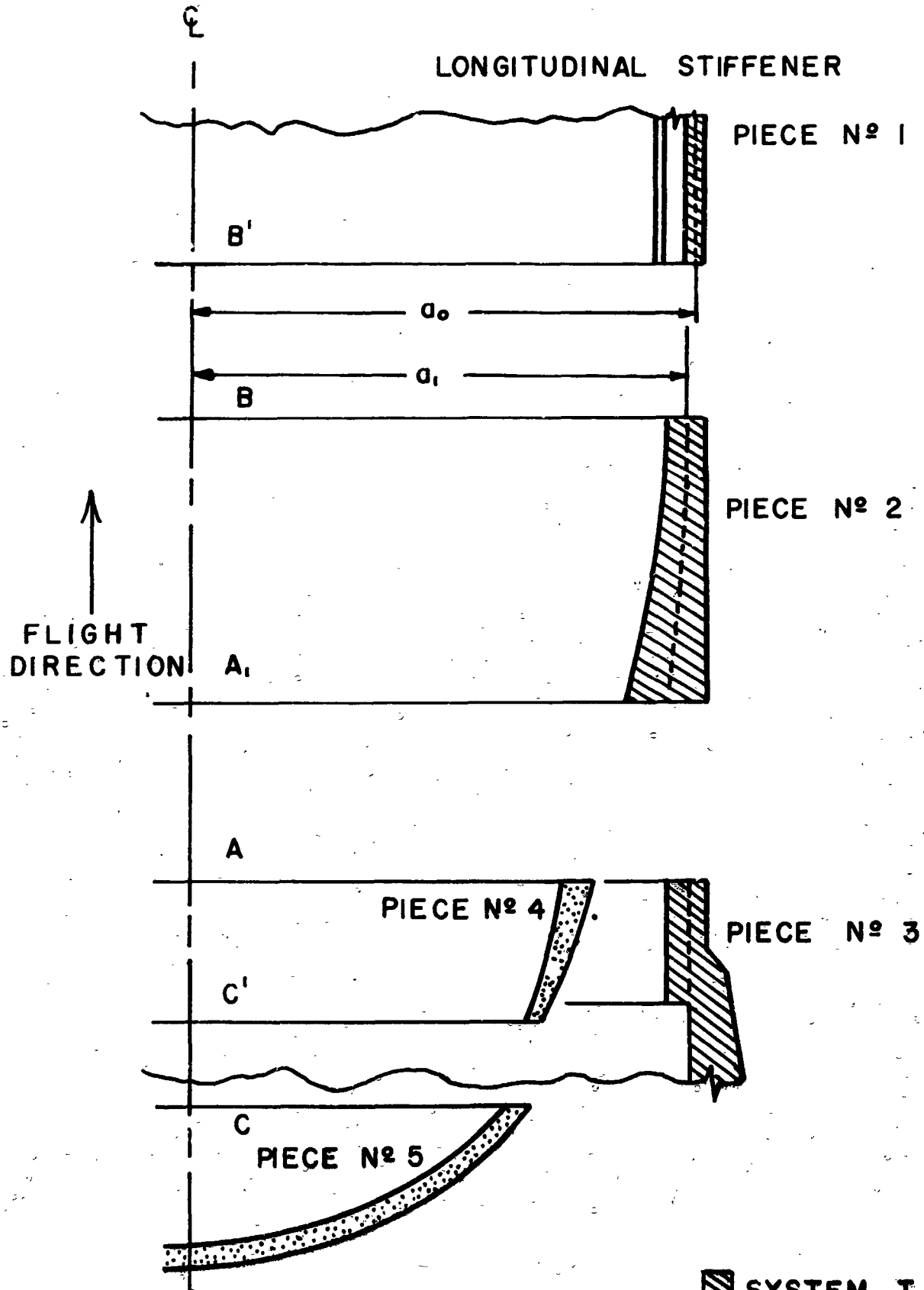

Figure 9. The Two Principal Systems.

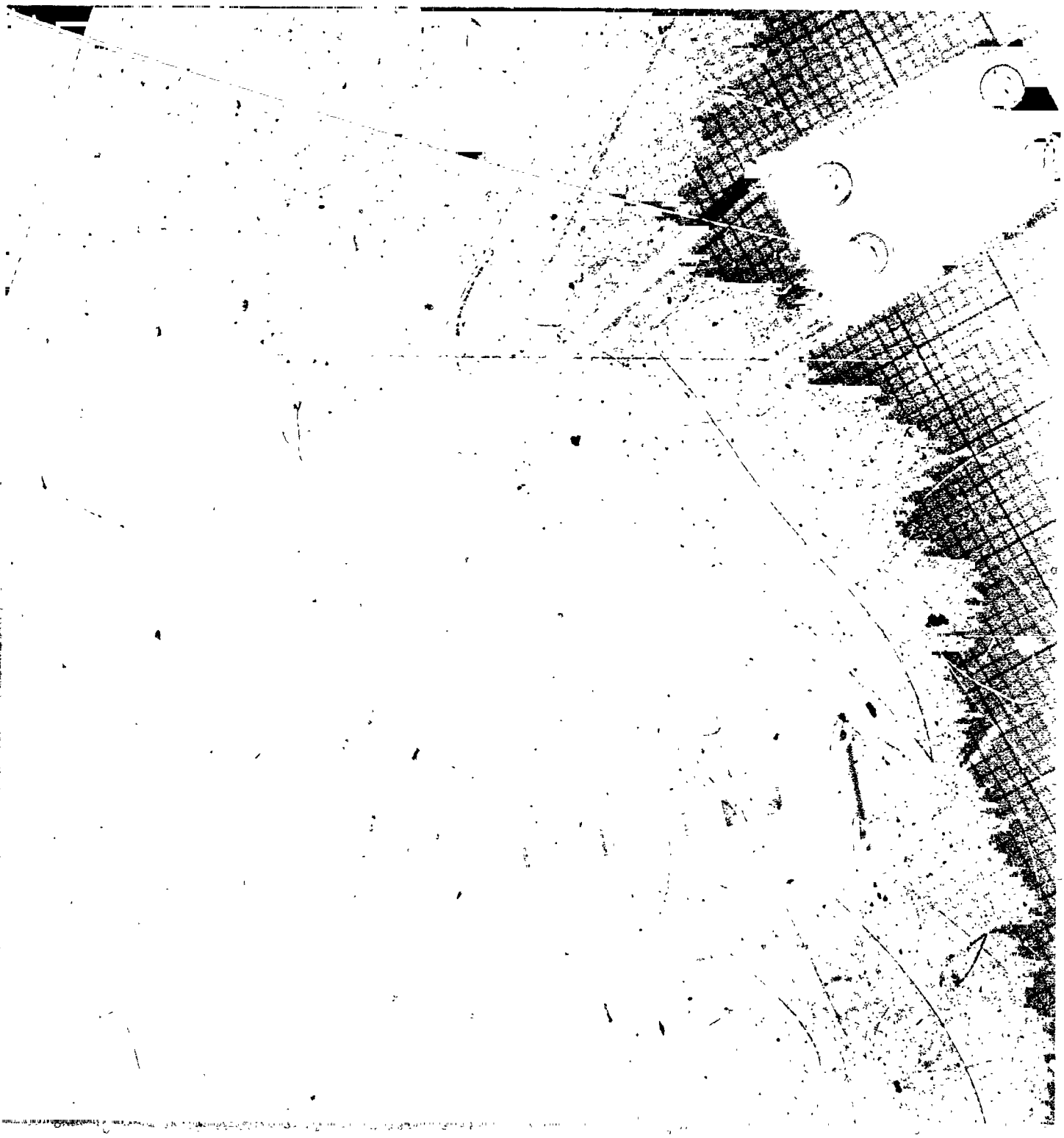

FIGURE 10. SPRING-BALANCE

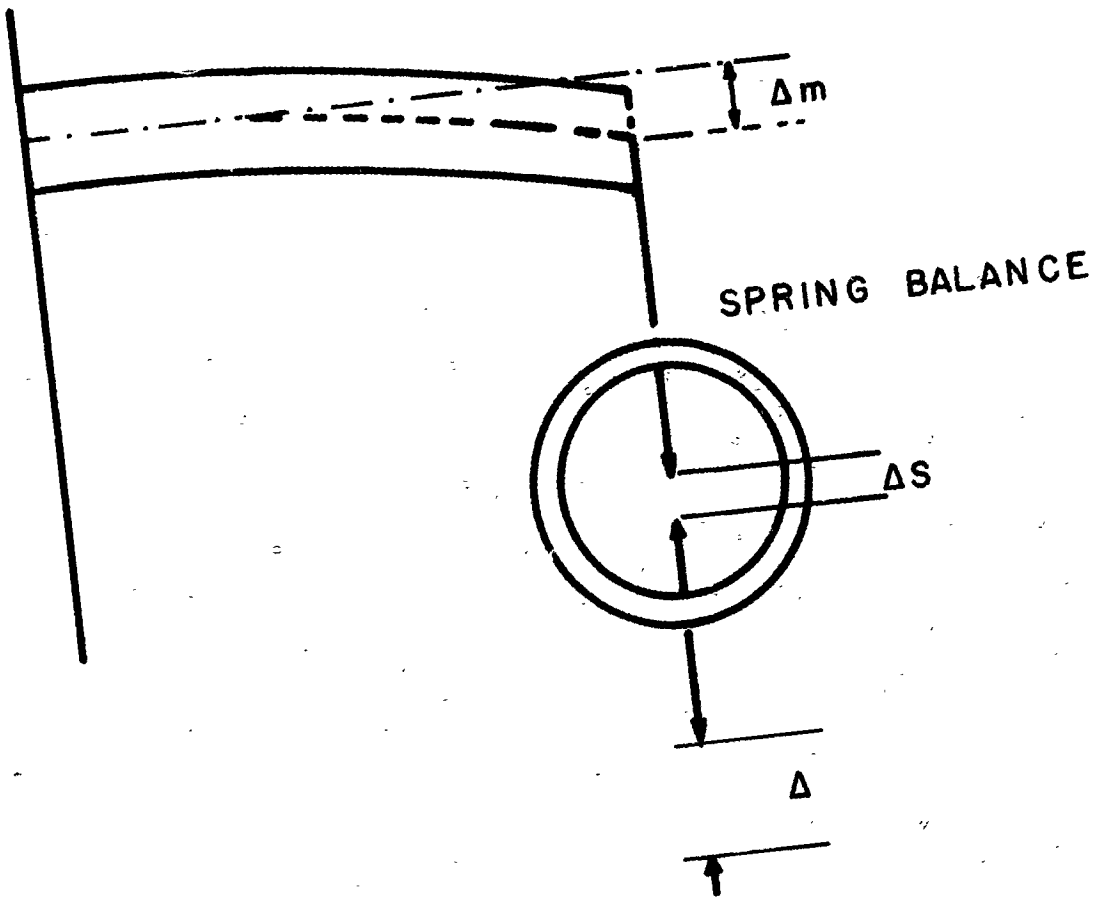

Figure II
Schematic Representation of the System Used to Calibrate the Spring—Balances

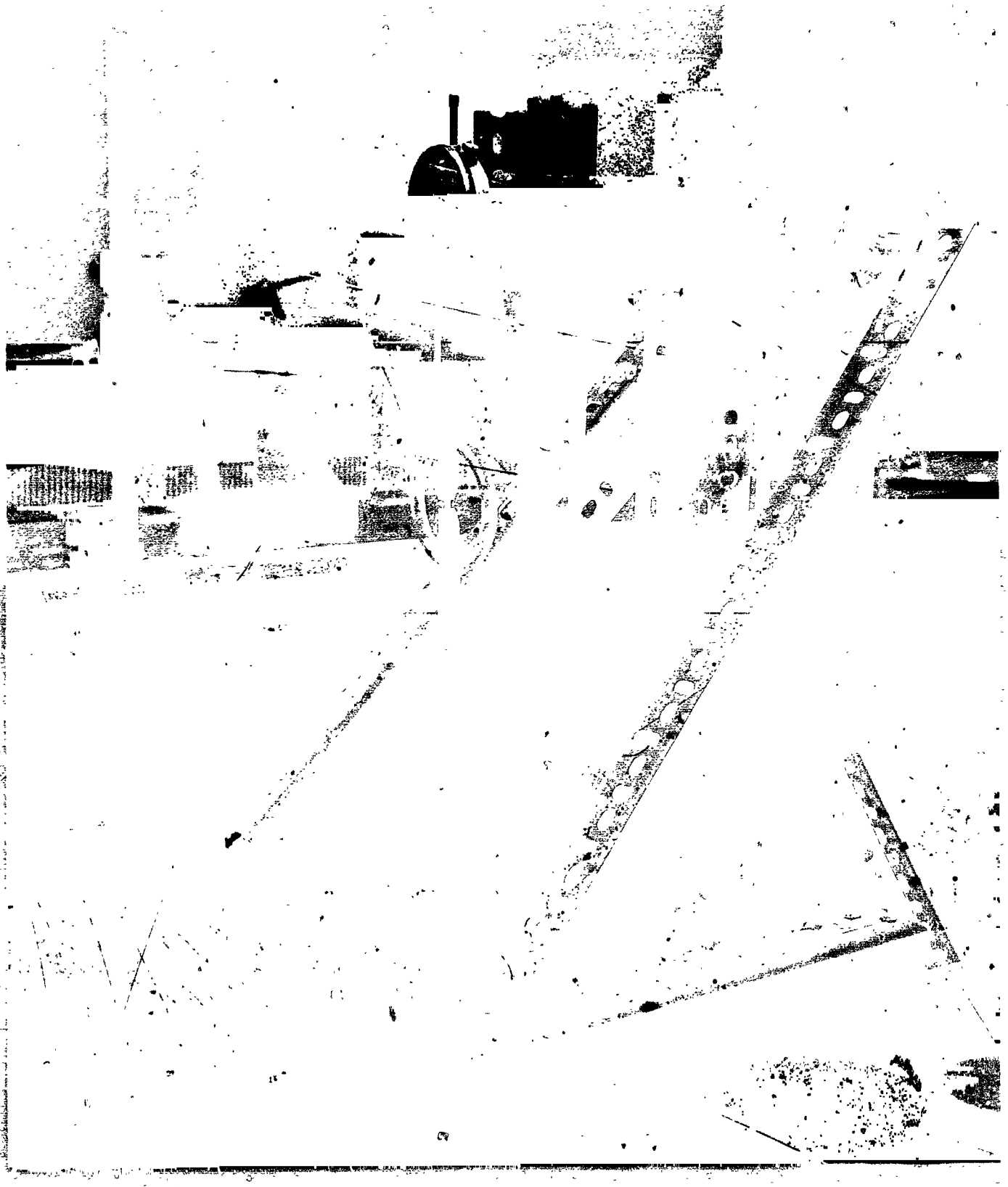

FIGURE 12. PICTURE OF THE SYSTEM USED TO CALIBRATE THE SPRING-BALANCES.

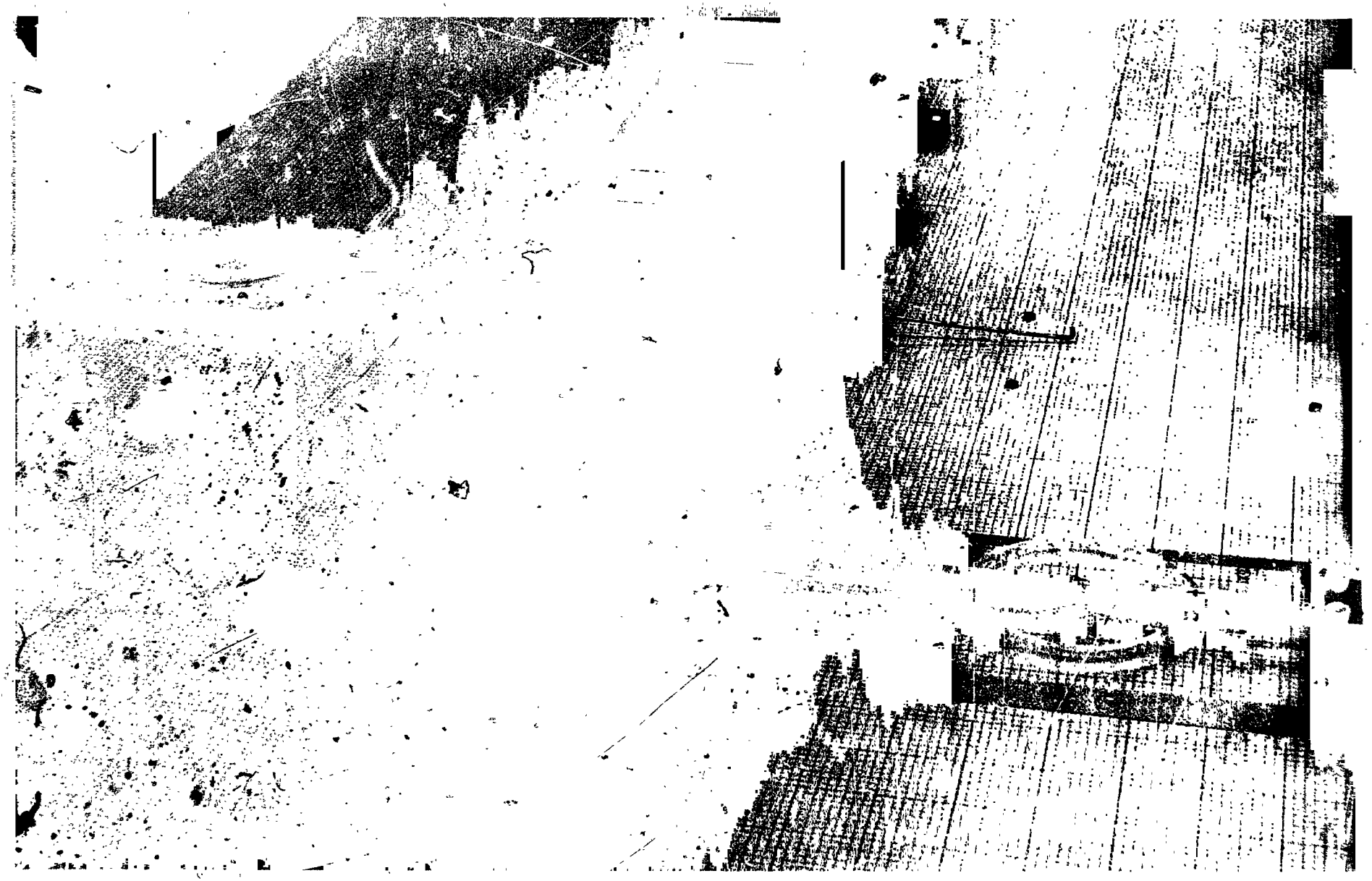

FIGURE 13. DEVICE USED TO APPLY A COUPLE.

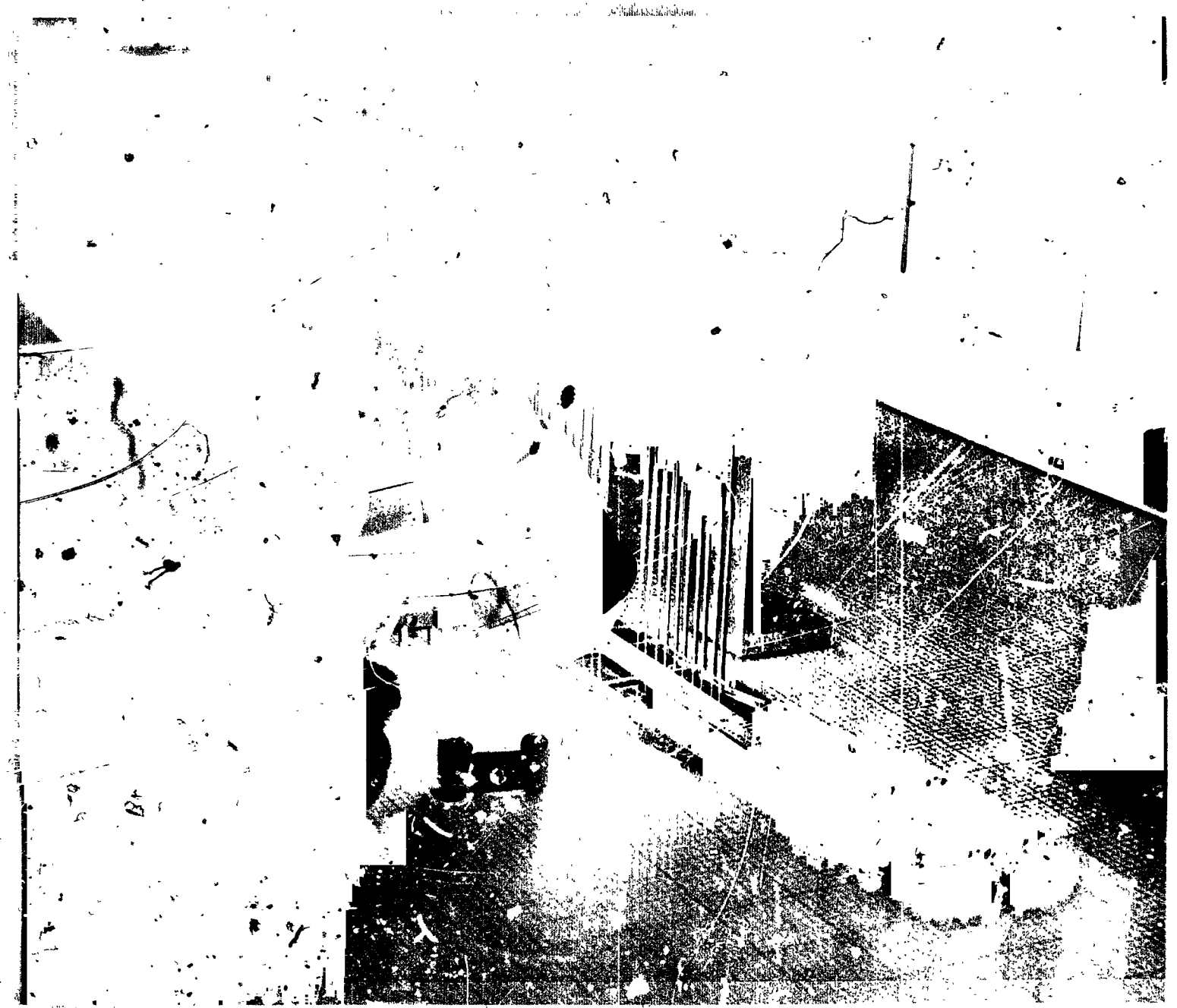

FIGURE 14. ILLUSTRATION SHOWING THE PROCEDURE FOLLOWED TO LOCATE FRINGE POSITION.

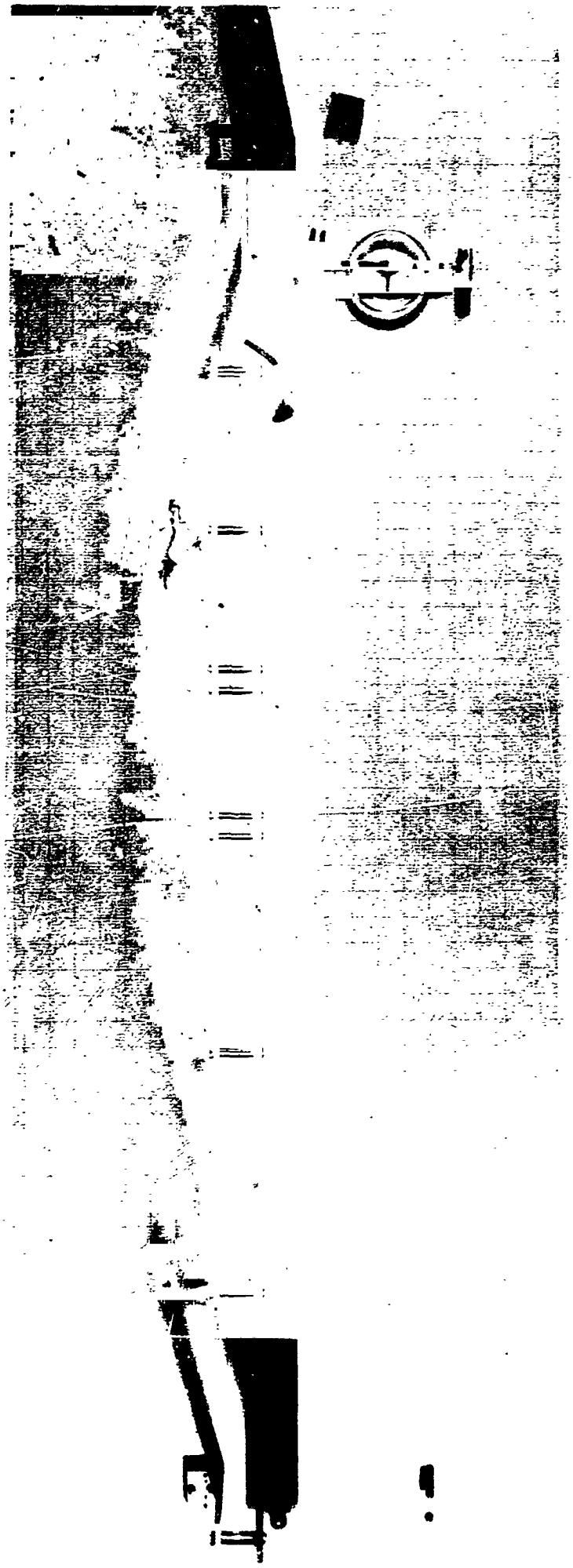

FIGURE 15. MOIRE PATTERN CORRESPONDING TO ONE STATE OF LOADING.

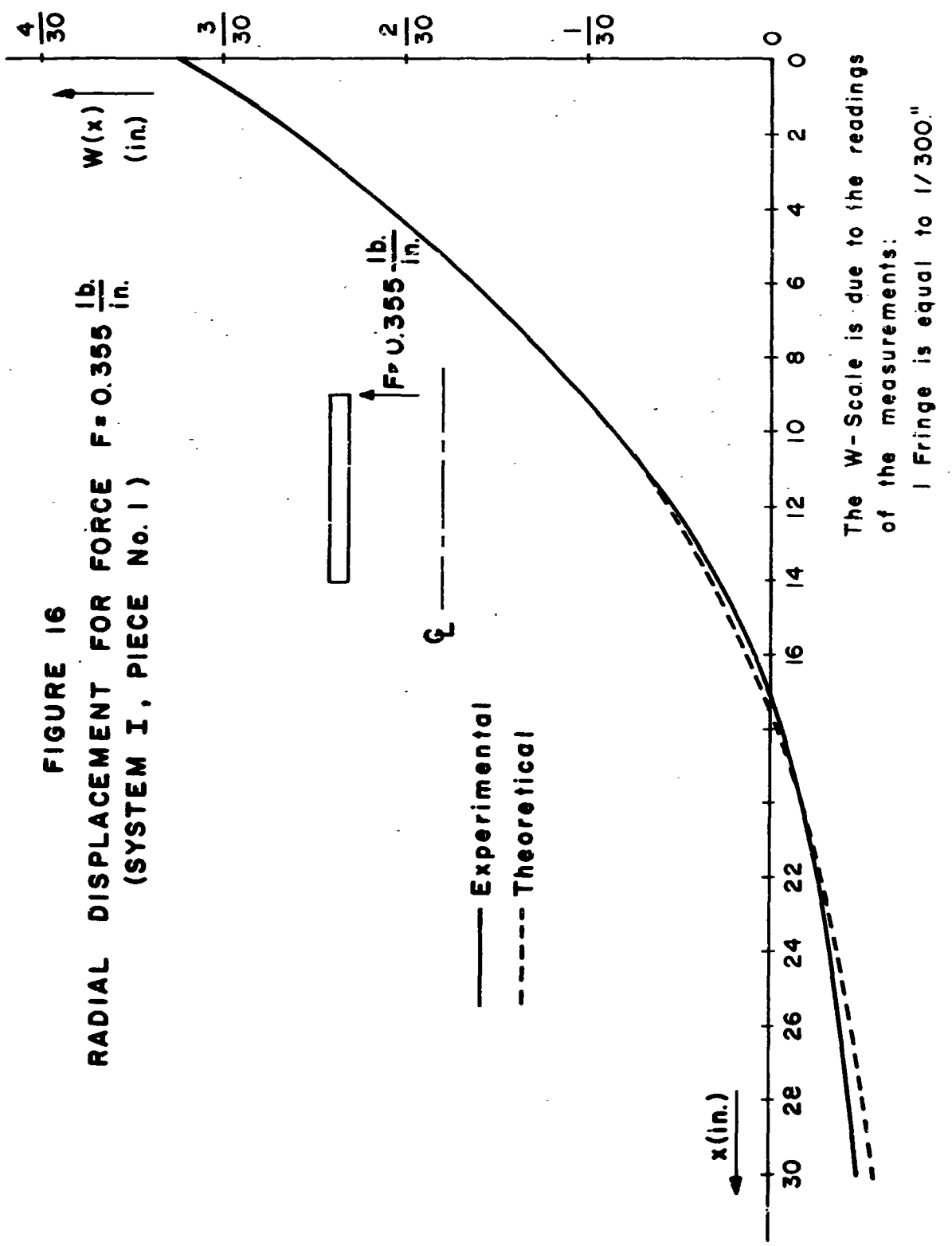

FIGURE 16
RADIAL DISPLACEMENT FOR FORCE F = 0.355 lb./in.
(SYSTEM I, PIECE No. 1)

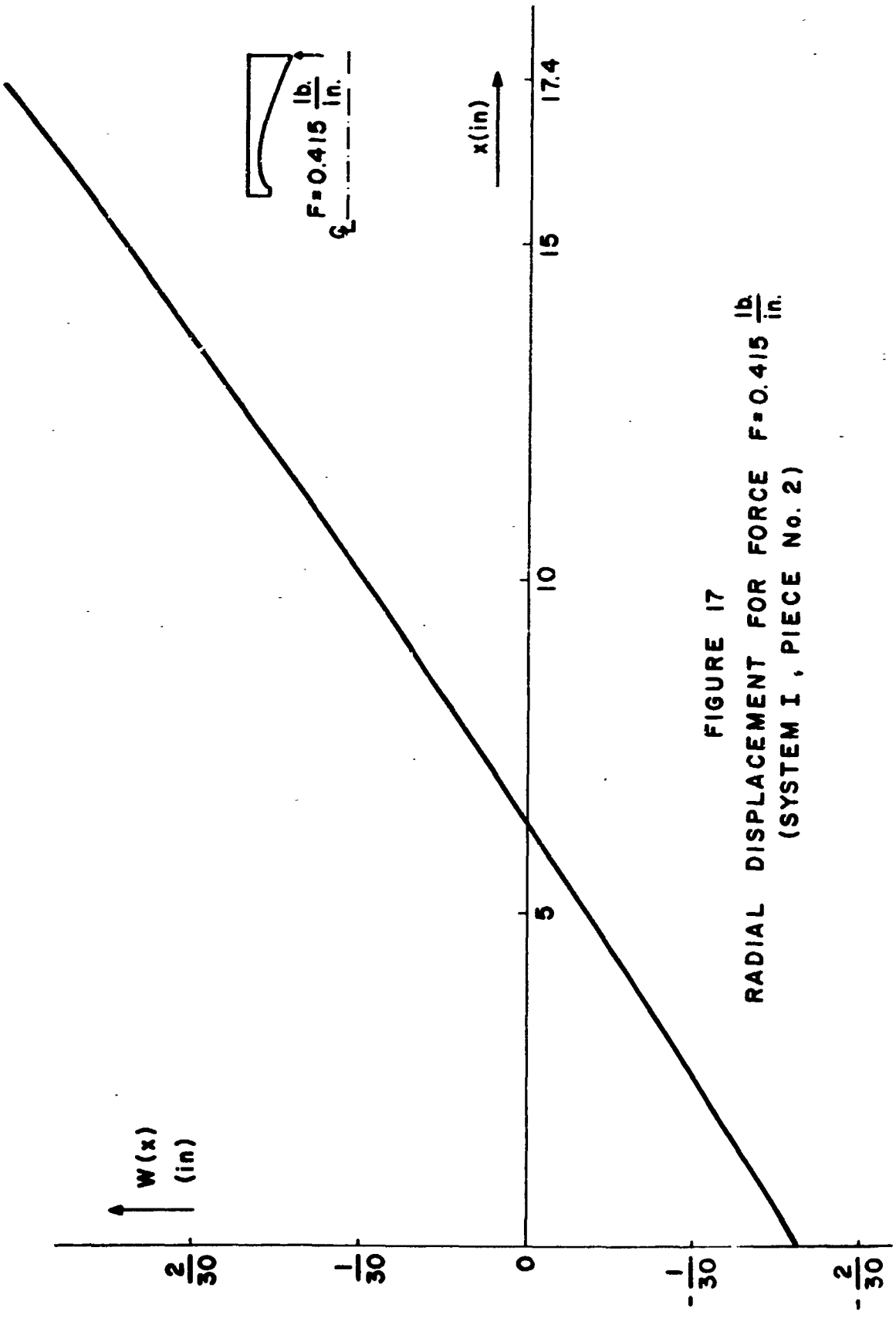

FIGURE 17
RADIAL DISPLACEMENT FOR FORCE F=0.415 $\frac{lb.}{in.}$
(SYSTEM I, PIECE No. 2)

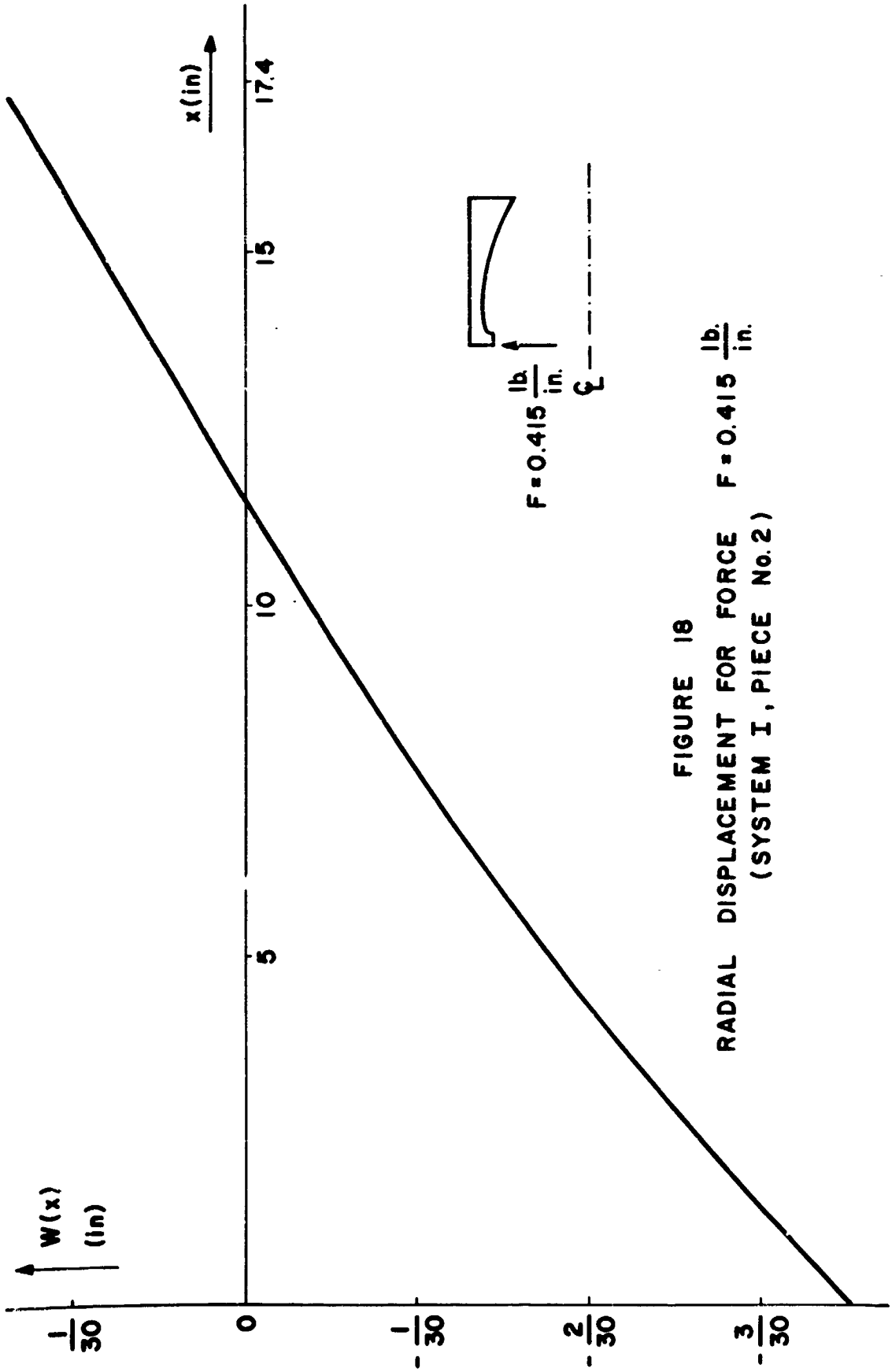

FIGURE 18
RADIAL DISPLACEMENT FOR FORCE (SYSTEM I, PIECE No. 2)

FIGURE 19

RADIAL DISPLACEMENT FOR COUPLE $M = 2.462 \frac{lb.\,in.}{in.}$
(SYSTEM I, PIECE No. 2)

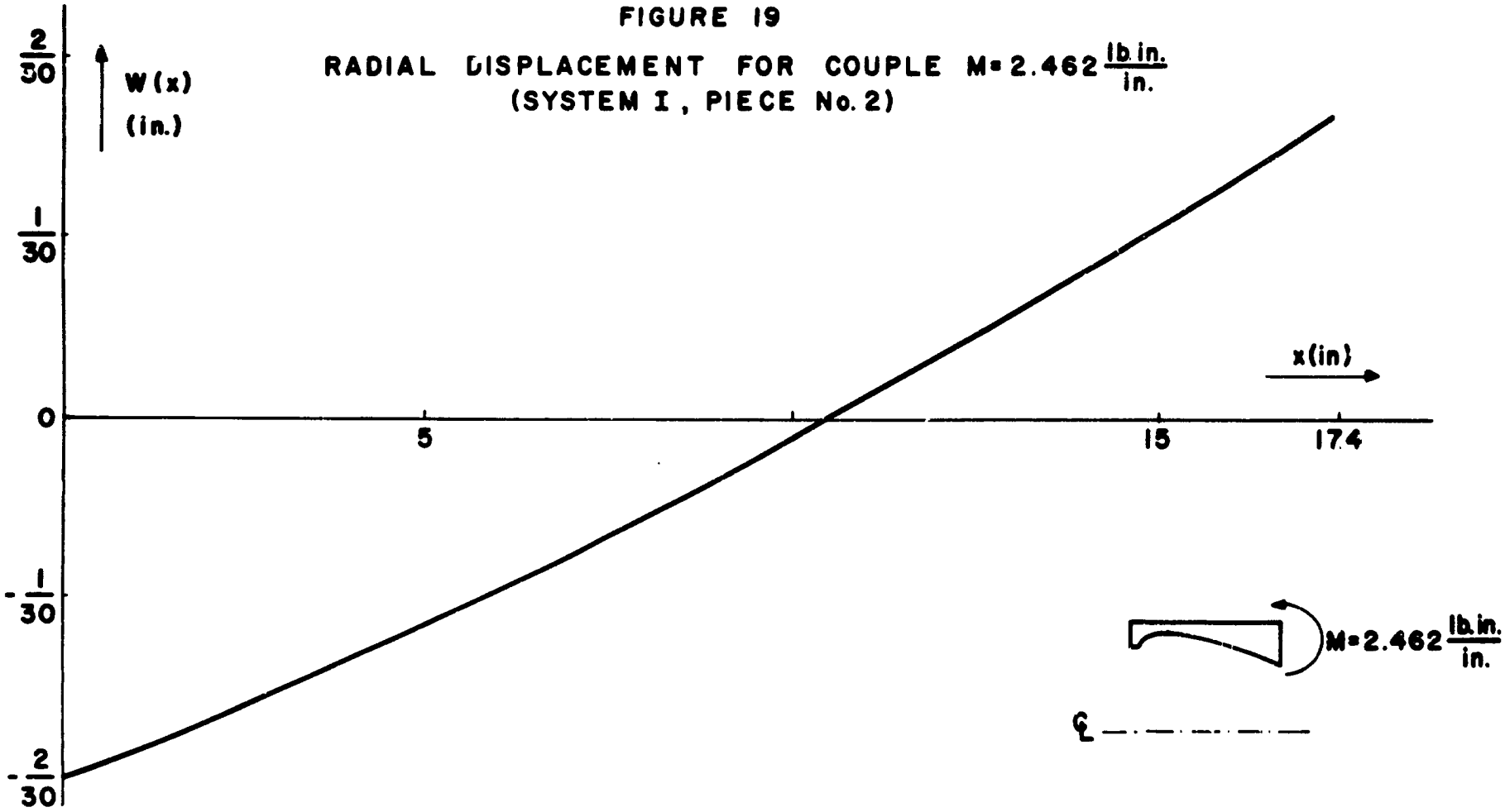

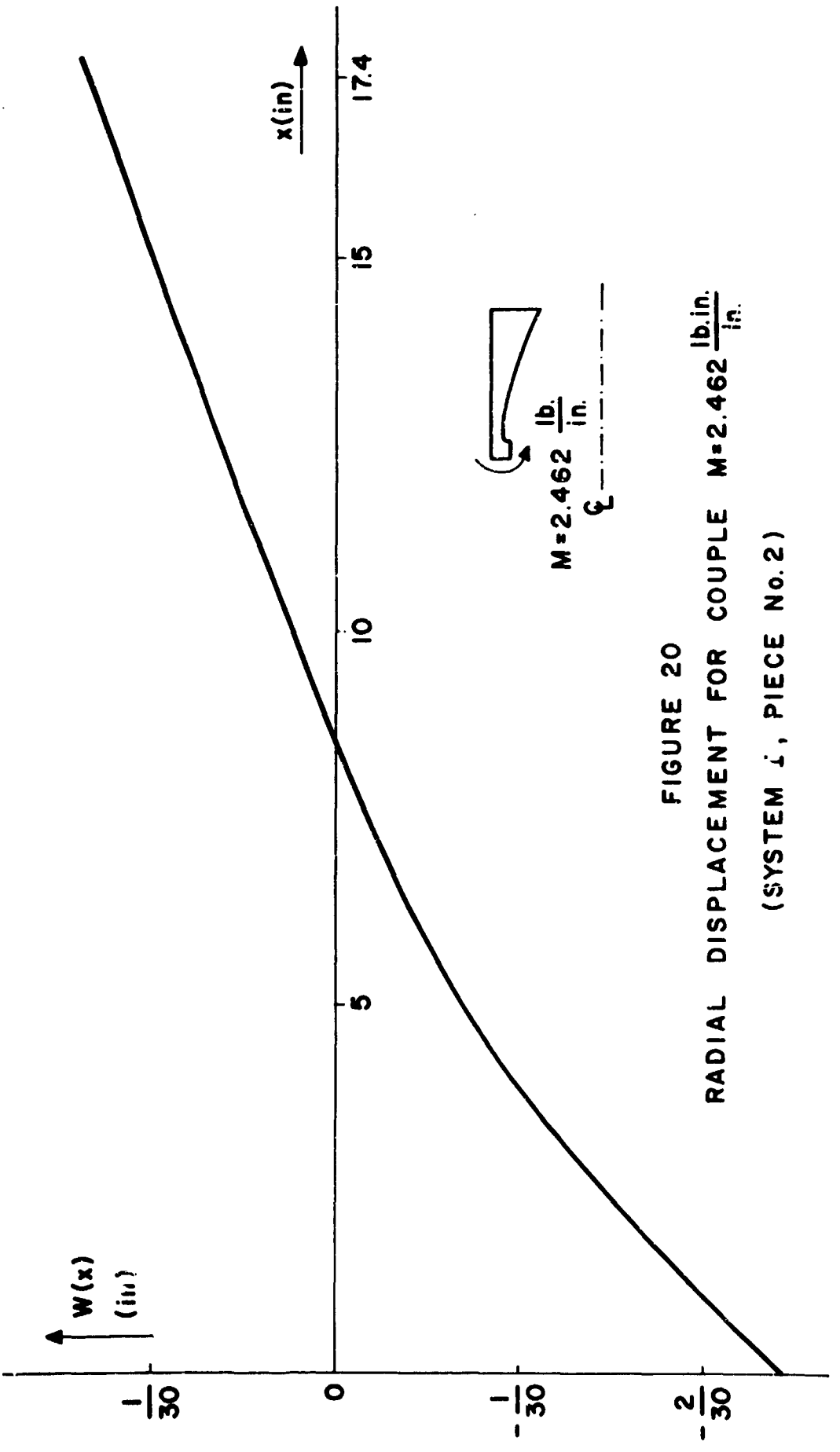

FIGURE 20

RADIAL DISPLACEMENT FOR COUPLE M=2.462 $\frac{lb.in.}{in.}$

(SYSTEM 1, PIECE No. 2)

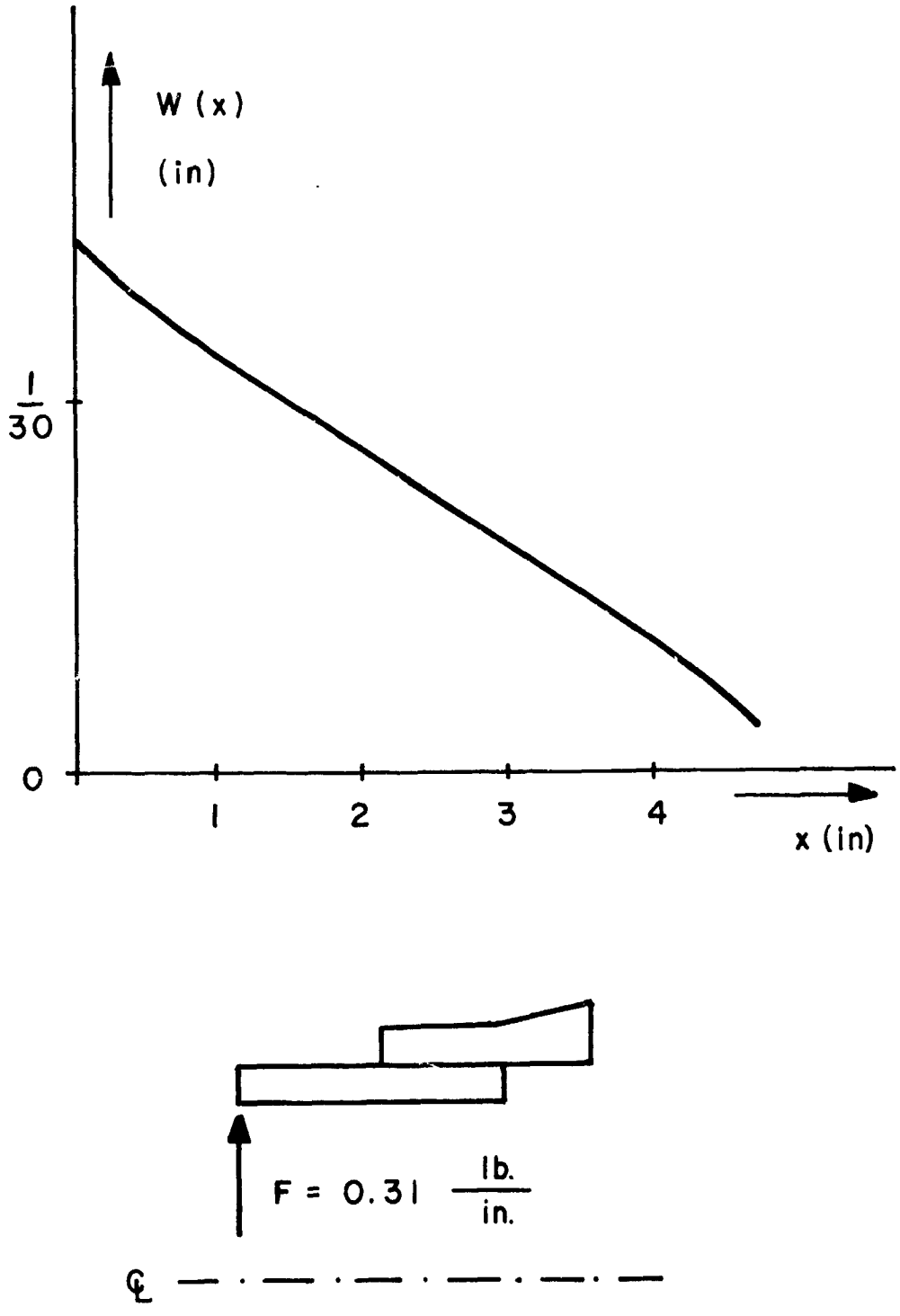

Figure 21. Radical Displacements
(System I, Piece Nº 3)

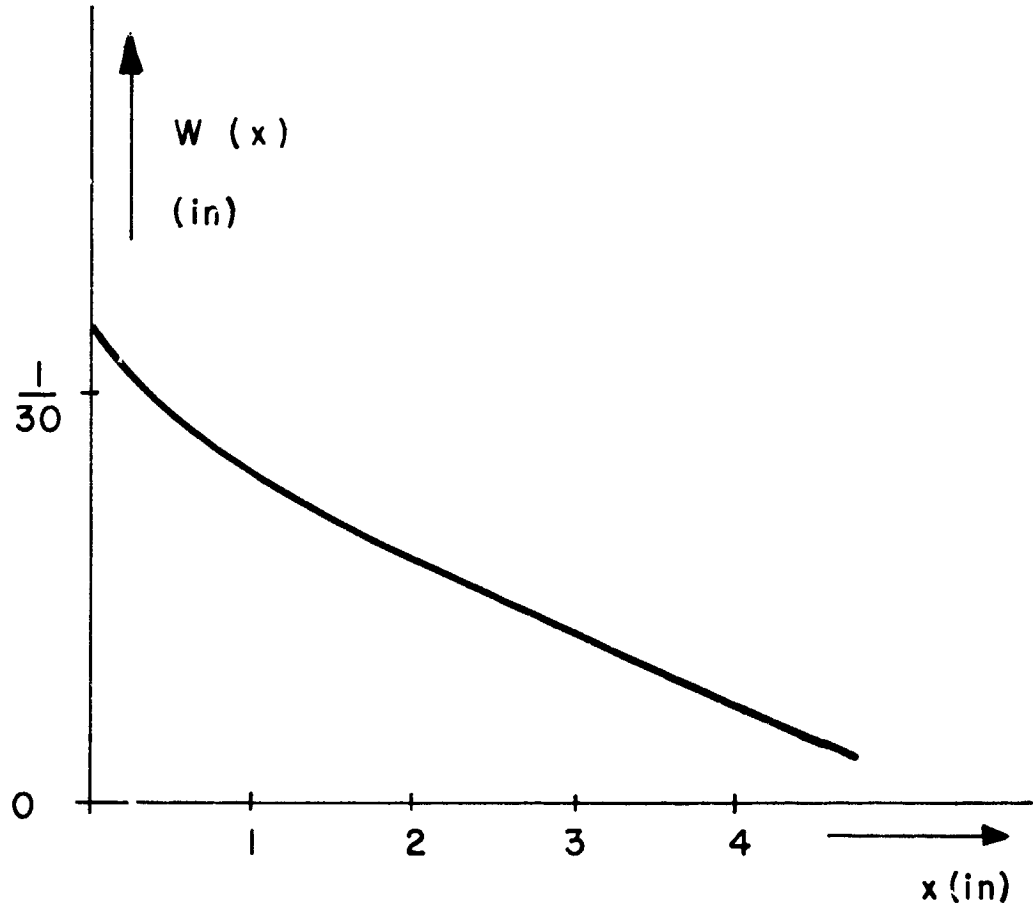

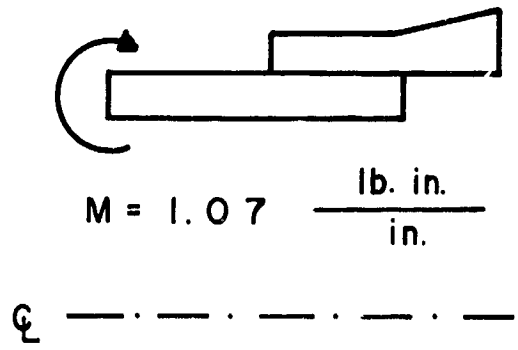

Figure 22. Radical Displacements
(System I, Piece Nº 3)

FIG. 23. Moment Distribution for Edge Force $Q_1 = +1$

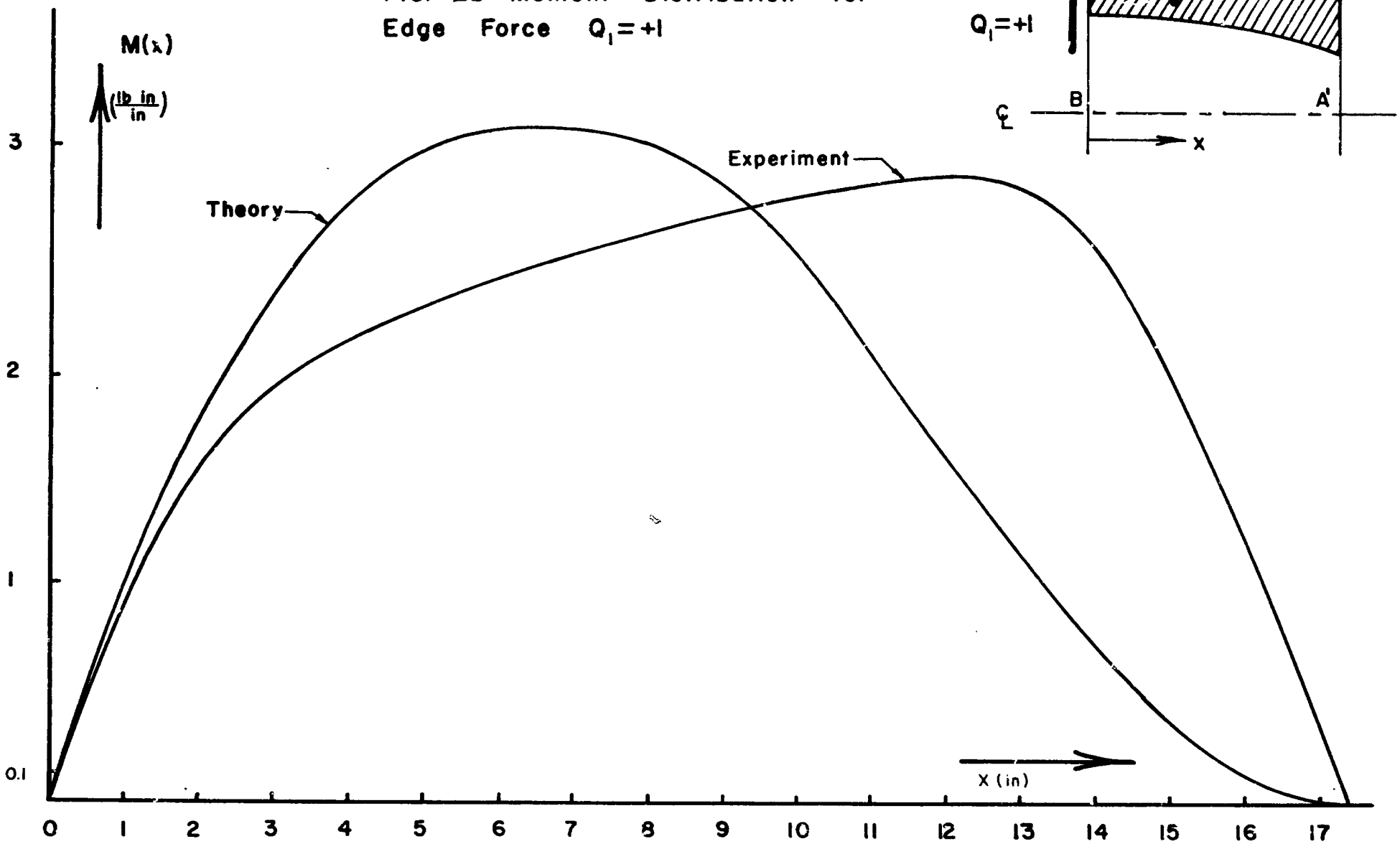

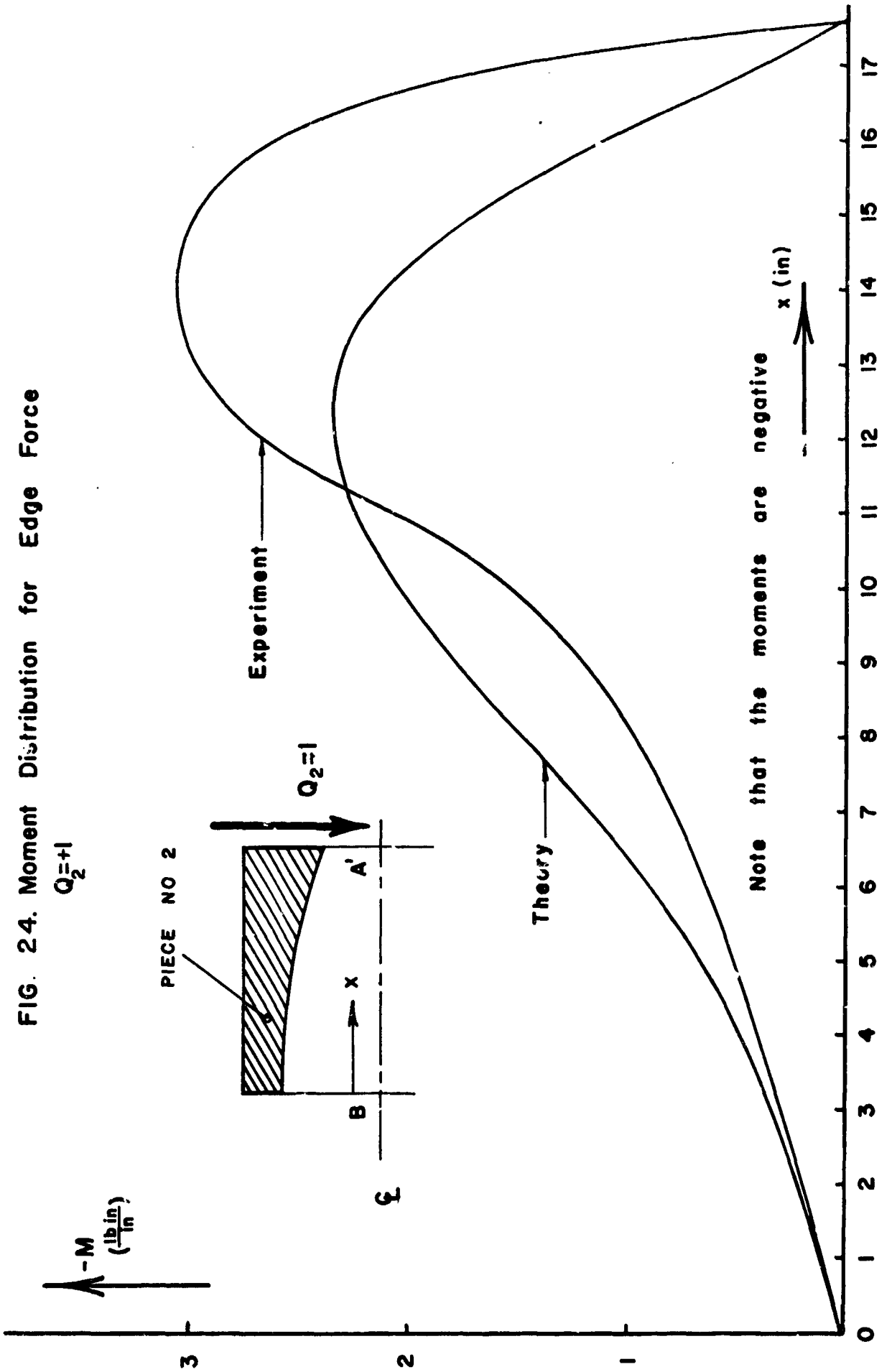

FIG. 24. Moment Distribution for Edge Force

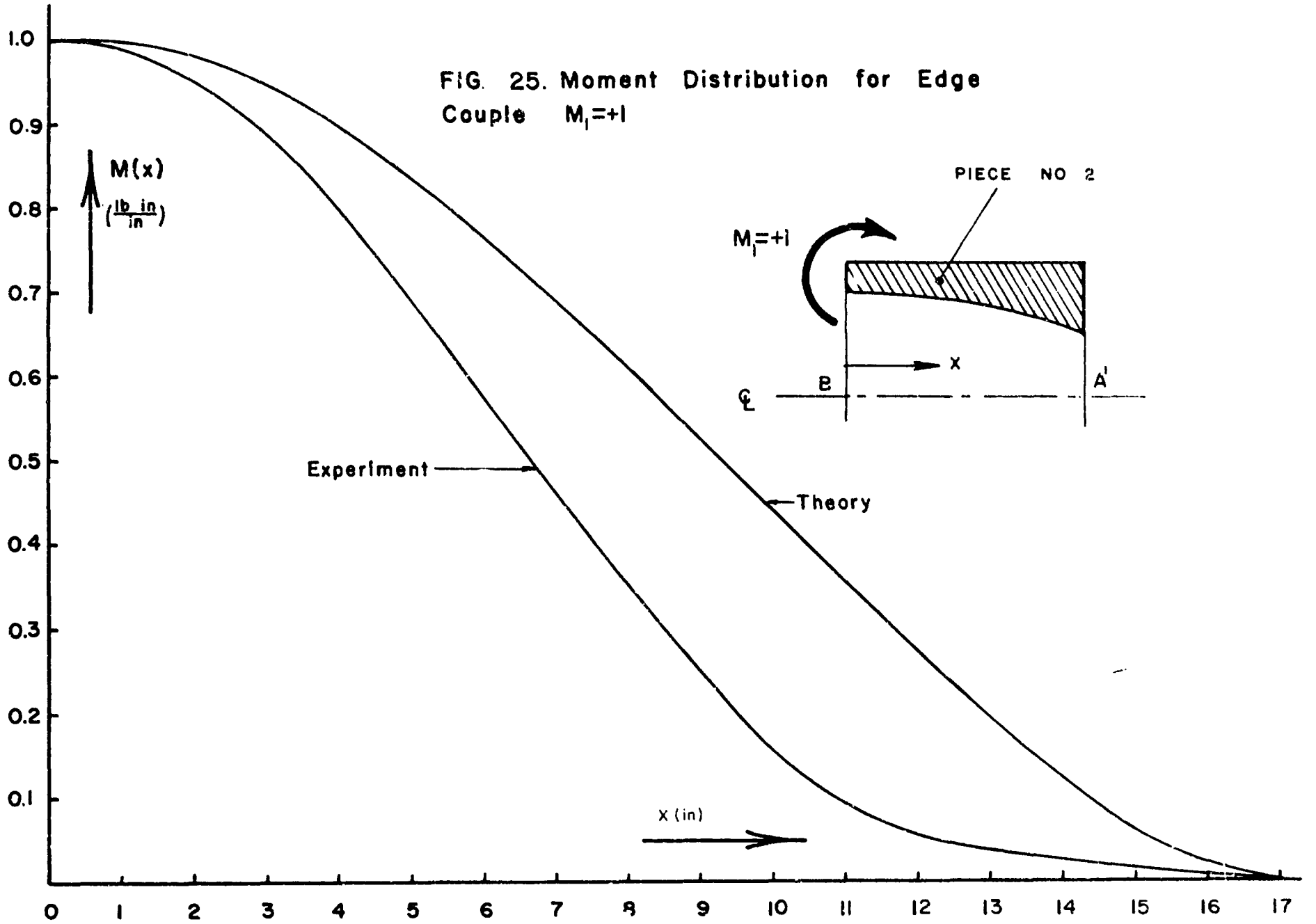
FIG. 25. Moment Distribution for Edge Couple $M_1=+1$
M(x)
$(\frac{lb\ in}{in})$
1.0
0.9
0.8
0.7
0.6
0.5
0.4
0.3
0.2
0.1
0
1
2
3
4
5
6
7
8
9
10
11
12
13
14
15
16
17
X (in)
Experiment
Theory
PIECE NO 2
$M_1=+1$
X
B
A'
℄

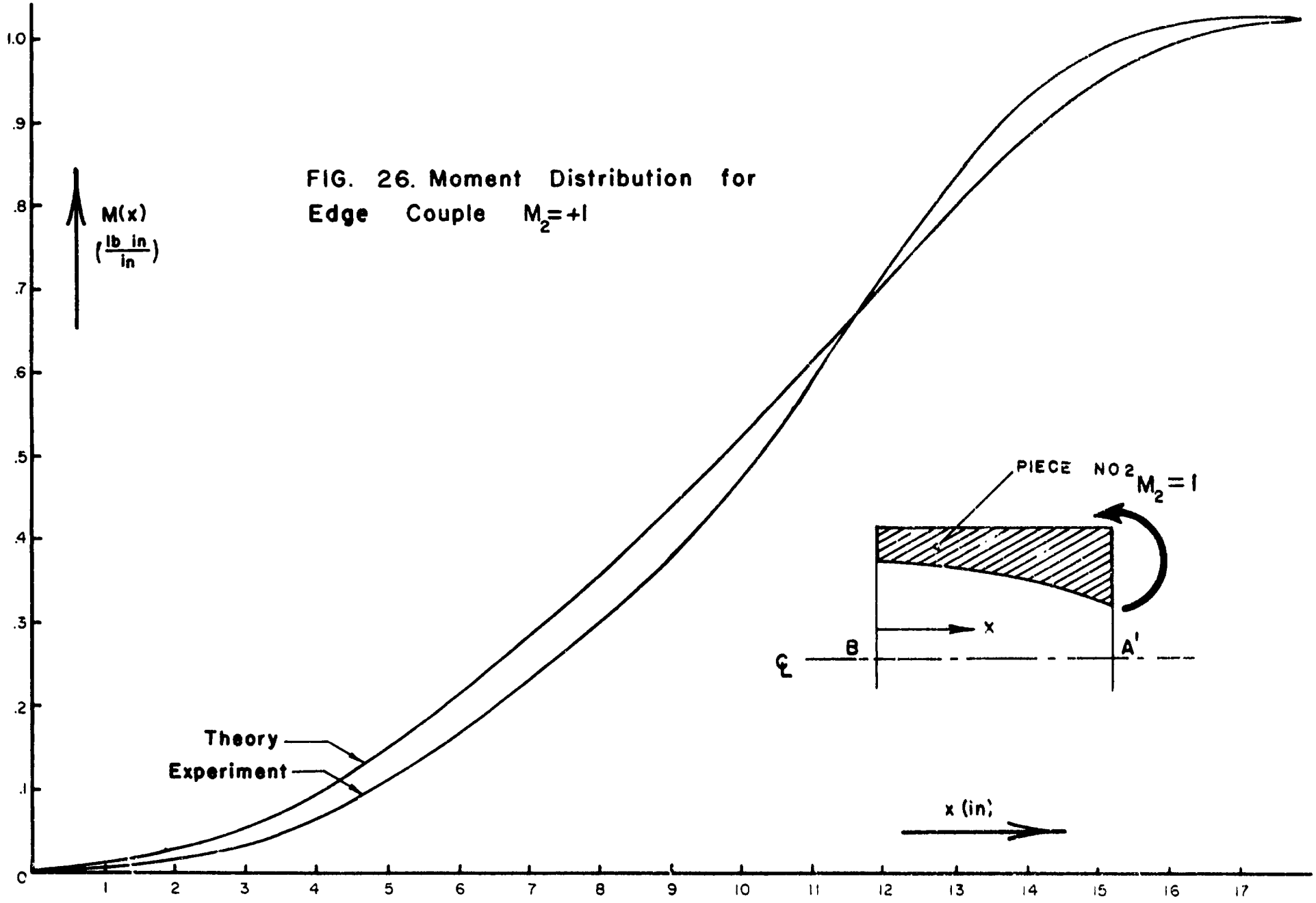

FIG. 26. Moment Distribution for Edge Couple $M_2 = +1$

FIG. 27. Moment Distribution for Edge Force $F_3 = +1$

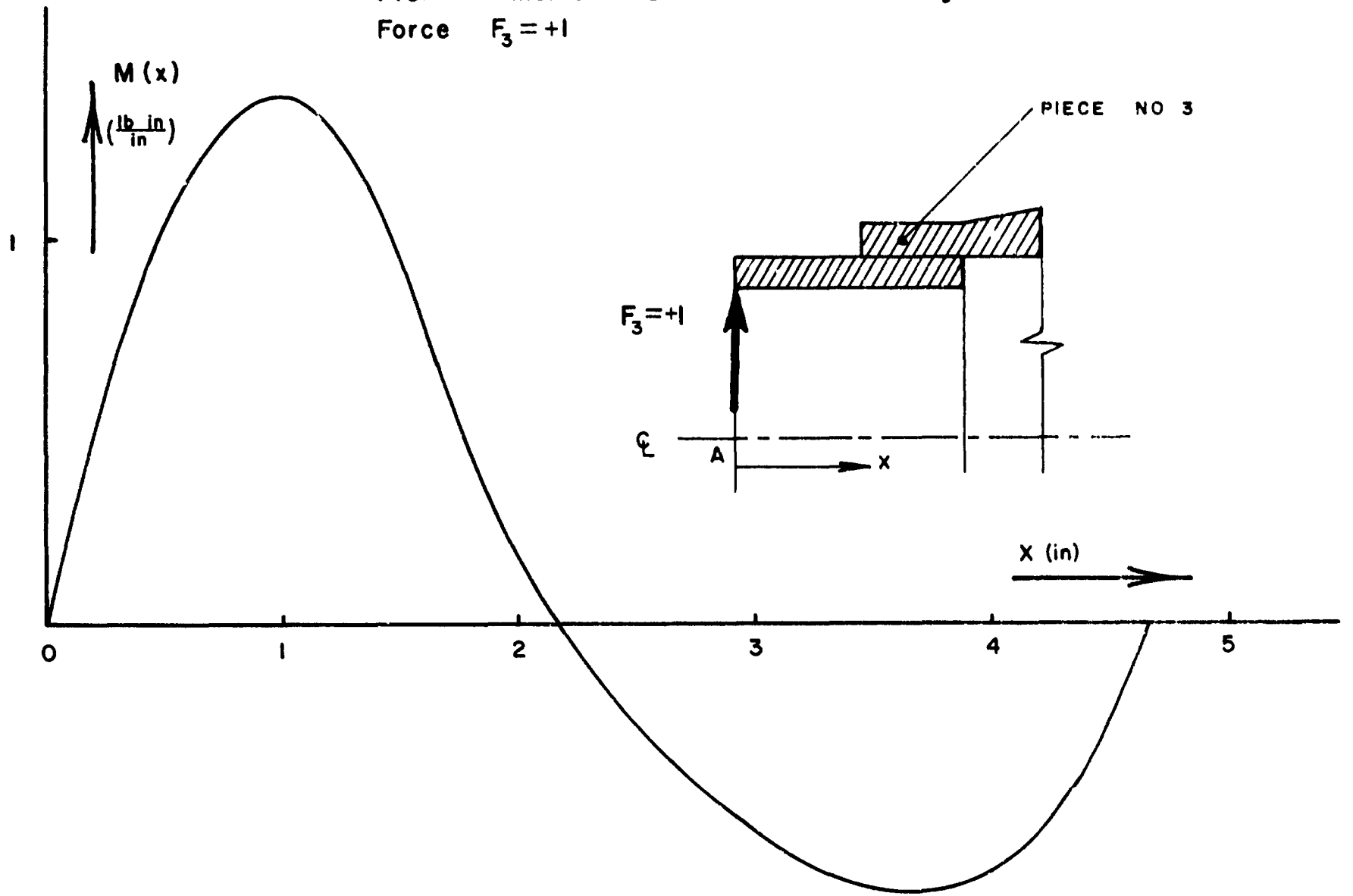

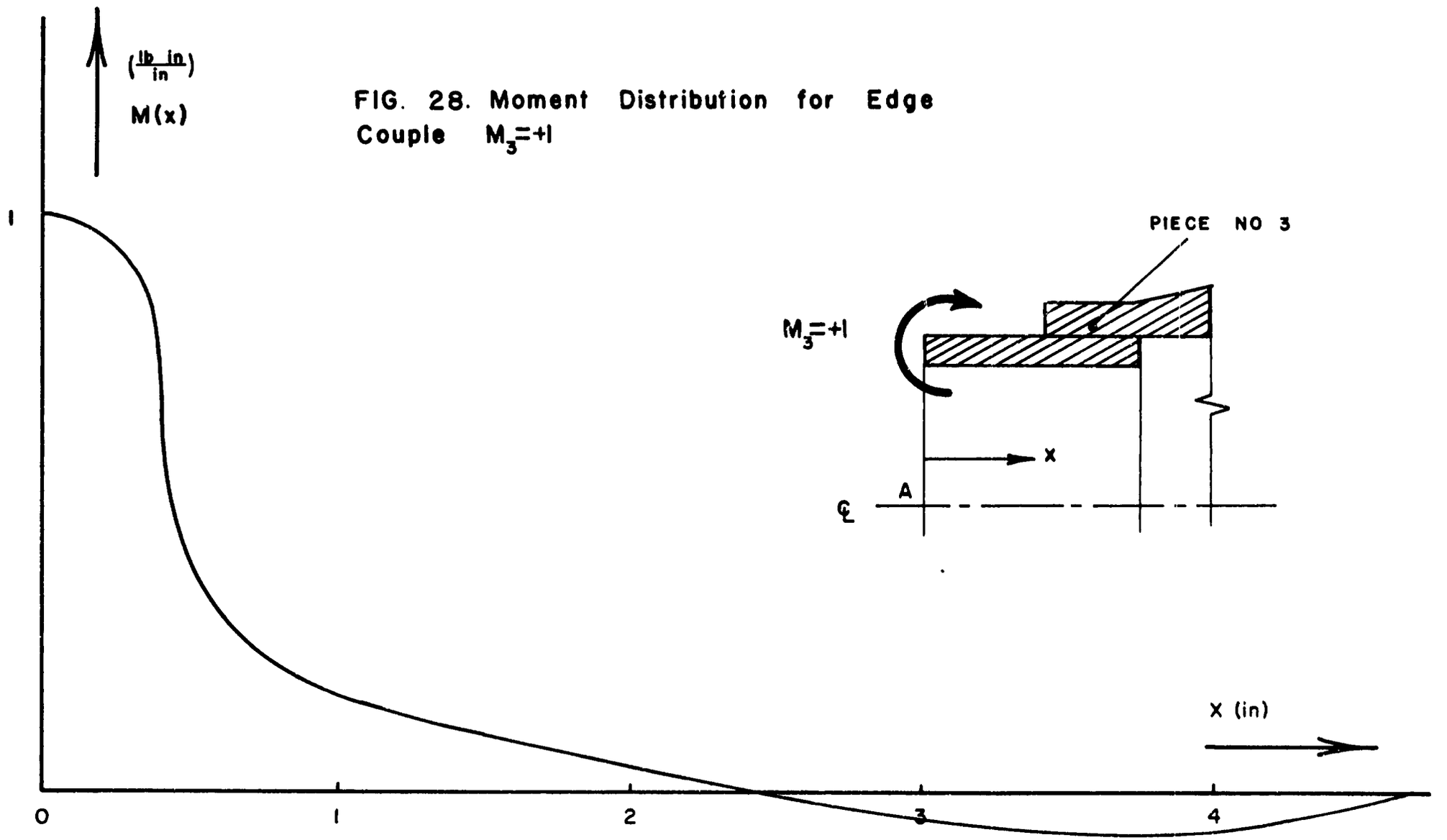

FIG. 28. Moment Distribution for Edge Couple $M_3=+1$

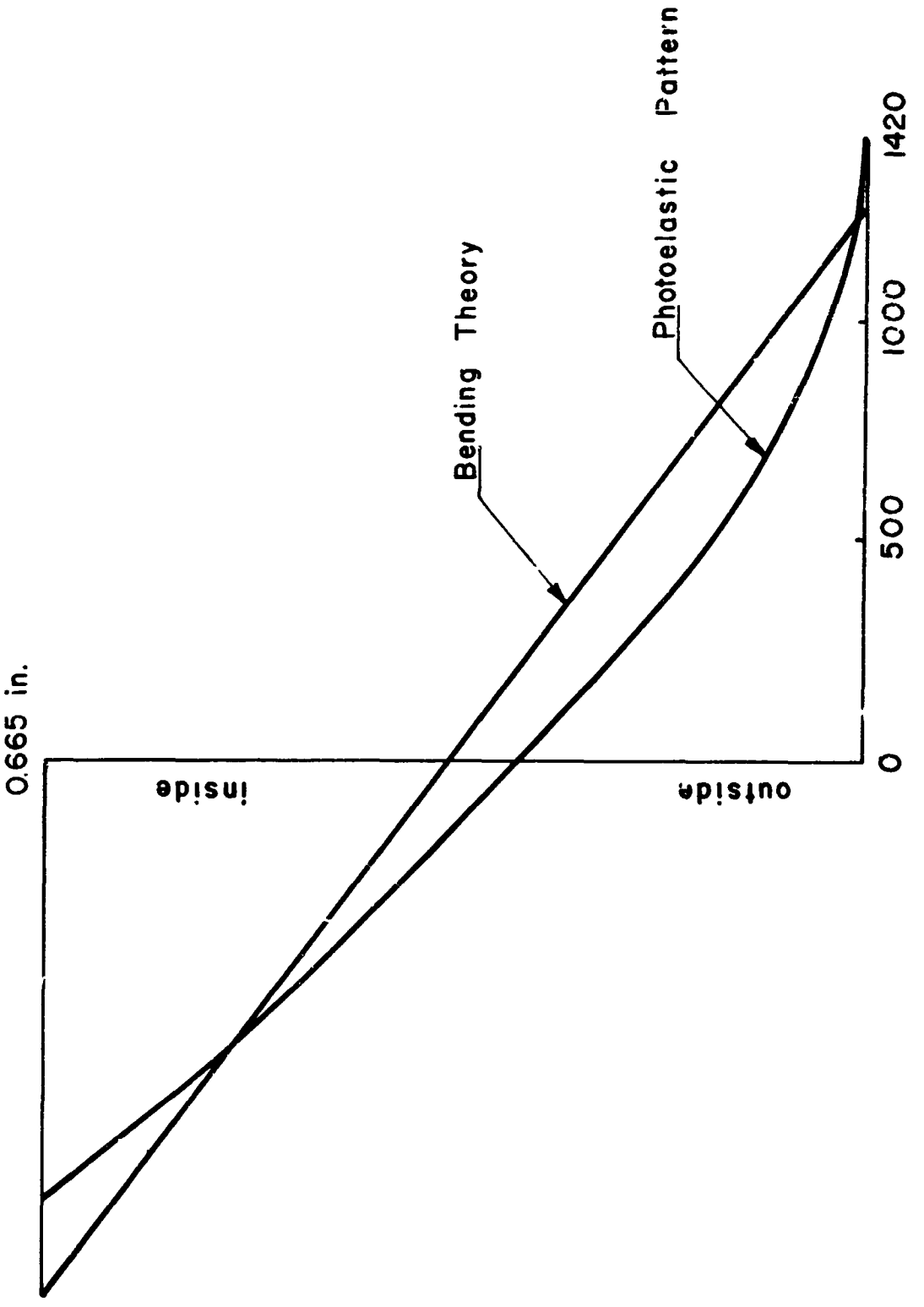

Figure 29. Stress Distribution at the Most Critical Section of the Joint Between Knuckle and Cylindrical Wall Under Pur[illegible] Bending

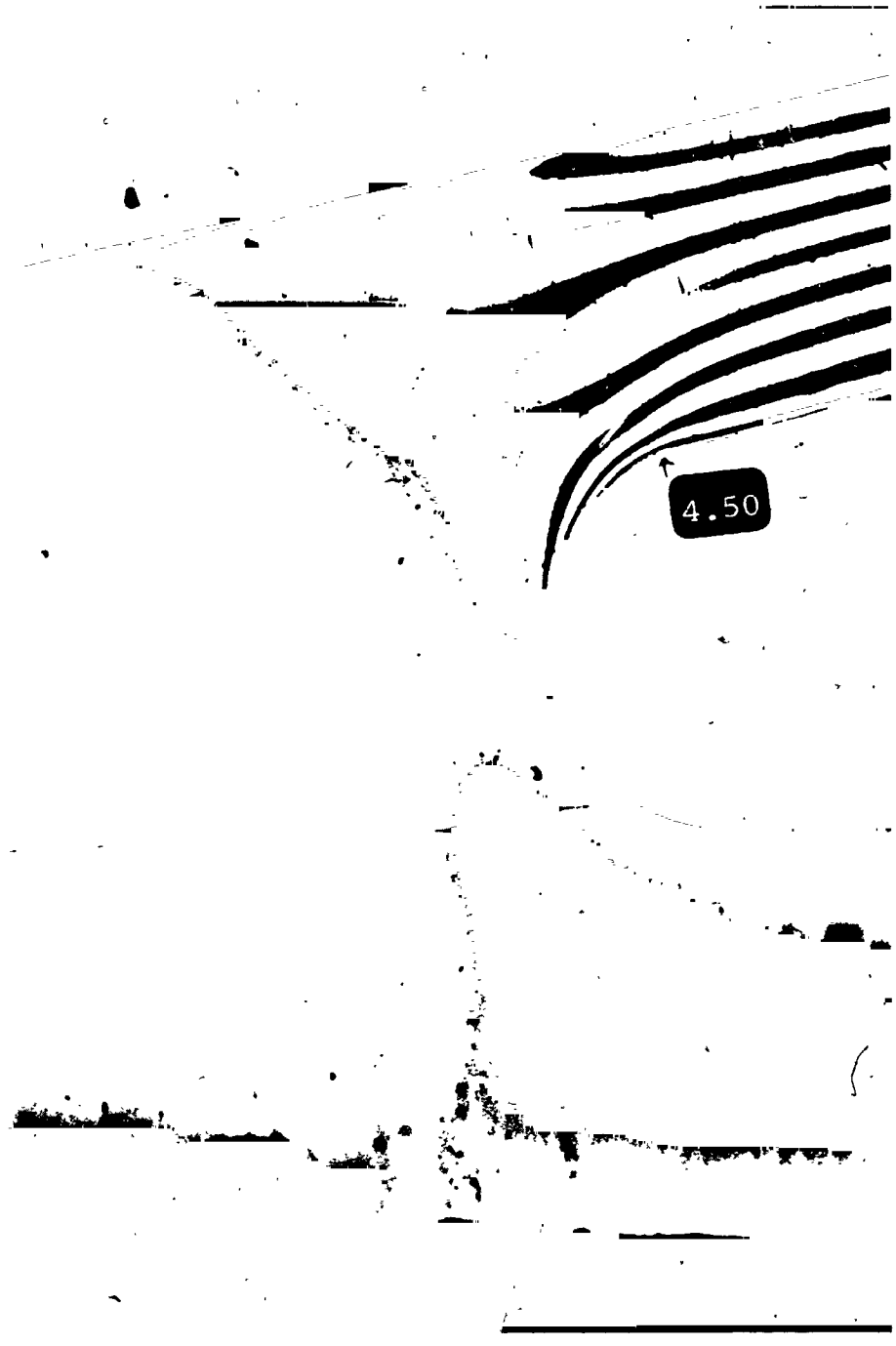

FIGURE 30. STRESS CONCENTRATION FACTOR FOR M = 29.70 lb/in, P = 0.

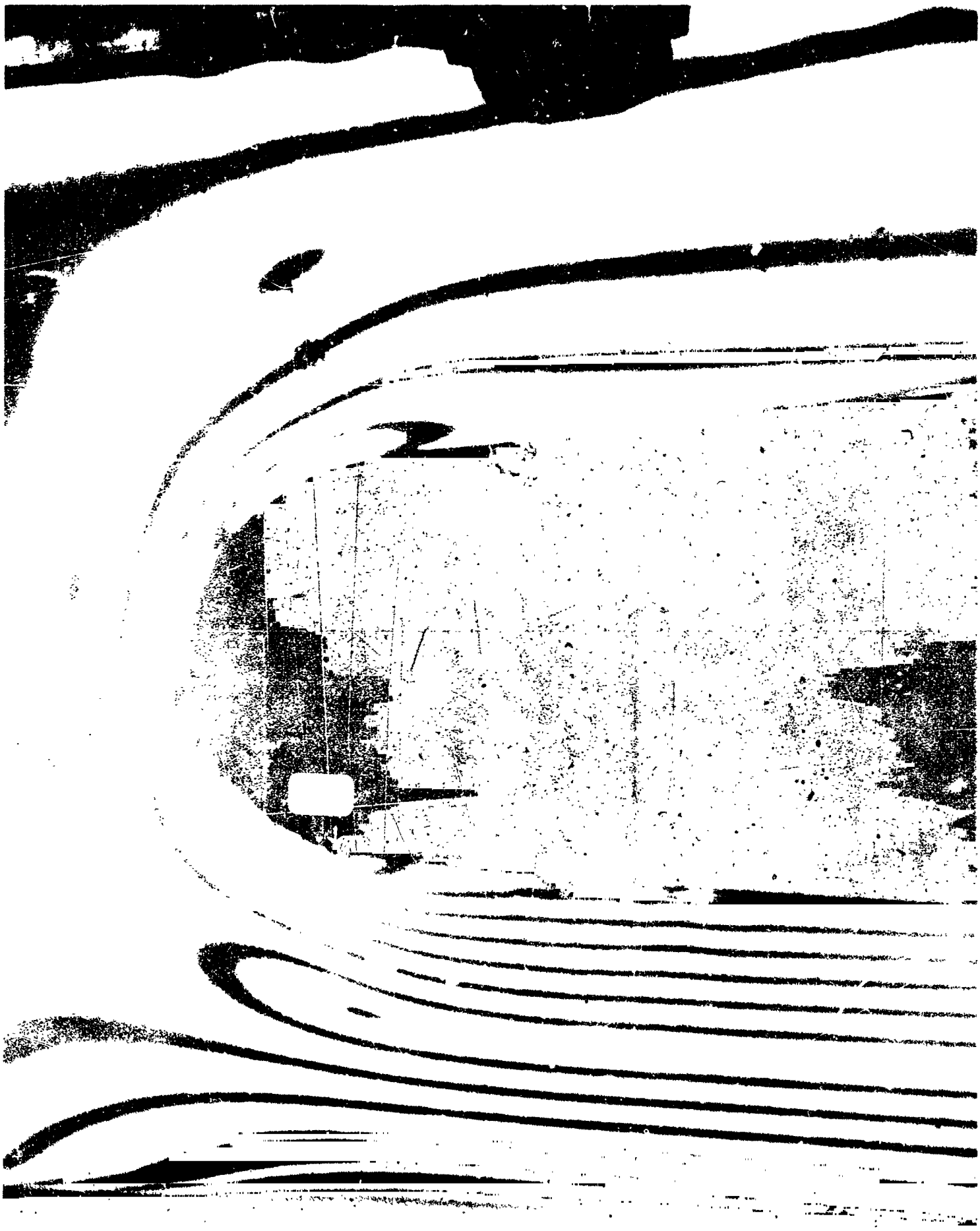

FIGURE 31. STRESS CONCENTRATION FACTOR FOR M = 44 lb/in, P = 9.9 lb.

FIGURE 32. STRESS CONCENTRATION FACTOR M = 33.3 lb/in, P = 12.5 lb.

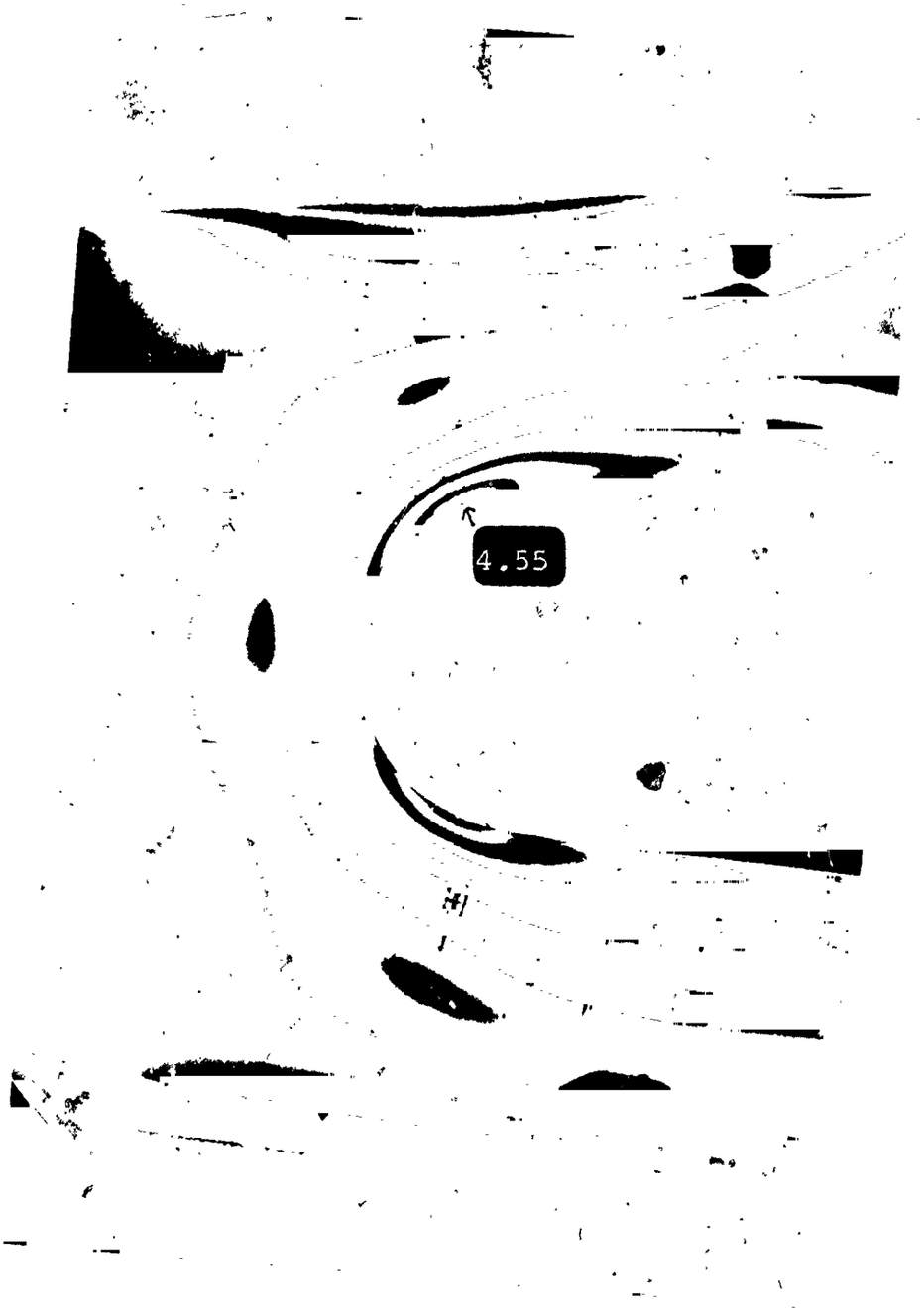

FIGURE 33. STRESS CONCENTRATION FACTOR M = 22 lb/in, P = 13.4.

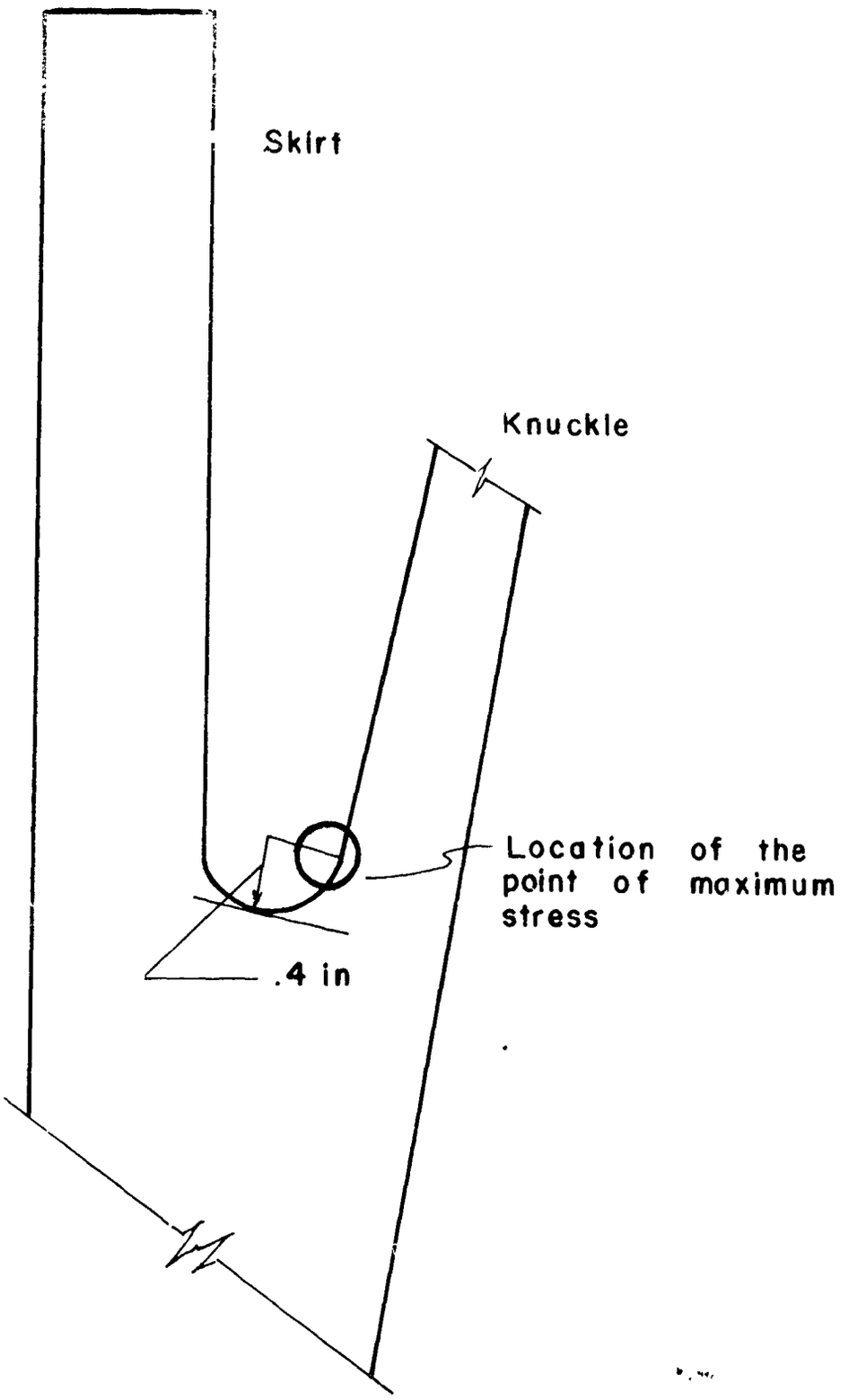

Figure 34. Location Of The Point Of Maximum Stress In The Intersection Of Knuckle, Skirt And Cylinder

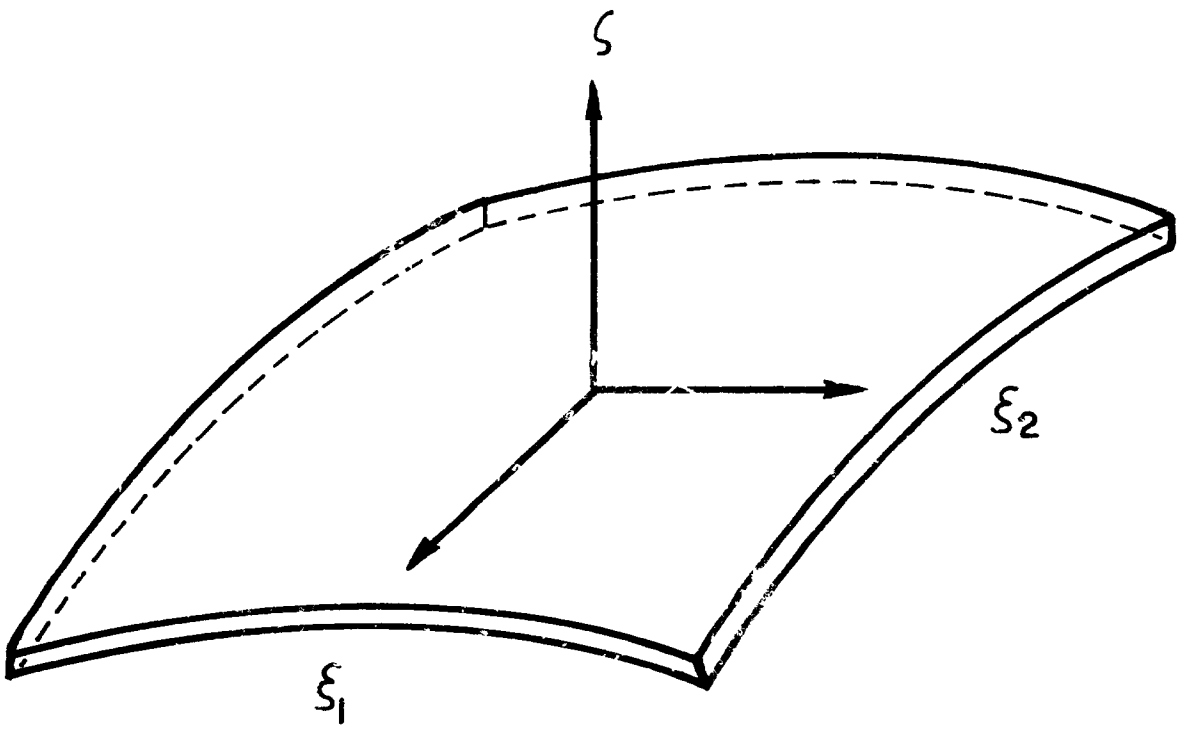

Figure 35. System Of Coordinates Corresponding To The Shell

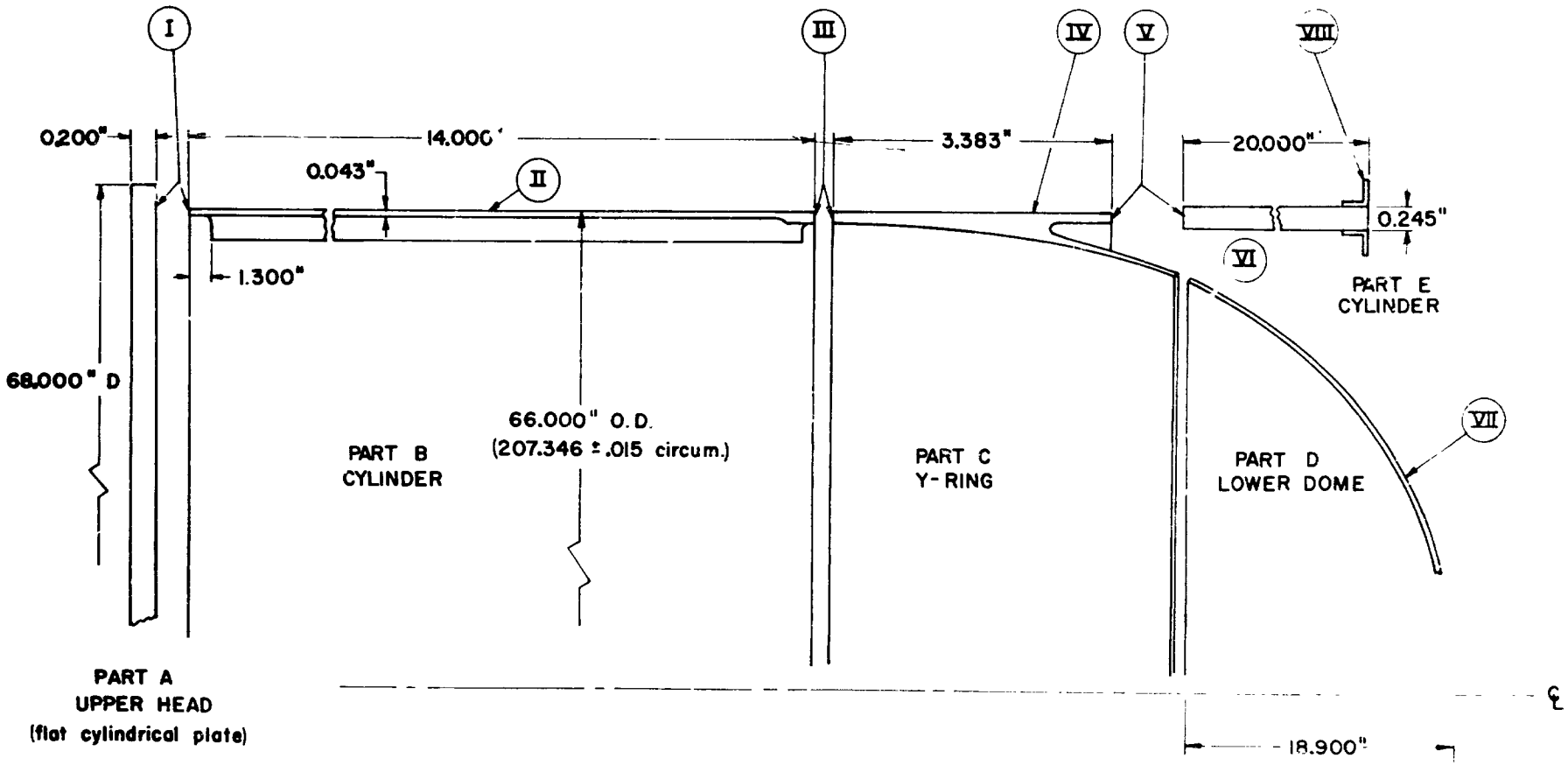

FIGURE 36
TANK

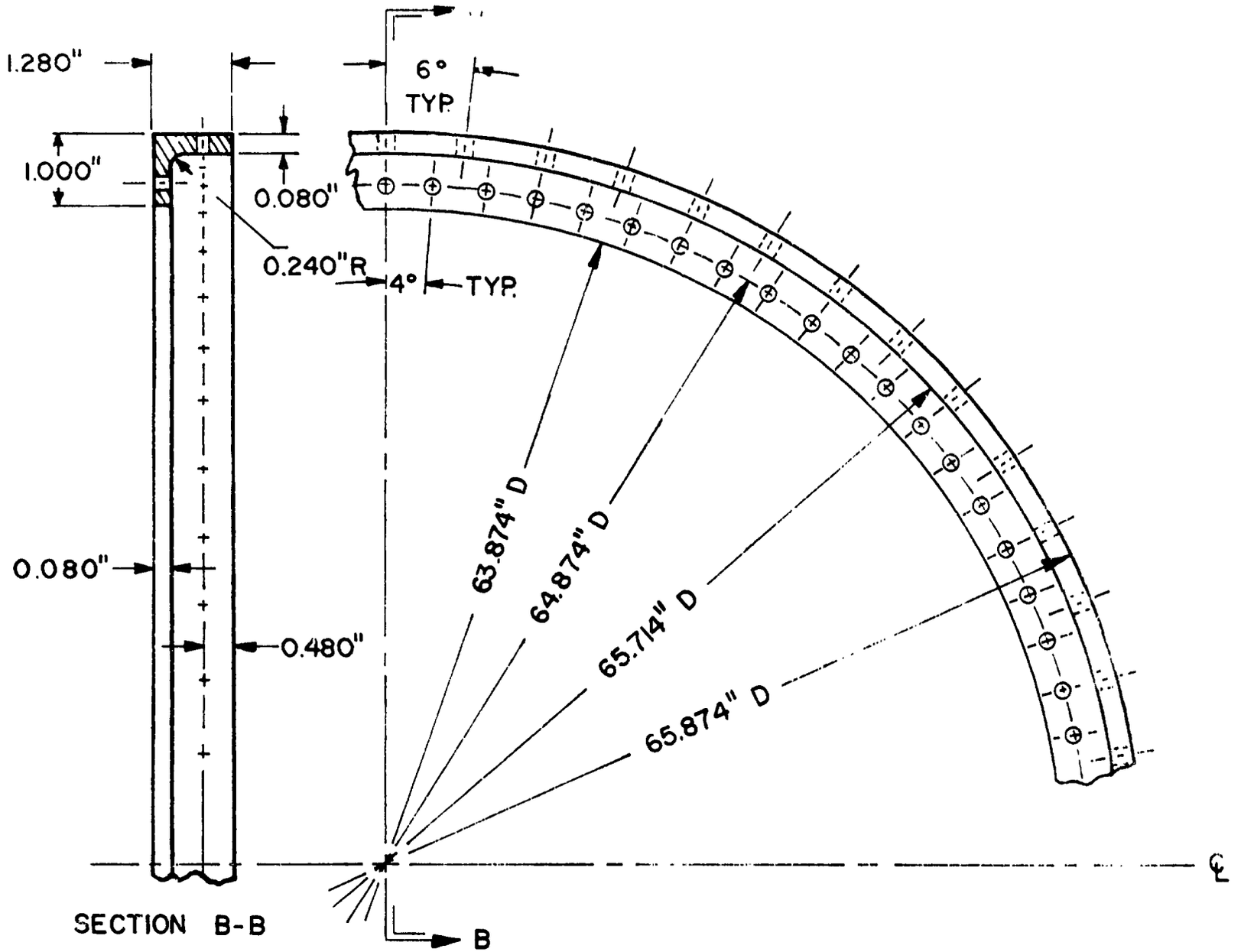

FIGURE 37
DETAIL I

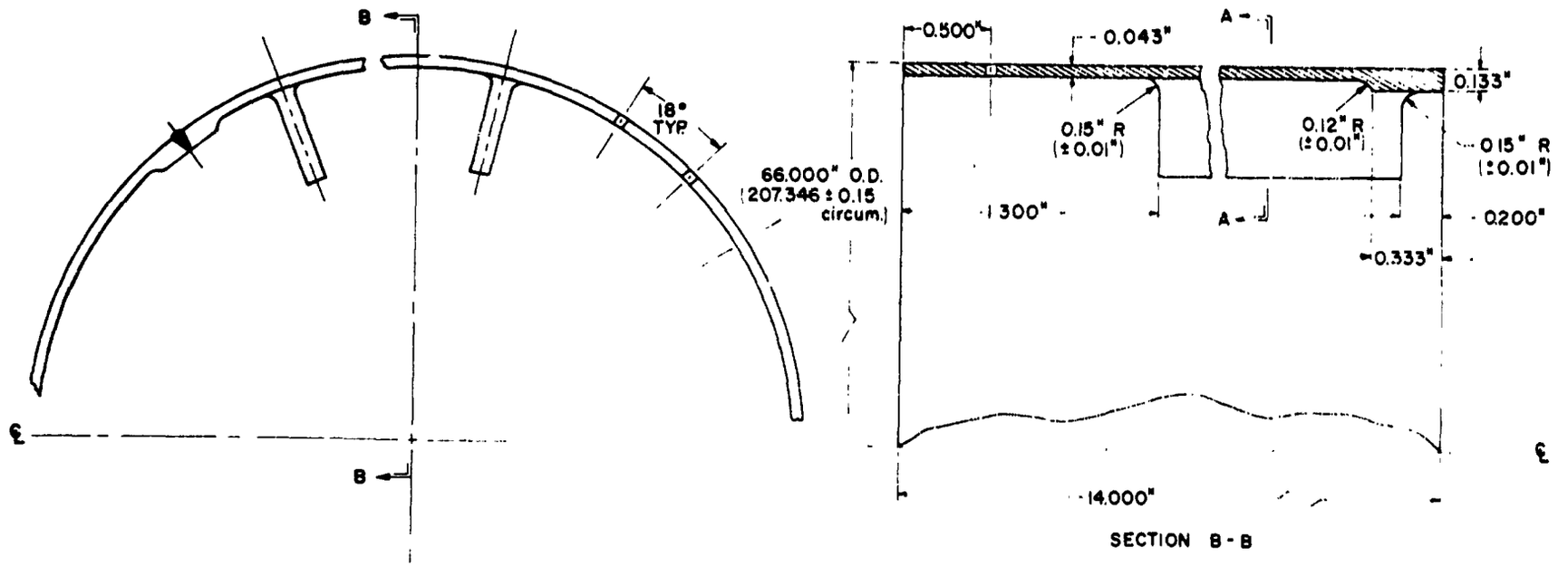

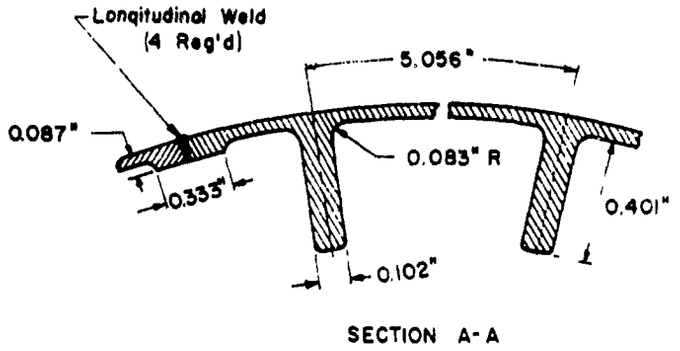

FIGURE 38
DETAIL II

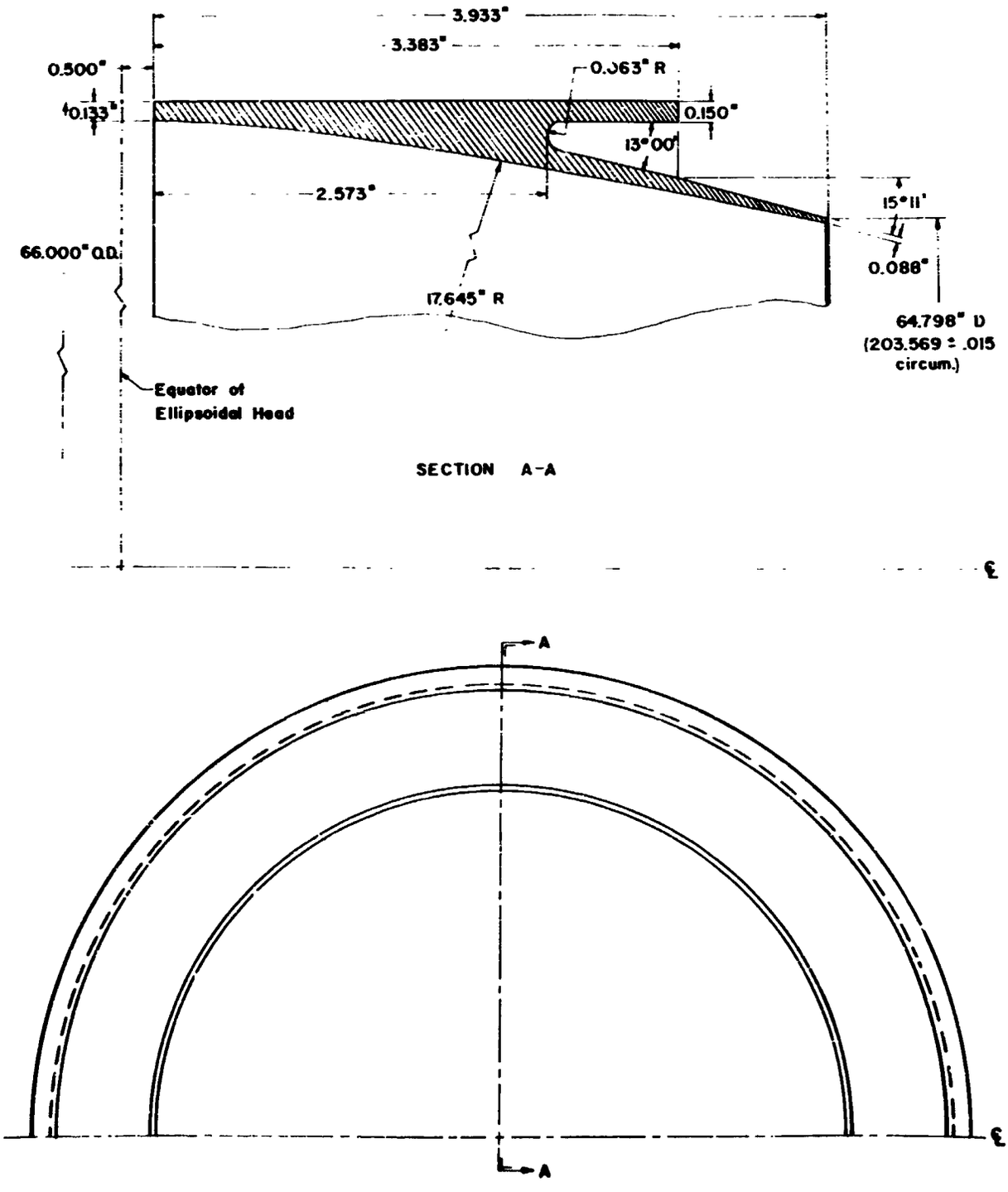

FIGURE 39
DETAIL IV

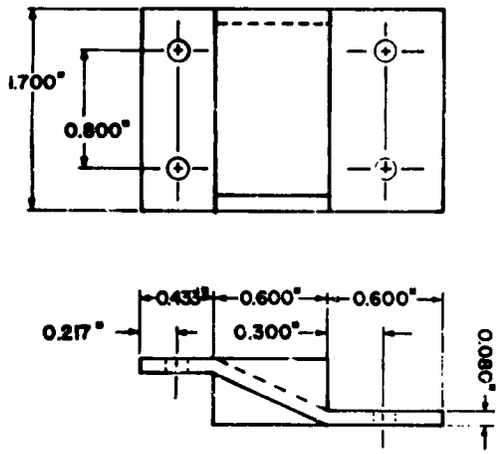

CLAMP 2

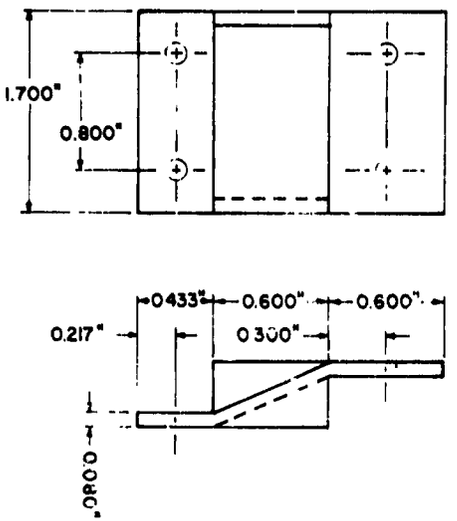

CLAMP 1

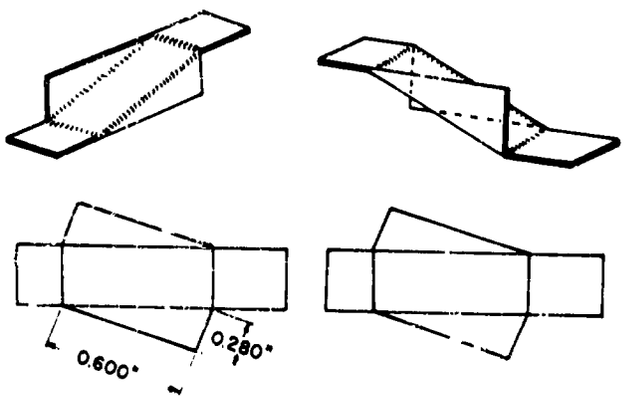

CLAMP 1 CLAMP 2

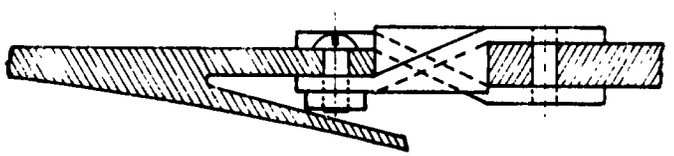

FIGURE 40
DETAIL V

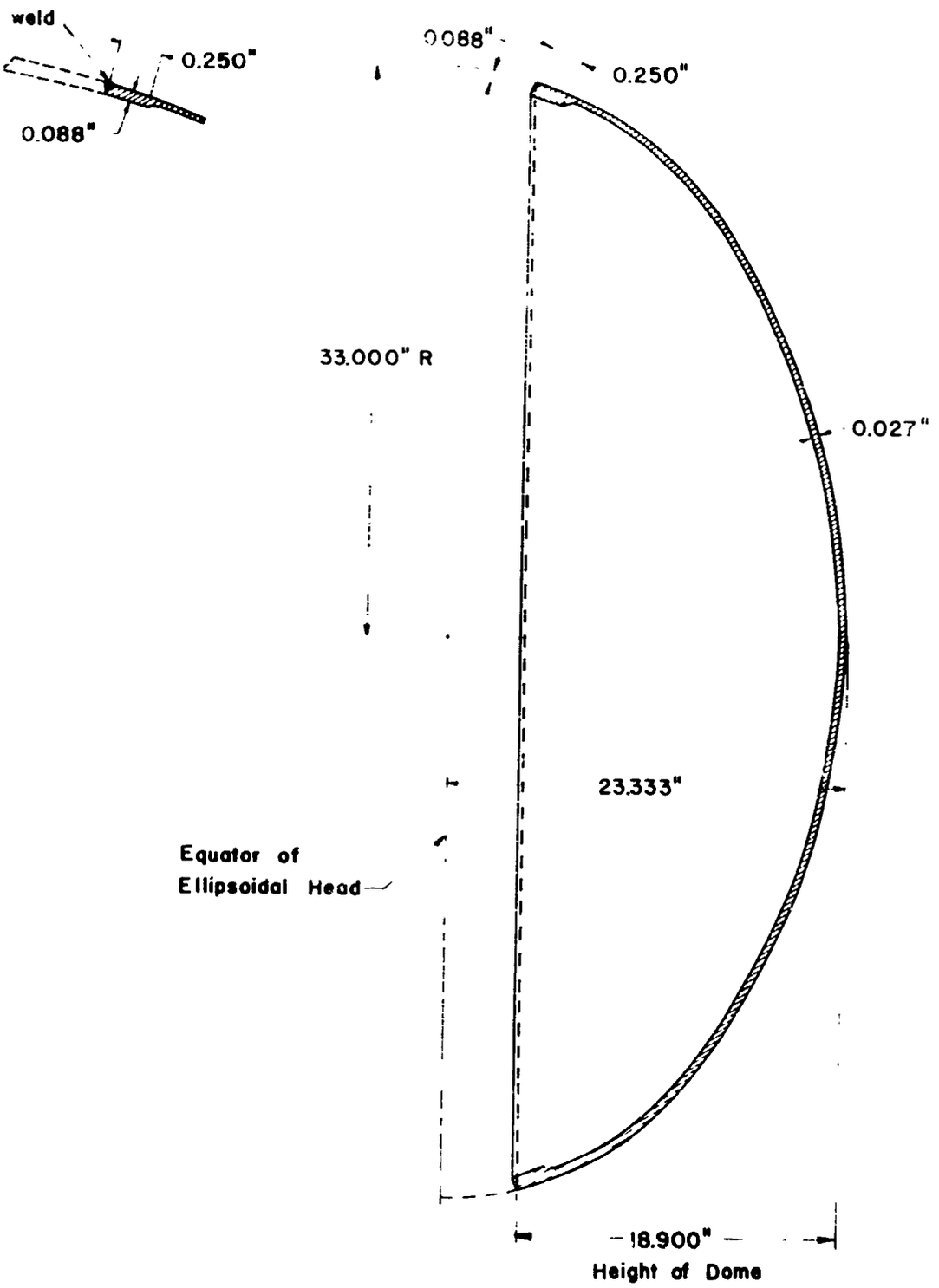

FIGURE 4!
DETAIL XII

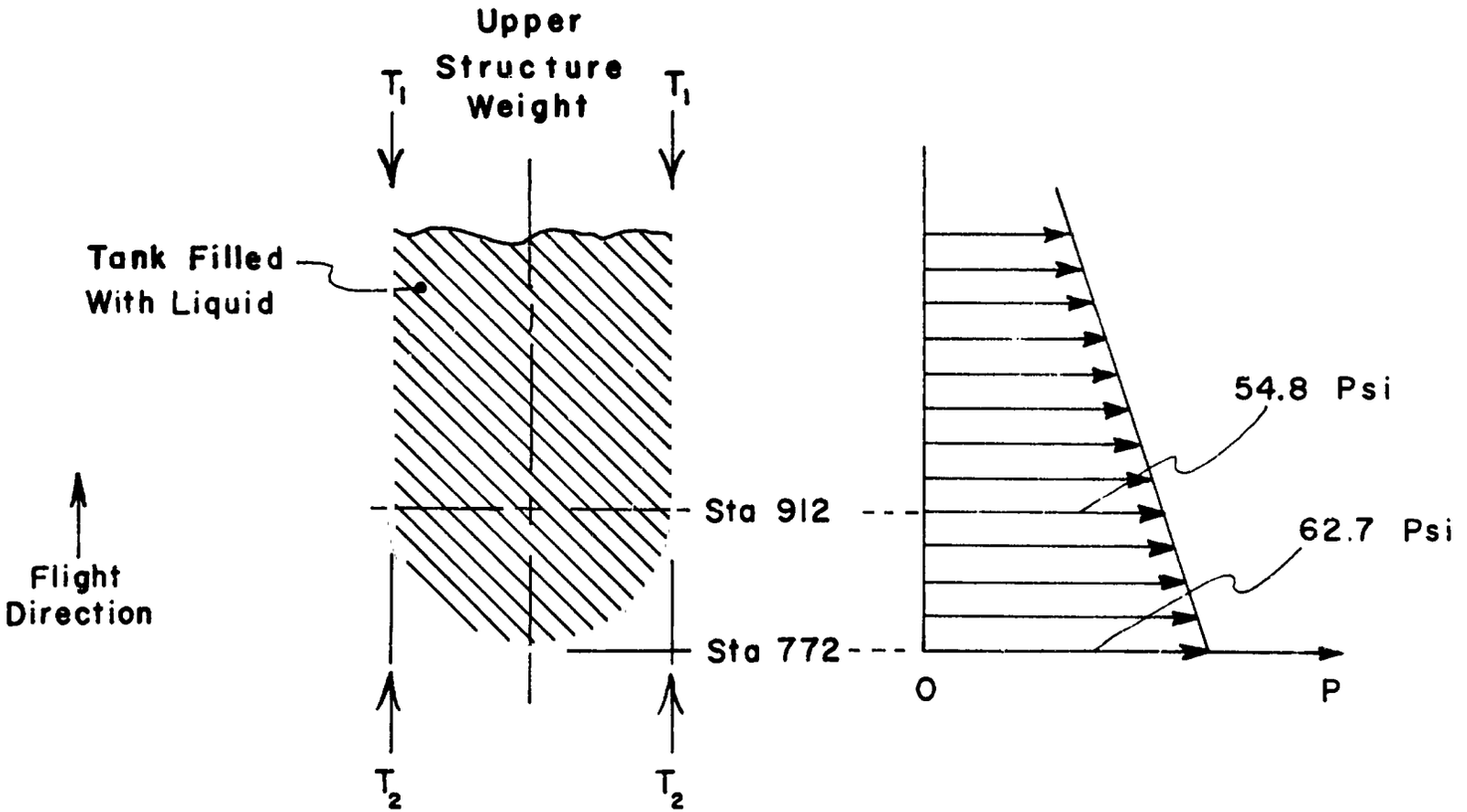

Figure 42. The Considered "Rebound" Loading

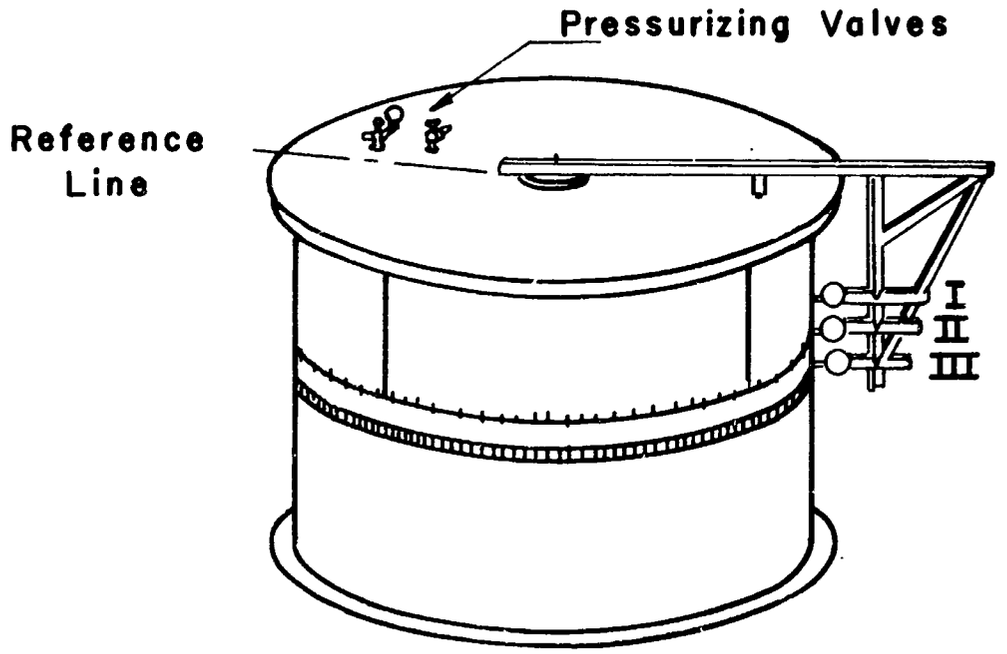

(a)

The Reference Line Indicates the Position of Reading I; Successive Readings Were Made at 22 1/2° Intervals Counter-Clockwise from the Reference Line.

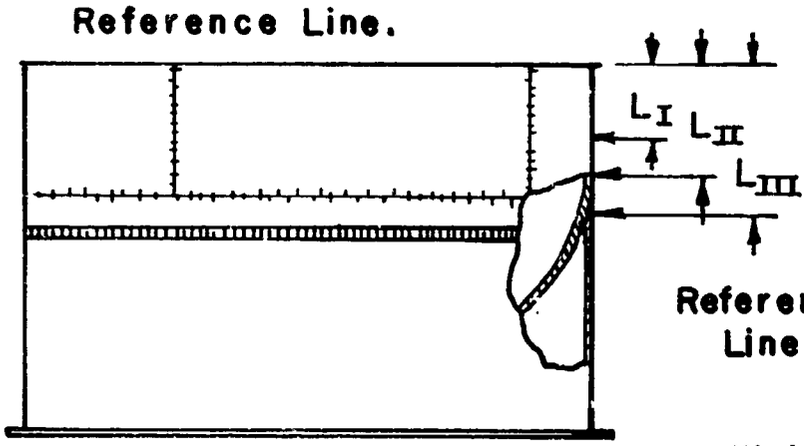

(b)

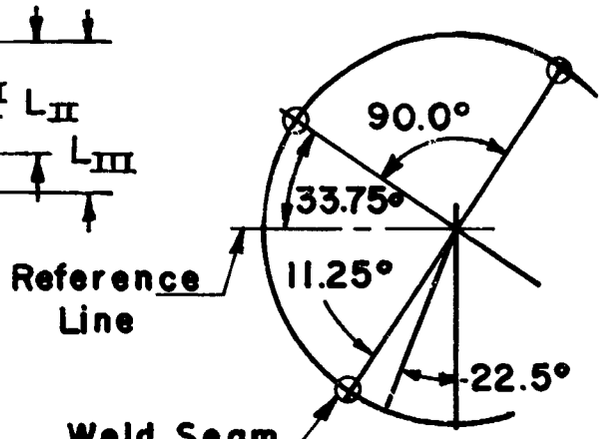

(c)

L_I = 8.70 Inches

L_{II} = 12.51 Inches

L_{III} = 15.16 Inches

Figure 43. Out-of-Roundness Test:
(a) Basic Set-Up;
(b) Side View of Tank;
(c) Partial Top View of Tank

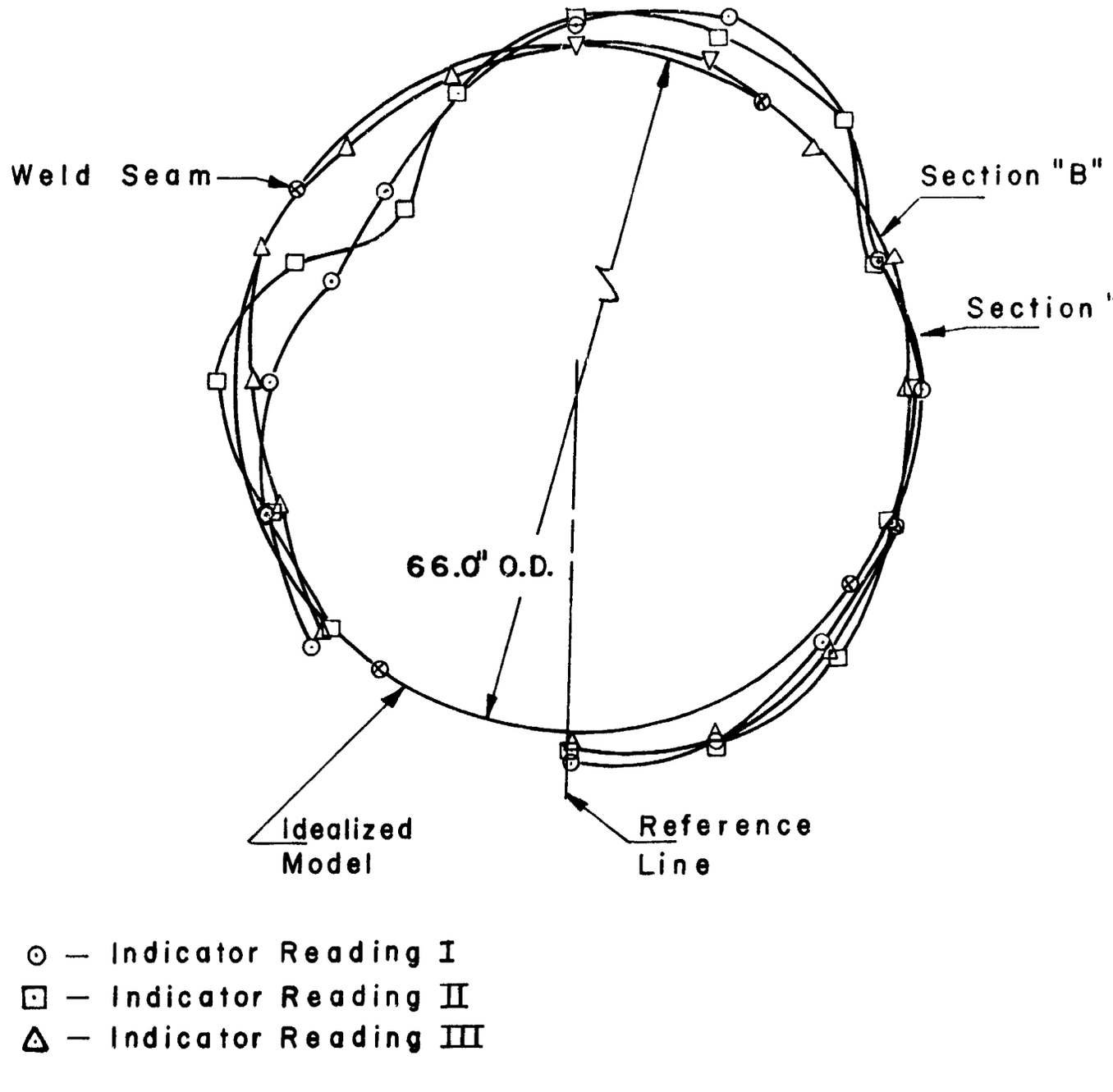

Figure 44. Tank Out-of-Roundness Curves

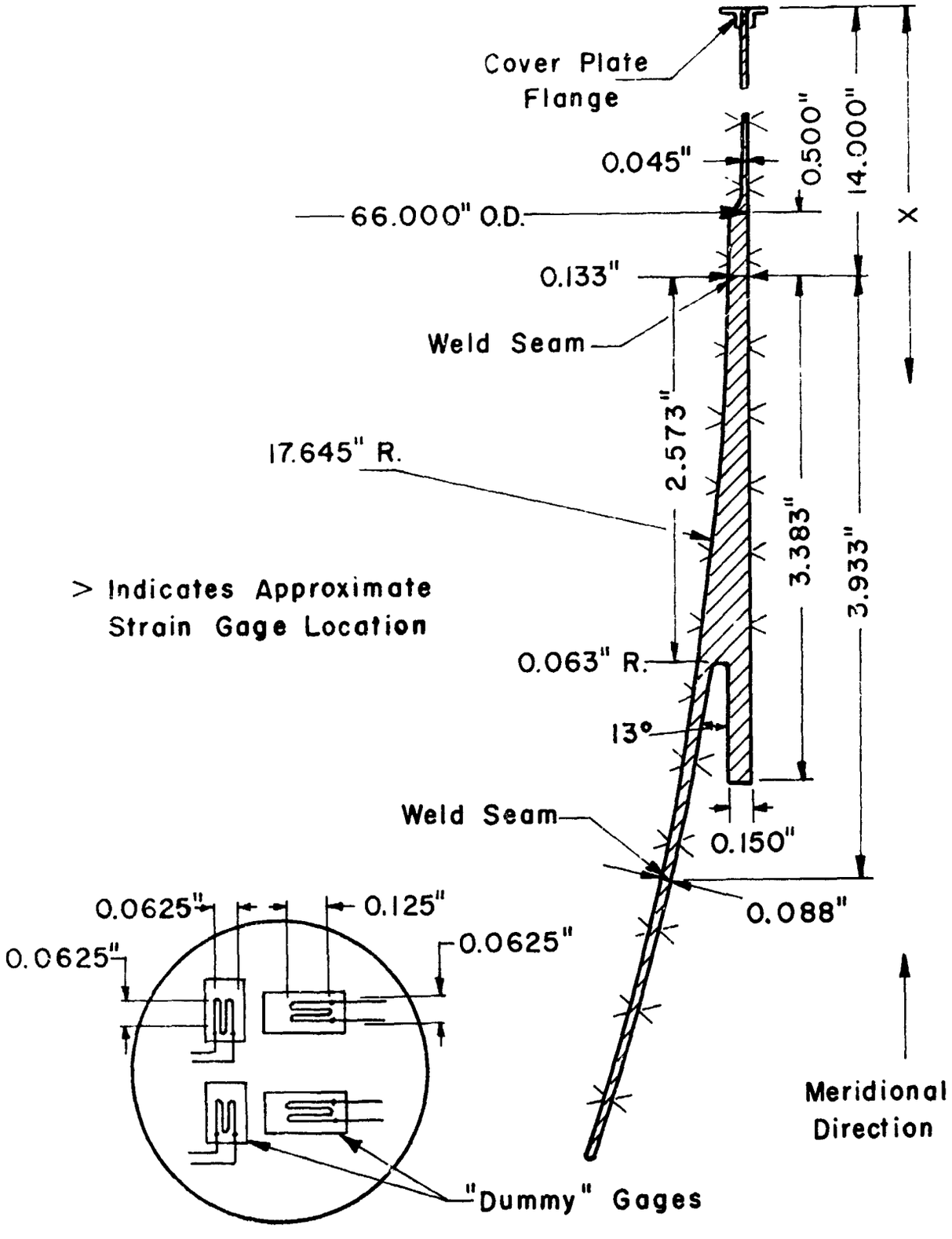

Figure 45. Dimensioned Sectional View of Y-Ring Showing Strain Gage Spacing

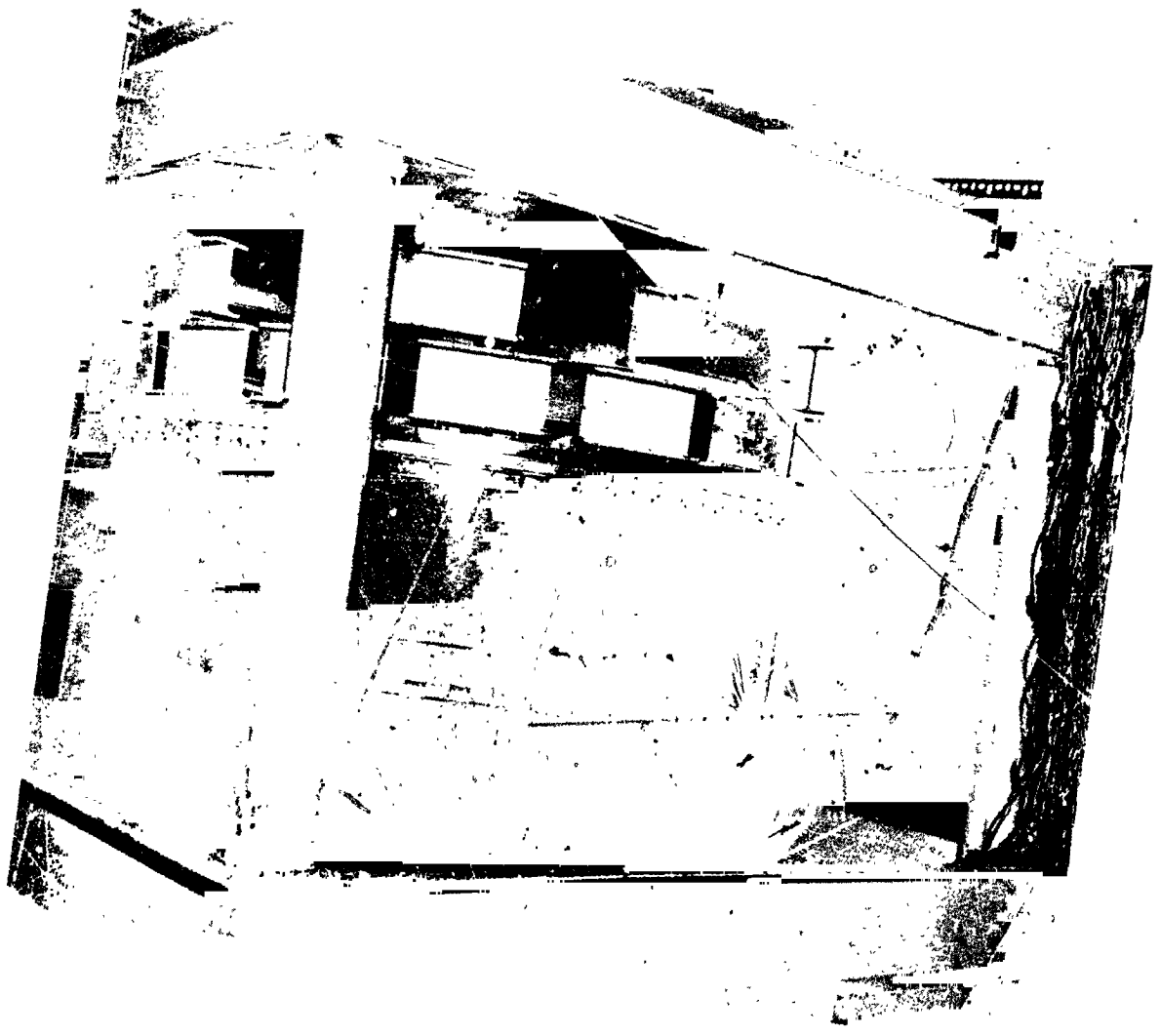

FIGURE 46. LOADING FRAME USED FOR TESTING THE TANK.

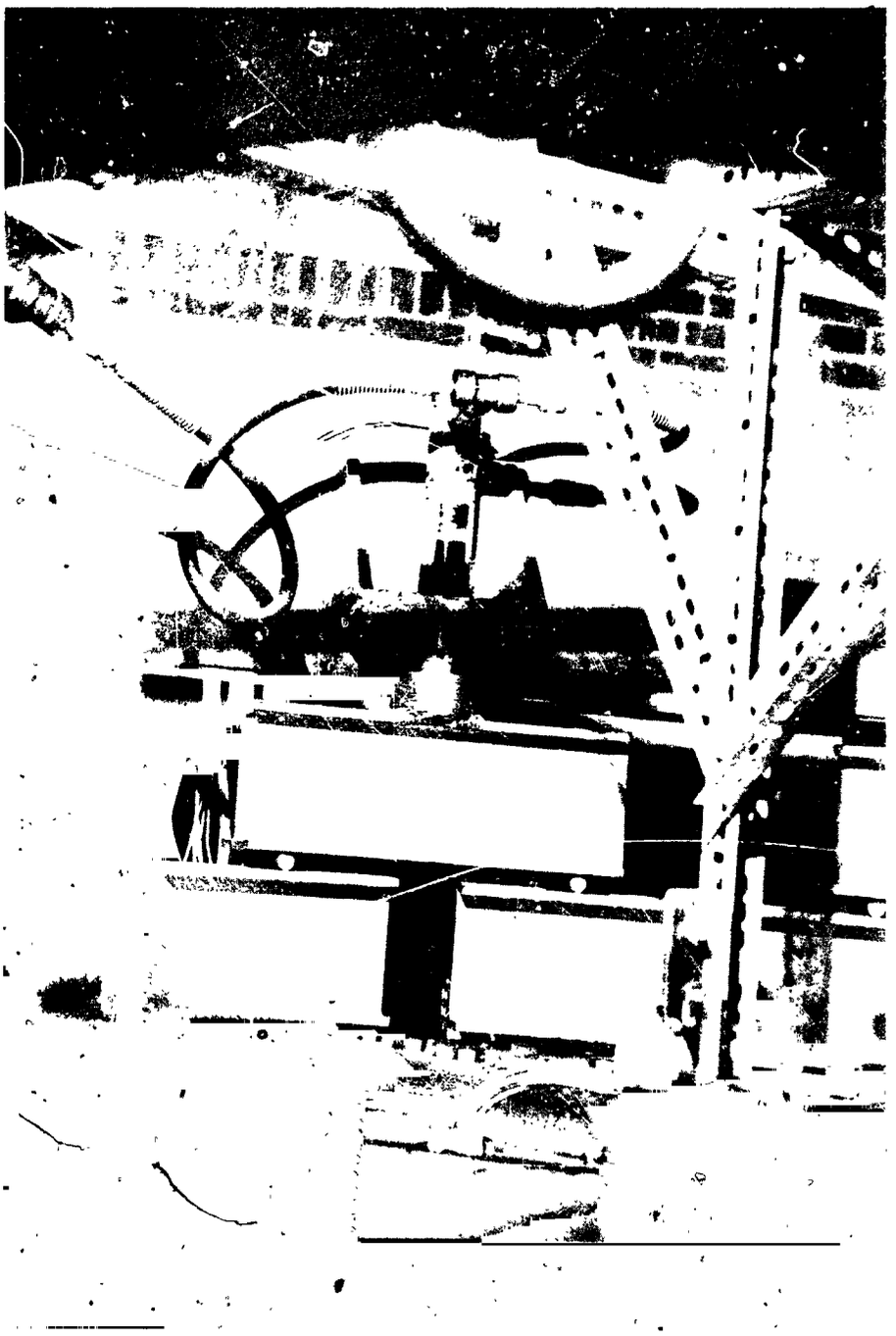

FIGURE 45. HYDRAULIC JACK AND SYSTEM USED TO DISTRIBUTE THE LOAD.

FIGURE 48. STRAIN GAGES APPLIED TO THE BULKHEAD.

FIGURE 49. STRAIN GAGES APPLIED TO THE INSIDE FACE OF THE "Y-RING."

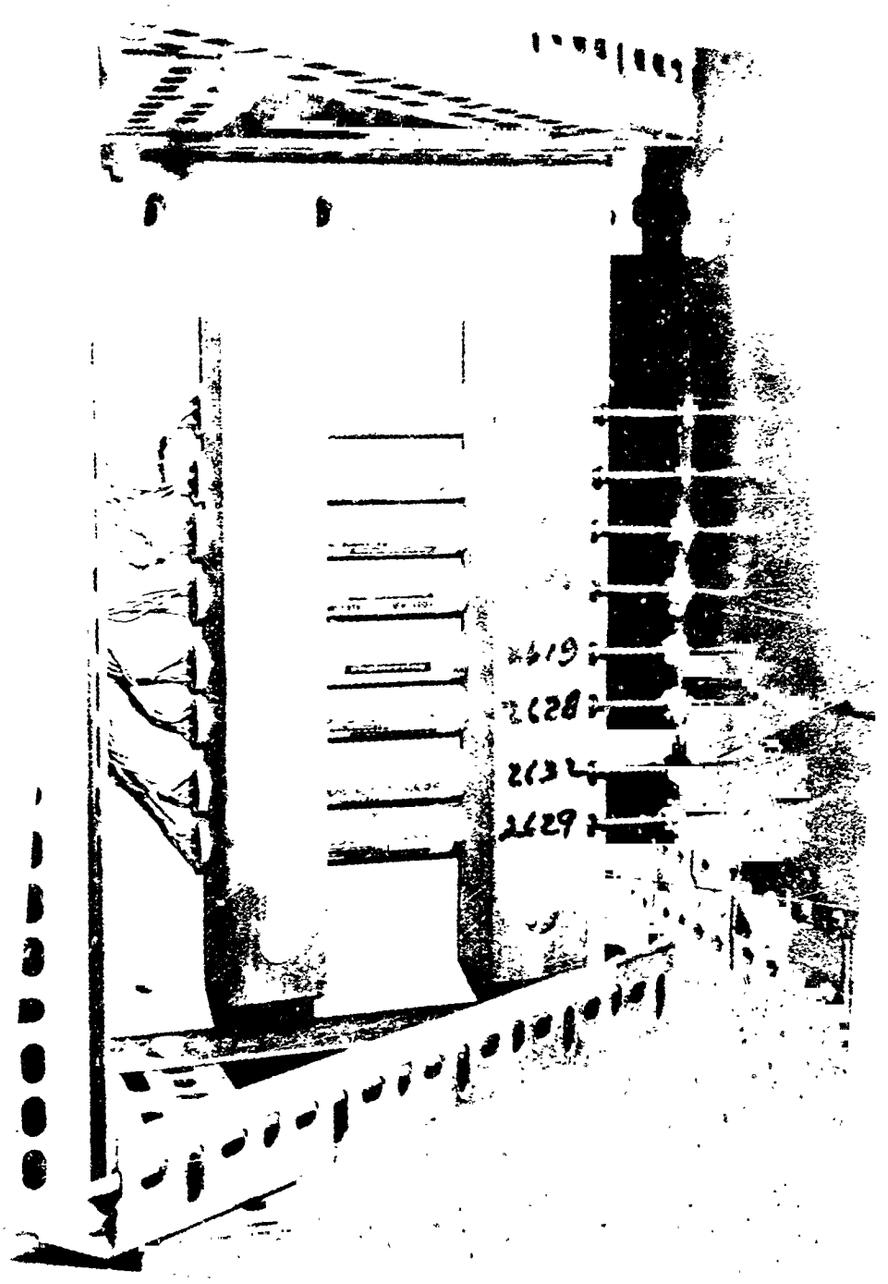

FIGURE 50. DIFFERENTIAL TRANSFORMER INSTALLATION

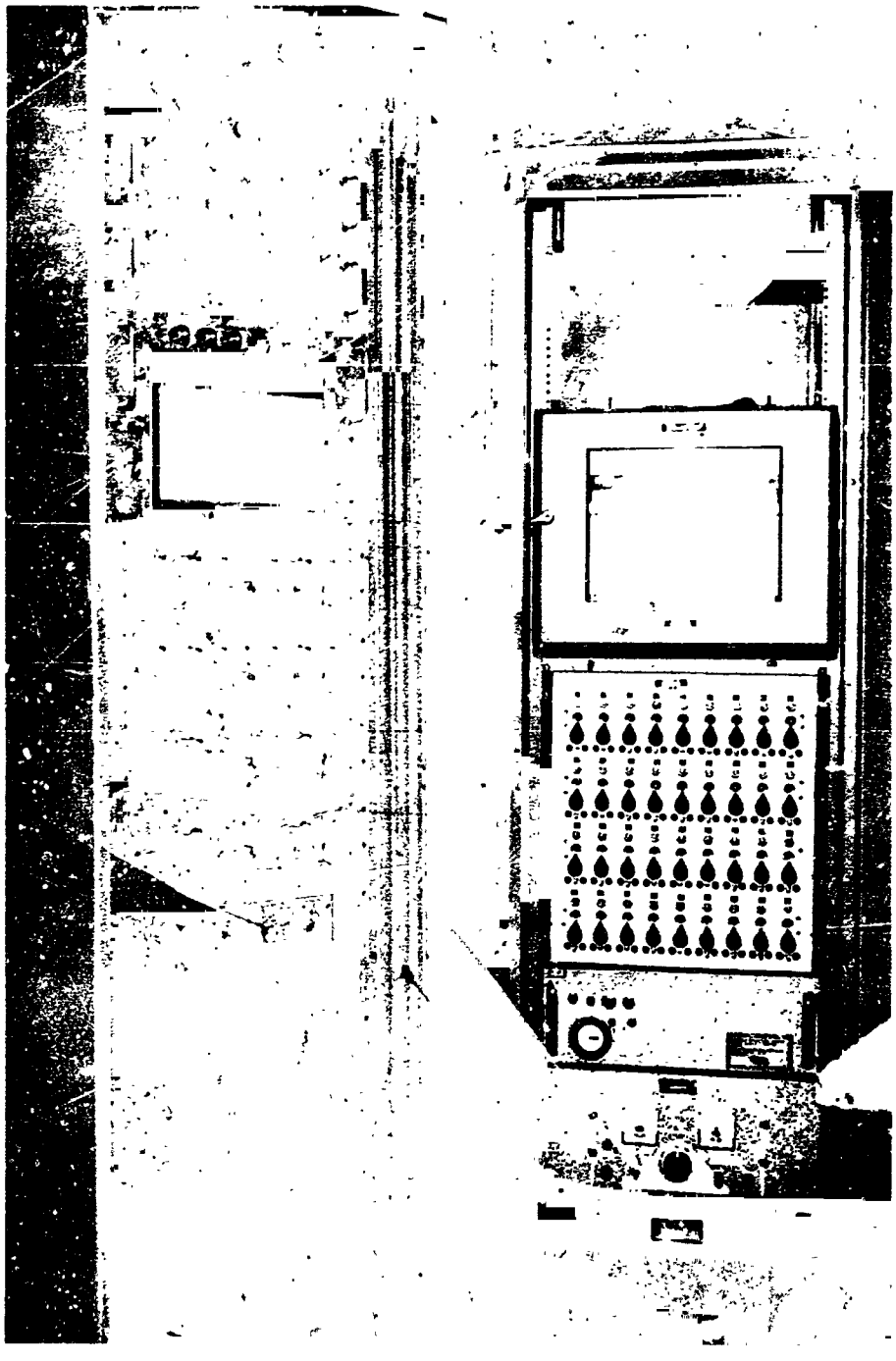

FIGURE 51. INSTRUMENTS USED TO RECORD THE STRAIN-GAGES AND THE DIFFERENTIAL TRANSFORMERS READINGS

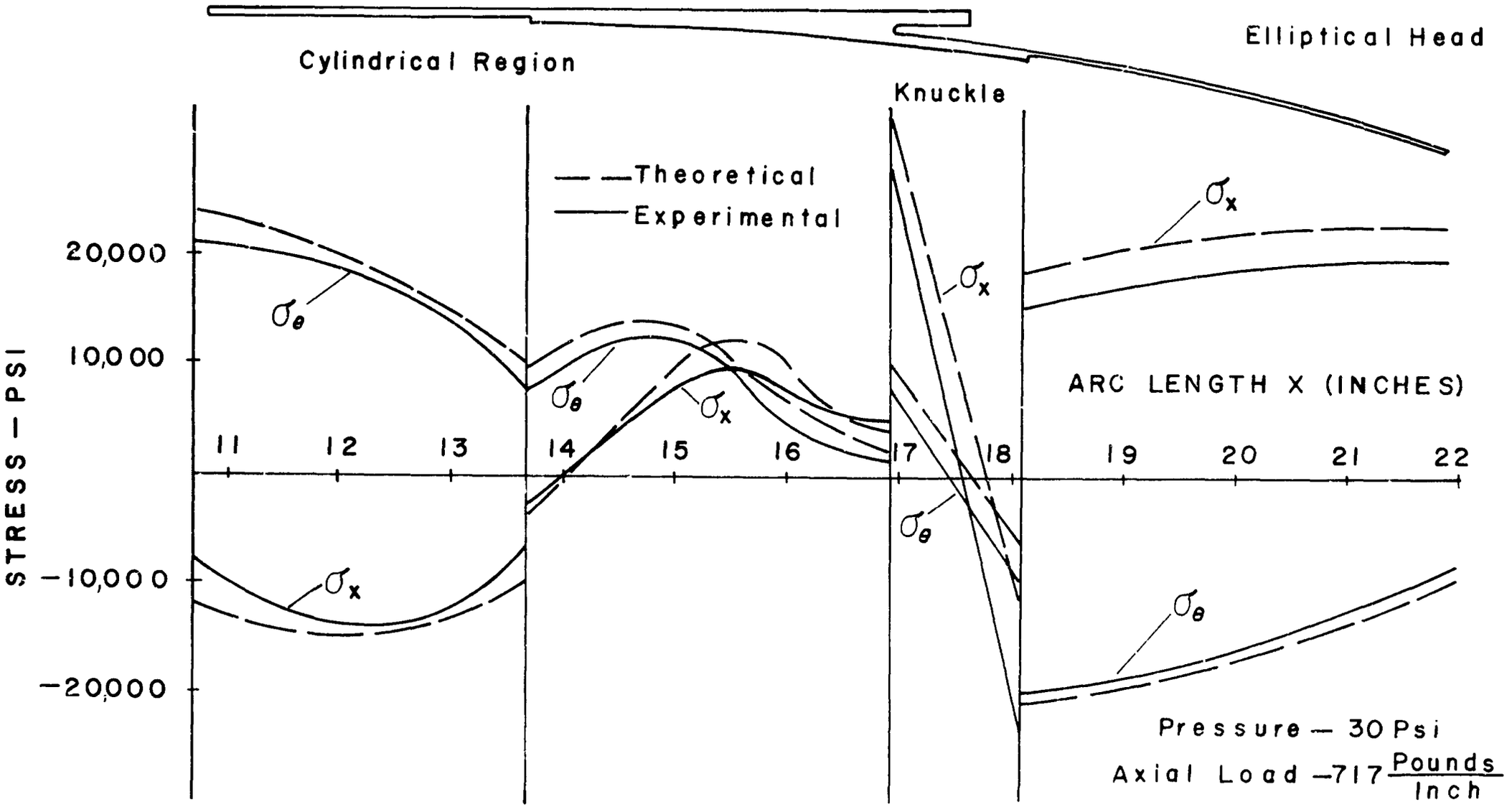

Figure 52. Interior Stress Distribution

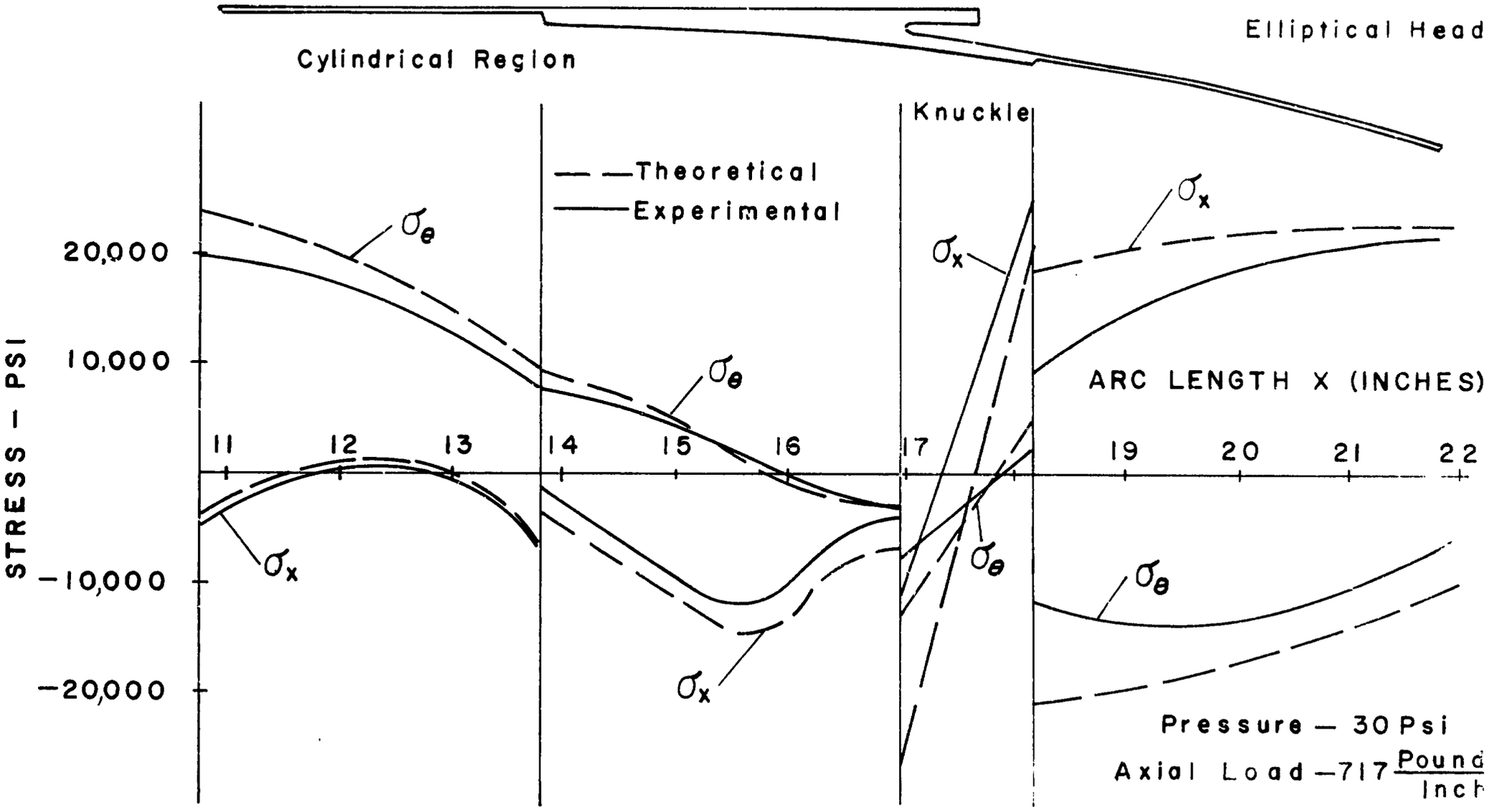

Figure 53. Exterior Stress Distribution

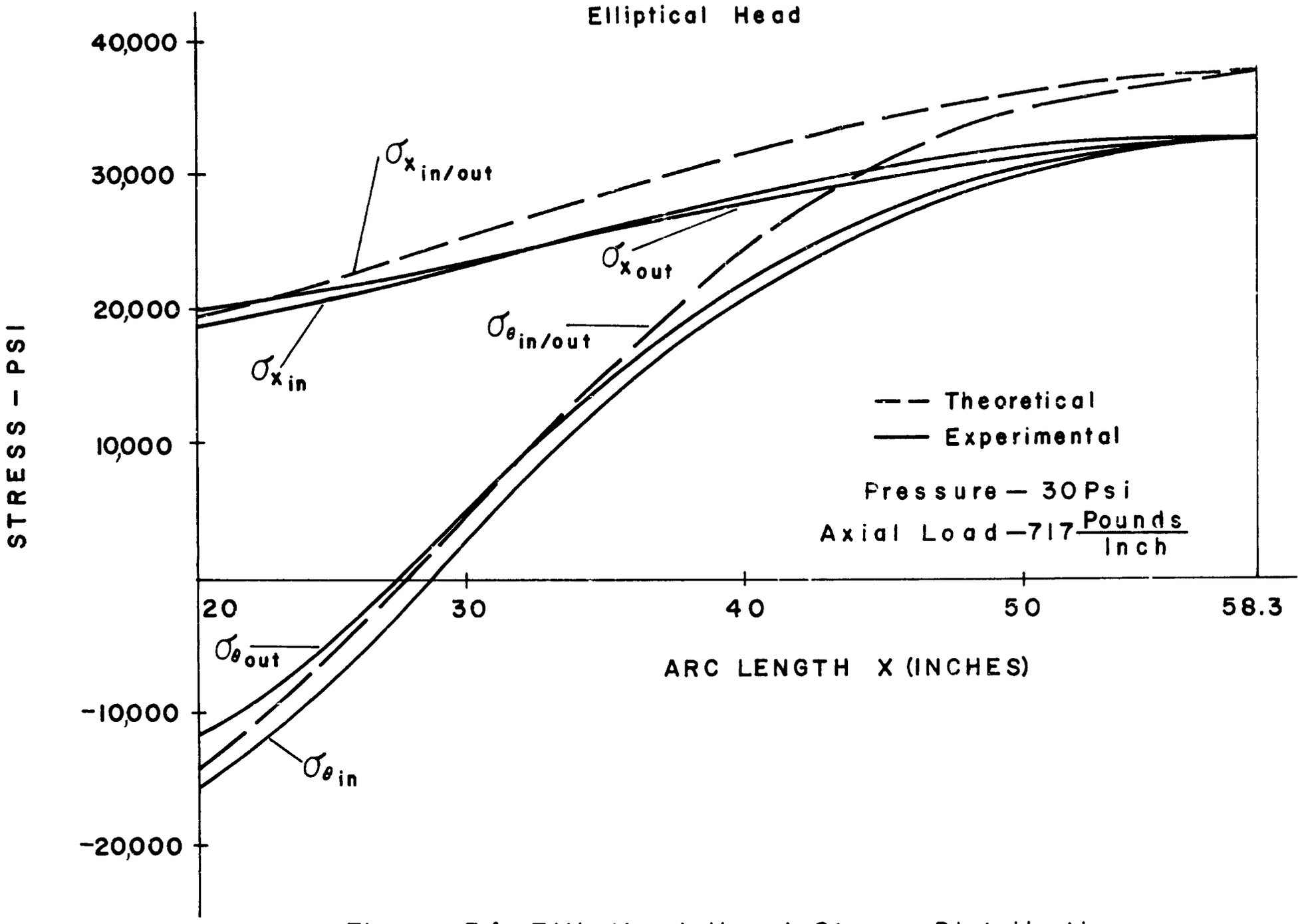

Figure 54. Elliptical Head Stress Distribution

LOADS

1 - 10 psi., 239 lb./in.

2 - 20 psi, 478 lb./in.

3 - 30 psi., 717 lb./in.

LEGEND

⊙ - X = 13.48 inches

⊡ - X = 17.03 "

△ - X = 33.9 "

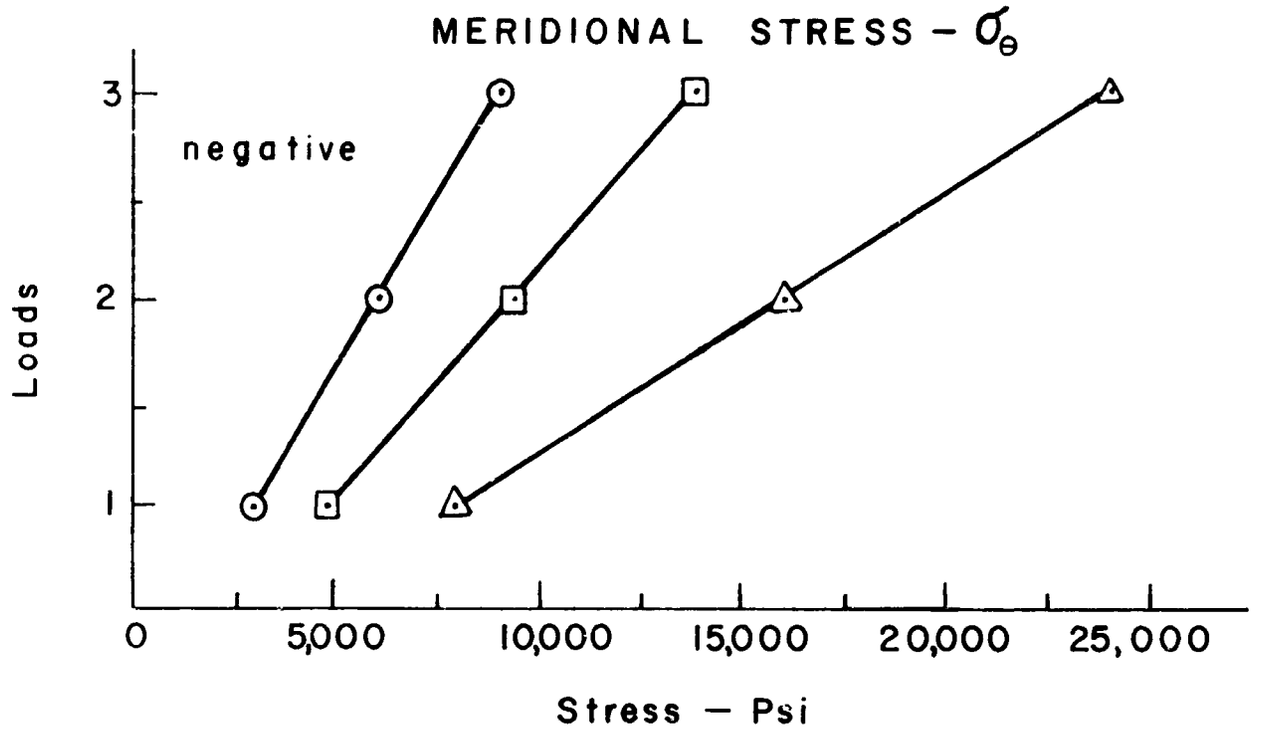

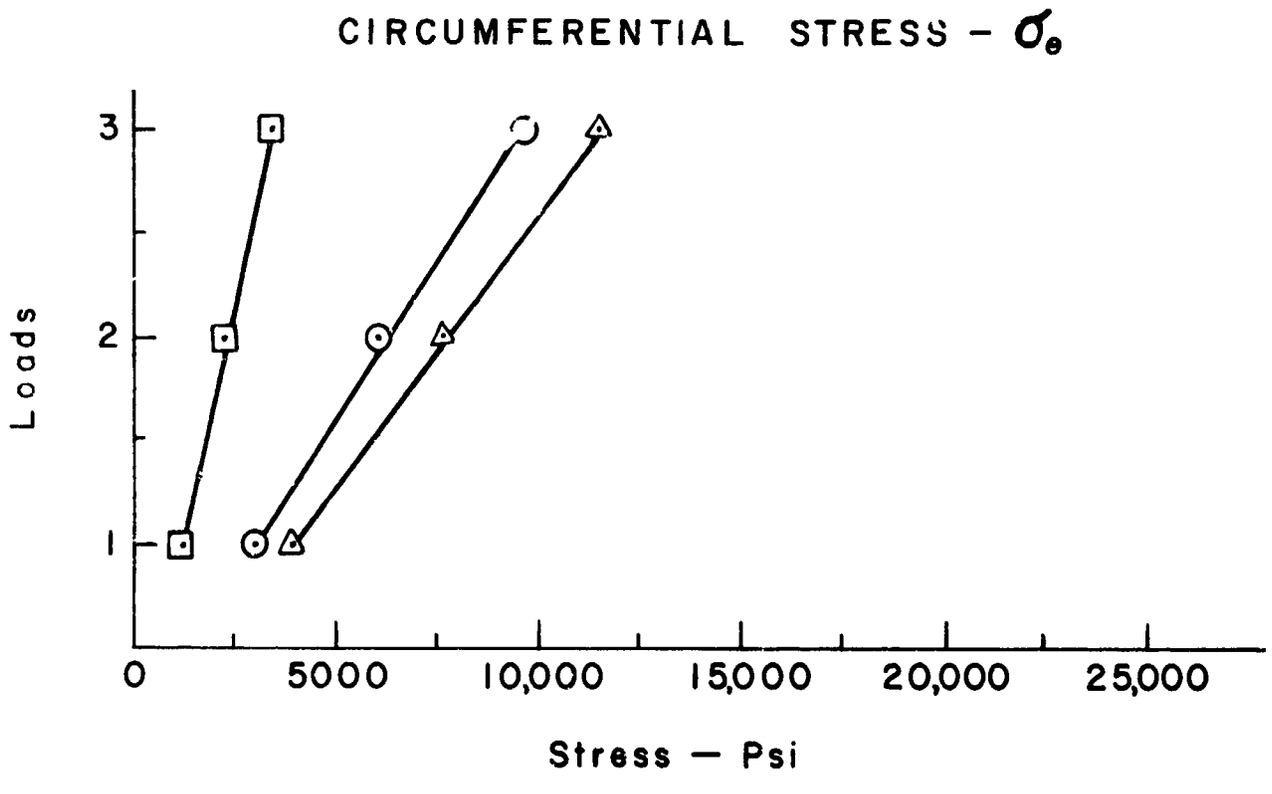

Figure 55. Linear Check of Stresses (Interior Points Only)

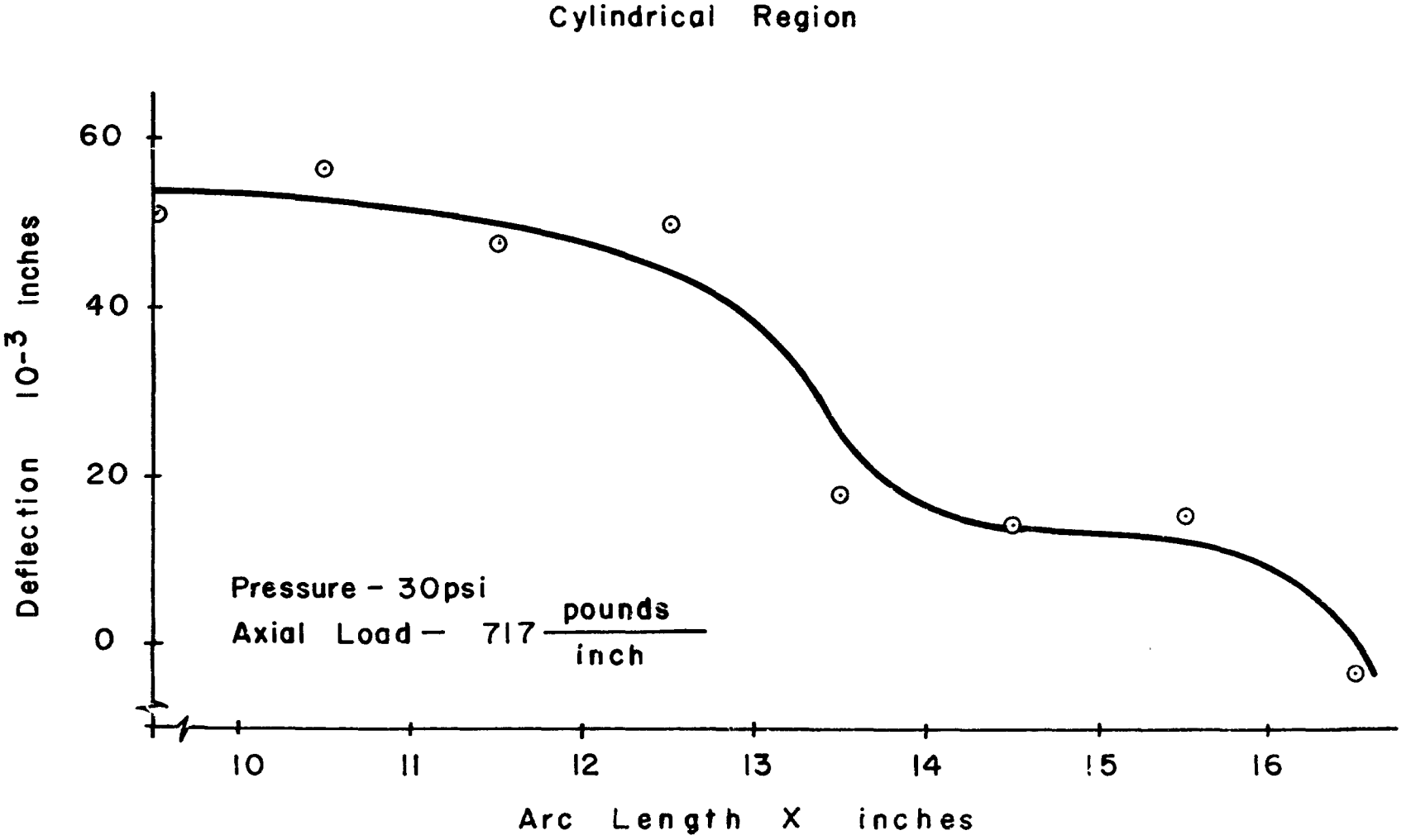

Figure 56. Deflection By LVDT Measurements

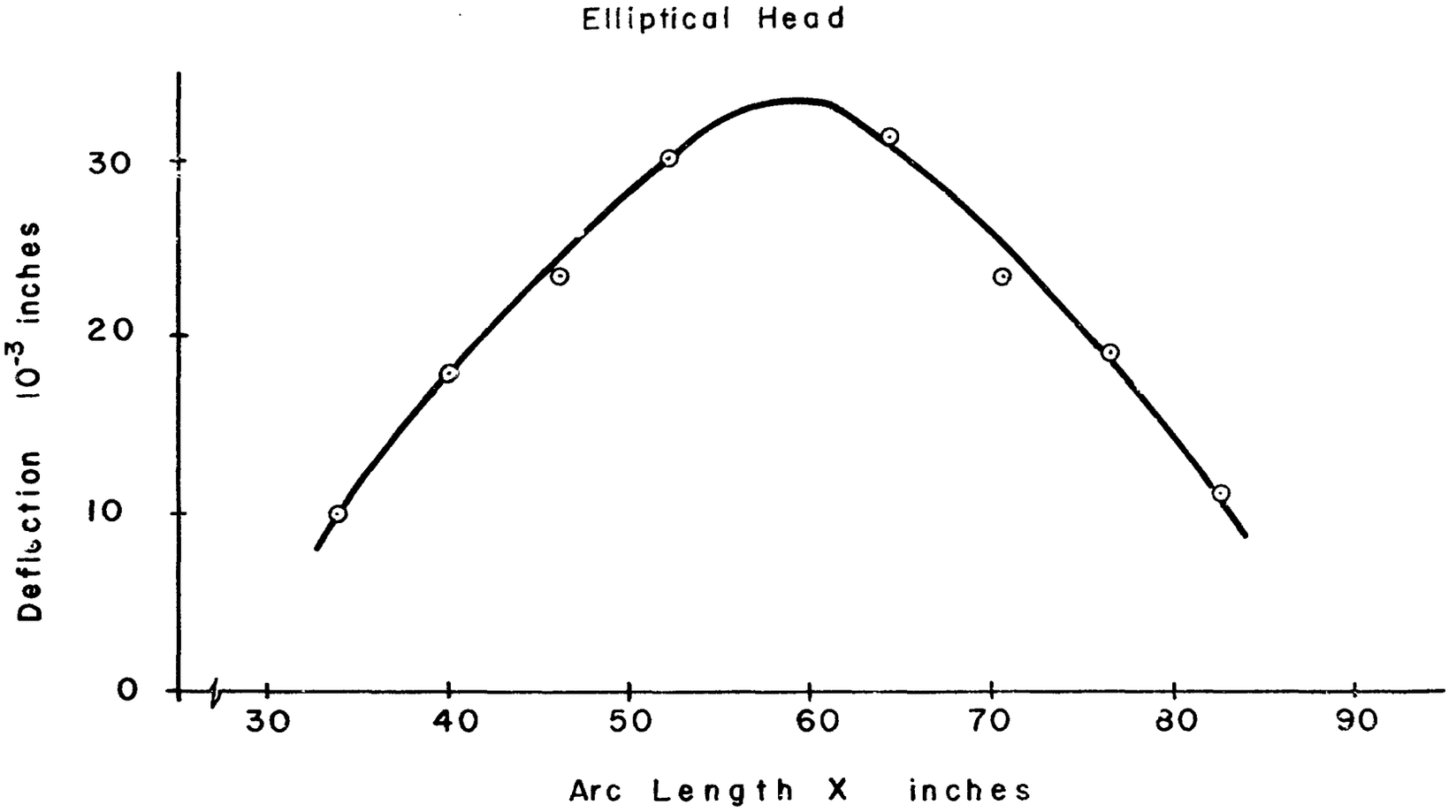

Figure 57. Deflection By LVDT Measurements